Novel Image Processing Methods for Aiding Diabetic Retinopathy Diagnosis Based on Color Fundus Images

Doktori (PhD) értekezés

Lázár István

Témavezető: Dr. Hajdu András

Debreceni Egyetem
Természettudományi Doktori Tanács
Informatikai Tudományok Doktori Iskola
Debrecen, 2016.

Ezen értekezést a Debreceni Egyetem Természettudományi Doktori Tanács Informatikai Tudományok Doktori Iskola Diszkrét matematika, képfeldolgozás és komputergeometria programja keretében készítettem a Debreceni Egyetem természettudományi doktori (PhD) fokozatának elnyerése céljából.

Debrecen, 2016.

….....
Lázár István

Tanúsítom, hogy Lázár István doktorjelölt 2009 – 2012 között a fent megnevezett Doktori Iskola Diszkrét matematika, képfeldolgozás és komputergeometria programjának keretében irányításommal végezte munkáját. Az értekezésben foglalt eredményekhez a jelölt önálló alkotó tevékenységével meghatározóan hozzájárult. Az értekezés elfogadását javaslom.

Debrecen, 2016.

….....
Dr. Hajdu András

Novel Image Processing Methods for Aiding Diabetic Retinopathy Diagnosis Based on Color Fundus Images

Értekezés a doktori (Ph.D.) fokozat megszerzése érdekében az informatikai tudományágban

Írta: Lázár István okleveles programtervező matematikus

Készült a Debreceni Egyetem Informatikai Tudományok Doktori Iskolája, Diszkrét matematika, képfeldolgozás és komputergeometria programja keretében.

Témavezető: Dr. Hajdu András

A doktori szigorlati bizottság:

elnök:	Dr. Kruppa András	……..
tagok:	Dr. Palágyi Kálmán	……..
	Dr. Fazekas Gábor	……..

A doktori szigorlat időpontja: 2013. október 25.

Az értekezés bírálói:

…….. ……..

…….. ……..

A bírálóbizottság:

elnök:	……..	……..
tagok:	……..	……..
	……..	……..
	……..	……..
	……..	……..

Az értekezés védésének időpontja:

CONTENTS

LIST OF FIGURES

LIST OF TABLES

1 INTRODUCTION

1.1 Motivation

Diabetic retinopathy (DR) is the most common microvascular complication of diabetes. It develops in most patients with long-standing illness and has become the major cause of vision loss in developed countries. It affects up to 80% of patients who have had diabetes for 20 years or more, though there is evidence that it begins to develop 7 years before the diagnosis of type 2 diabetes [1]. DR is a silent disease in early stages and many of the cases are only diagnosed when serious vision loss occurs. Effective treatments, such as blood pressure control, scatter laser treatment, or in severe cases, vitrectomy can prevent vision loss. However, early diagnosis is a key factor. Diabetic patients are advised to get a comprehensive dilated eye exam at least once a year, so that DR may be diagnosed at the earliest possible stage.

The diagnosis of DR is based on the identification of visible lesions and vascular abnormalities on the *fundus* (the interior surface of the eye). Nowadays, the most widespread diagnostic tool is color fundus photography. For this aim, the eyes are usually dilated by applying special eyedrops which causes the pupils to widen. Digital images are then taken of both eyes with different settings using special fundus cameras [2]. Though there are other imaging techniques, such as optical coherence tomography (OCT), and other diagnostic options, such as fluorescein angiography (FA), color fundus imaging still retains its leading role in DR diagnosis. This is mostly because of its speed, cost-effectiveness, and non-invasive nature. However, the identification of early symptoms on color fundus images can be very challenging. Computer aided diagnostic (CAD) systems that provide support in the recognition of lesions and deformations related to DR could be a major asset for clinicians in this otherwise time and human resource demanding procedure [3]. DR screening programs are already available in certain countries, such as the UK, the Netherlands, and the US, mostly funded by the national healthcare systems. The procedure in these cases is usually that color photographs are taken of the patients' eyes in a timely manner and evaluated in dedicated reading centers,

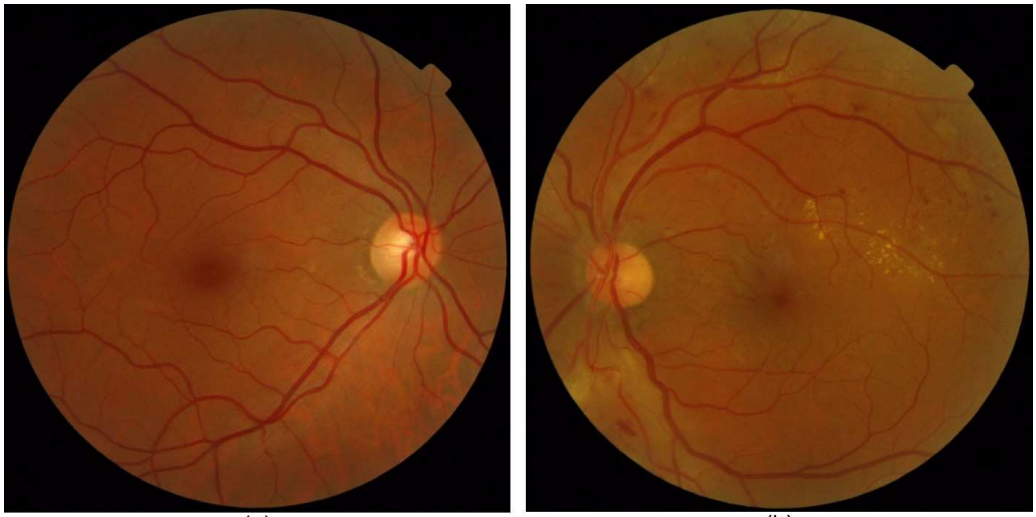

Figure 1. Examples for a healthy fundus image (a) and another one showing signs of DR (b). Both images are from the MESSIDOR database (http://messidor.crihan.fr).

where trained graders assess the presence and stage of eye related complications.

In Fig. 1, an image of a healthy fundus and another one showing symptoms of DR are presented. (Images are from the MESSIDOR database, see http://messidor.crihan.fr).

This thesis focuses on the proposal of novel image processing techniques for the automatic screening of DR based on non-invasive retinal imaging. We concentrate on two closely related tasks: the detection of microaneurysms (MAs), and the segmentation of the vascular system. While these two aims might seem unrelated, the approaches in the literature show several similarities. The methods proposed in this dissertation are also similar in the sense that they are based on the same novel approach regarding the general methodology of directional processing.

1.2 Basic anatomy of the fundus and lesions associated with diabetic retinopathy

From a simplified point of view, the fundus consists of the retina, the optic disc, the macula, the fovea, and the blood vessels. Though the structure of the eye is more complex, it is sufficient to discuss only these anatomical parts to

understand the content of this dissertation. It is common in the literature to refer to fundus images as retinal images, and both expression will appear in this work as well.

The optic disc is the location where the optic nerve and the major blood vessels enter the eye. There are no light receptors in this area, which causes the blind spot in human vision. The macula is a highly pigmented spot close to the center of the retina. Its center is called the fovea and it is responsible for sharp vision. The fundus is the only part of the human body where the circulation in small blood vessels can be observed directly. The geometrical and morphological properties of retinal blood vessels, such as width, length, tortuosity, or branching patterns can provide valuable information about several ophthalmologic and cardiovascular diseases [4]. In the case of DR, new blood vessels may grow and bleed into the eye, thus blocking vision. The structure of the blood vessels in the retina is unique to every person, thus, these images are also widely used for biometric identification and authentication purposes. Manual segmentation, i.e., the annotation of every pixel in an image that belongs to a visible vessel, is a very time demanding task even for an expert with training. Automatic vessel segmentation and quantification are essential tasks in a retinal imaging CAD system. Besides of being a component of primary diagnosis, results of vessel segmentation are used for the localization of the optic disc and the fovea, and also as an aid to lesion recognition methods.

The most important lesions associated with DR are microaneurysms (MAs), haemorrhages, and exudates. The presence of MAs on the retina is the earliest and most characteristic symptom of DR [5]. Their diagnostic significance is even more important due to the fact that in the case of non-proliferative diabetic retinopathy (NPDR) no other symptoms at all are noticeable, only the presence of MAs can indicate the, at this stage still manageable, DR. MAs appear on the surface of the retina as small circular dark spots. In the more conventional sense, MAs are dilations of the capillary walls filled with blood. The lesions that are referred to as MAs in the case of retinal images are actually small bleedings that have a circular shape due to the physical nature of the surface of the retina. If the bleeding continues, the lesion gets larger and more amorphous, which is the reason why it is referred to as a haemorrhage from this point on.

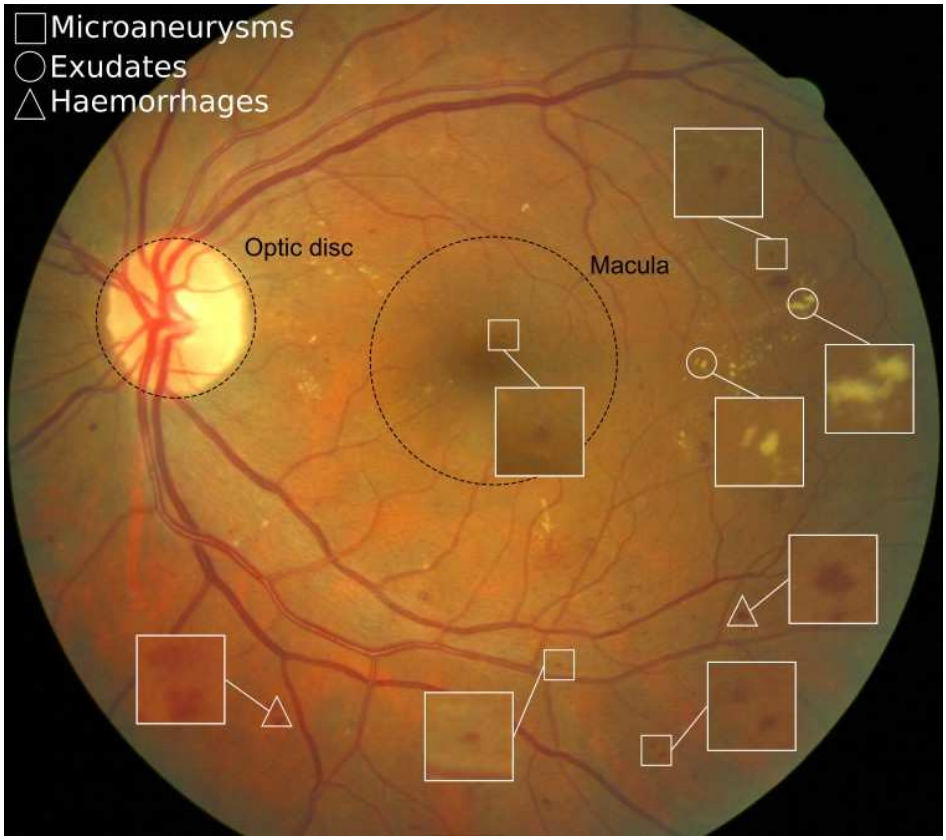

Figure 2. A fundus image showing MAs, exudates, and haemorrhages. The optic disc and the macula are also marked.

MAs usually appear close to thin vessels, though it is important that they cannot be located on the visible vessel itself. This characteristic has to be taken into consideration when developing automatic MA detection methods. MAs have a clinically established maximal diameter, which is usually considered to be less than 125 µm. The recognition of MAs is essential in the process of DR grading, since it forms the basis of deciding whether an image of a patient's eye should be considered healthy or ill. Thus, automatic MA detection is one of the core functionalities of a DR screening CAD system.

Exudates are lipid deposits that leak from damaged blood vessels and have an appearance of various shapes and well defined edges with mostly yellowish or white color [6], [7]. There are other types of bright lesions, such as cotton-wool spots, however, since here we do not specifically concentrate on bright

lesions, these are collectively referred to as exudates, or simply just as bright lesions. The reason that these lesions have to be discussed anyway is that their presence is a significant hindering factor for developing precise vessel segmentation methods, which topic will be discussed in more details in later sections.

In Fig. 2, a fundus image showing MAs, haemorrhages, and exudates is shown, with the macula and the optic disc being marked as well.

1.3 Contributions and main structure of the dissertation

The main contributions of this dissertation and the corresponding publications are the proposal of two novel automatic retinal microaneurysm detectors and an automatic retinal vessel segmentation method. These techniques share a common basic principle, the usage of directional pixel-wise processing to describe the local surroundings of a pixel under examination. The extracted information is used in further steps such as classification or region growing. While most similar directional approaches in the literature use only the summed or maximal response over the considered directions, the techniques described here offer different solutions by treating the directional responses of a pixel as a vector. New methods are presented for cross-sectional profile response calculation and direct analysis. Additionally, the proposed vessel segmentation technique's capability in another field of medical image processing, namely, the segmentation of pigment network in dermatoscopic images is also presented. All the proposed methods have been thoroughly tested on publicly available image sets and compared with many of the state-of-the-art algorithms.

The main contributions of the dissertation together with the corresponding publications can be summarized as follows:

1. The proposal of an unsupervised MA segmentation method based on pixel-wise directional responses obtained by a fundamental morphological technique [8].
2. The demonstration that the candidate extraction phase of MA detection can be based on the extraction of regional minima of the image

intensities [9].

3. The proposal of an MA detection method based on the direct analysis of image minimum cross-section intensity profiles. The presentation of a peak detection and property measurement technique, the proposal of candidate features that are derived from the statistical measures of the directional peak properties, and a final MA scoring formula [9]–[12].
4. The proposal of a novel vessel segmentation approach based on a directional response vector similarity measurement and its application in pixel level classification and region growing segmentation [13], [14].
5. The proposal of a matched filtering technique that does not give high response to the steep intensity transitions at the boundaries of the optic disc and bright lesions [14].

The rest of the dissertation is organized as follows. In the following section, deeper overviews on the background and the state-of-the-art literature methods for retinal MA detection, vessel segmentation, and accuracy measurement techniques are given. In sections 3 and 4, the author's proposals for MA detection and vessel segmentation are presented, respectively. The results of performance evaluation conducted on publicly available image sets and an online challenge are also discussed. The application of certain components of the proposed vessel segmentation technique to dermatoscopic pigment network segmentation is also discussed in section 4. The main points and contributions are summarized in English in section 5, and in Hungarian in section 6.

2 OVERVIEW OF THE RELATED LITERATURE TECHNIQUES

This section gives an overview on the literature methods that have been proposed for retinal MA detection (section 2.1) and vessel segmentation (section 2.2) tasks. We mostly discuss those methods that have been evaluated on publicly available data by following protocols that make objective comparison possible. In section 2.3, we discuss the accuracy measurement techniques used in the field.

2.1 Retinal microaneurysm detection methods

The expectation towards automatic MA detection is to reliably mark the centroid of MAs in the image, preferably along with confidence values that express the certainty of the individual candidates of being MAs. In a CAD system, the operator may vary a confidence threshold to observe possible lesions at different confidence levels. Besides the localization of MA centroids, automatic methods can also outline the boundaries of the corresponding lesions, which can further help the diagnosis. This latter approach is sometimes referred to as MA segmentation, however, both the expressions detection and segmentation occur in the literature.

It may seem straightforward to develop methods for the automatic localization of MAs on retinal images due to the fact that they have a well-defined shape and size. Unfortunately, there are certain circumstances that make this detection task rather complicated. The problem itself is not the localization of MAs, but the elimination of false detections. Since the presence of even one MA is a symptom of incipient DR, the decision between whether the image should be considered healthy or ill is mostly based solely on the results of the MA detection methods in such a system. Moreover, the current trends develop towards of composing such CAD systems that can precisely filter out healthy images, so that they would not be passed for inspection to an ophthalmologist. Fundus images of later stages of DR show more pathologies, e.g., larger haemorrhages or exudates. Consequently, other tools should be considered to recognize these lesions. Techniques exist that instead of trying to detect one

Figure 3. Parts of the vessels and artifacts on the optic disc that locally appear as MAs.

specific lesion aim to categorize regions of the image as being pathological or not [15], [16]. Other techniques aim to obtain such features of the entire image that can be used to recognize pathological cases [17].

Amongst the many factors hindering MA detection are the pigmentation of the retina, disconnected vessel segments that appear as small dark objects of various shapes, and the crossings of thin blood vessels. As it can be seen in Fig. 3, many small dark structures having local MA like appereance can be observed within the region of the optic disc. However, due to the high contrast of this region, such anomalies may be wrongly recognized as MAs by many methods. The general approach to overcome this problem is to segment the optic disc and eliminate detections within this region. We note that while the tasks of MA detection and optic disc segmentation might seem unrelated, there is a strong connection between MA detection and vessel segmentation methods, and optic disc detection relies highly on the result of automatic vessel segmentation methods.

Most techniques in the literature break down the detection of MAs into the steps of image preprocessing, candidate extraction, feature extraction, and candidate classification, as shown in Fig. 4. The first step usually involves an image transformation aimed at improving image quality, such as different methods for contrast enhancement, smoothing, and illumination correction. Retinal images have the largest contrast in the green channel, consequently, the common practice is to use the green channel for processing. For noise reduction, convolution with Gaussian masks and median filtering are widely applied techniques.

In the candidate extraction phase, methods use different techniques to

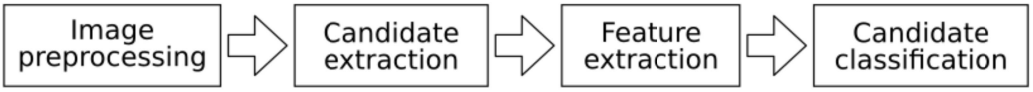

Figure 4. The general workflow of MA detection methods in the literature.

localize pixels or regions that possibly belong to MAs, even at the cost of marking a high number of non-MA regions. Next, specific descriptors that may be either pixel- or region-based ones are obtained for each candidate. These features are intended to capture those characteristics that help to distinguish true candidates from false ones. In the classification step, mostly supervised machine learning algorithms are used to categorize candidates based on their feature vectors as true or false MAs.

So far, more than 50 features have been proposed for binary classifiers in MA detectors. Some features are rather simple and extensively used, while some others are mostly related to a specific candidate extraction method. Examples for the more general ones are the discrete geometry and color-based features. Discrete geometry based ones include the connected component size, compactness, circularity, perimeter, area, aspect ratio, and eccentricity. Some of the common color features are the mean and standard deviation of the intensities within the region in different color channels, hue, dynamic, shade corrected intensity, or the intensity differences of the region and its surroundings.

Methods that follow other workflows exist as well. Some of these apply classification at pixel level for initial segmentation, or consider an entirely non-supervised approach, such as one of the author’s proposals described in this work. Comprehensive surveys of available techniques in the literature are given by Mookiah et al. [18], Winder et al. [19], and Patton et al. [20].

The first computerized approaches for the segmentation of retinal MAs were described by Laÿ [21] and Baudoin et al. [22]. These methods calculate the maximum of morphological openings with linear structuring elements of different orientations. This step results in an image from which the structures that are smaller than the structuring element are missing. It is easy to see that the maximum of morphological openings mostly enhances elongated structures such as the vessels. Therefore, the difference of this image and the original one

(top-hat transformation) may be thresholded to obtain MA candidates. Thus, the segmentation is based on the assumption that all darker structures that are not part of the vessel system presumably correspond to lesions. These approaches have constituted the basis for several later algorithms. It is important to note that Zana et al. [23] applied the same morphological approach for retinal vessel segmentation.

Spencer et al. [24] applied preceding illumination and shade correction steps to improve the quality of fluorescein angiography images before the actual segmentation and detection steps. A Gaussian matched filter was used after the top-hat transformation to enhance MA-like objects, and a recursive region growing method produced the segmented MA candidates. This was the first method that involved an additional classification step. Variations of this method with different preprocessing steps and classification methods have been proposed by several authors, e.g., in [25] Cree et al. applied a redesigned region growing and classification algorithm, Frame et al. [26] concentrated on comparing classification techniques, while Mendonca et al. [27] and Hipwell et al. [28] proposed other variants. Fleming et al. in [29] also built on the work of Spencer et al. [24] for candidate region extraction, and applied a consequent Levenberg–Marquardt nonlinear least-squares fitting of a paraboloid. The resulting paraboloid parameters were then also used as features for classification.

A limitation of the morphological approach by Laÿ [21] is that the usage of oversized structuring elements results in the detection of tight vessel curvings as possible MAs. However, if the length of the linear structuring element is chosen such that no parts of the vessels will be wrongly detected, true MAs would be lost, since no circular structure that is larger than the structuring element can be detected in this way. In [30], Niemeijer et al. considered an additional pixel-wise classification based candidate extraction method and merged the two outputs. Other morphology based methods include the one proposed by Walter et al. [31], where criteria based morphology operators [32] are applied in the candidate extraction phase followed by the candidate classification. Ram et al. [33] proposed a method, in which the candidate selection is the same as described in [30], and a two-stage candidate rejection

step is applied as well. The confidence values of the remaining candidates are calculated as their distance from the optimal hyperplane of a support vector machine. The method proposed by Sopharak et al. [34] also uses grayscale morphology for coarse MA segmentation, similarly to the approach presented in [31]. The authors of [34] also consider additional feature extraction and classification using a Naïve Bayes classifier.

Non-morphology based methods have also been investigated. Zhang et al. [35] used Gaussian masks of different sizes and standard deviations, and calculated the maximal pixel-wise correlation with the original image. The result produced the basis of the candidate extraction phase, and the correlation results were also used in the candidate classification step. Matched filtering with a Laplacian of Gaussian (LoG) mask in addition with a circular symmetry operator were used by Bhalerao et al [36]. Mizutani et al. [37] utilized a double-ring filter for the initial detection of MAs. Quellec et al. proposed an approach using template matching in the wavelet domain [38]. In the method proposed by Sanchez et al. [39] the histogram of the preprocessed image is modeled using a 3-component mixture model, with the assumption of normal distribution in the gray level of each class. The MA candidates are extracted by thresholding the obtained model and classified by a logistic regression classifier. Radon transformation has been applied to MA detection by Giancardo et al. [40], [41], Tavakoli et al. [42], and Oliveira et al. [43]. Inoue et al. [44] utilized the eigenvalues of the Hessian matrix at a given candidate point to determine a shape index. Similarly, in [45] Adal et al. used the determinant of the Hessian as the basis of candidate extraction. The mean and maximum of the eigenvalues together with the determinant of the Hessian were used as features for classification. The usage of the Hessian is also a widely used approach in vessel segmentation, which subject will be discussed in the next section.

Akram et al. [46] proposed an MA segmentation approach whose initial candidate extraction phase is based on the pixel-wise maximal directional Gabor filter response, which is also a common technique in retinal vessel segmentation. The main contribution of their proposal is the usage of a hybrid classifier, which is a weighted combination of an extension of a multimodel mediod based modeling approach, a Gaussian mixture model (GMM), and a

support vector machine (SVM). Ensemble based approaches have been proposed by Antal and Hajdu [47], [48]. These are based on the optimal combination of preprocessing methods and candidate extractors. The unsupervised morphology based method [8] described in this dissertation is also used as a candidate extractor member in [48].

2.2 Retinal vessel segmentation methods

The purpose of automatic retinal vessel segmentation is to construct a binary mask for the input fundus image where pixels belonging to the vessel network are marked as foreground ones. See Fig. 5. for a demonstration.

Changes in vessel width and tortuosity over time are important diagnostic elements of many retinopathies, such as those due to hypertension, diabetes, or prematurity. In the case of hypertensive retinopathy, no lesions are present on the retina, thus, the diagnosis is solely based on the evaluation of features of the retinal vascular system. Similarly, plus disease is associated with retinopathy of prematurity and characterized by the increase in vessel width and tortuosity. Distortion and growth of new vessels is also a symptom of DR in later stages, hence, automatic vessel segmentation is also an essential component of automatic DR screening systems. Methods for the automatic characterization

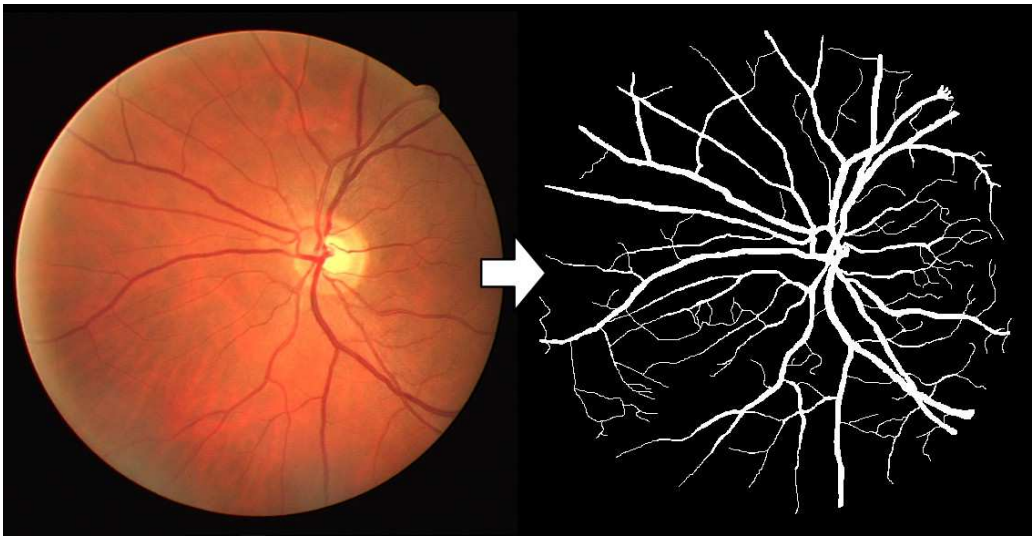

Figure 5. The desired output of automatic vessel segmentation.

and grading of retinal vessel tortuosity have been proposed by Heneghan et al. [49] and Grisan et al. [50]. However, these methods assume the availability of a precise binary vessel mask.

The region of the optic disc may be considered as the root of the retinal vascular system. Thus, it is straightforward to at least partially build the task of optic disc localization upon the result of one or more vessel segmentation methods. The localization of the optic disc may also be necessary in the diagnosis of certain eye conditions, such as glaucoma, which directly affects the appearance of the optic disc. Precisely localized optic disc is also useful as an aid for lesion detection methods, such as the previously described MA detectors, or for bright lesion segmentation due to the similar color information. Since there is an anatomical/mathematical relationship between the location of the optic disc and the macula, accurate vessel segmentation may also be the basis of the localization of the macula and the fovea. Some of the methods in the literature for optic disc and/or macula/fovea detection using vascular information include those of by Foracchia et al. [51], Youssif et al. [52], Niemeijer et al. [53], Mendonca et al. [54], and Hoover et al. [55].

A precise vessel mask can provide great assistance to lesion detection methods as well. There are several similarities between vessel segmentation and MA detection methods in the literature, e.g., the first and most fundamental morphological approach is basically the same in both cases. There are also methods for haemorrhage segmentation that rely on vessel masks, e.g., the one proposed by Tang et al. [56]. In [57], Youssef and Solouma discuss how precise vessel segmentation can be used to improve exudate detection accuracy.

Multimodality is an important factor in fundus image processing to improve the recognition rate of certain lesions. Such an approach is the registration of red-free and angiographic images, which is mostly done using key-points of the vascular tree. Temporal registration, i.e., the registration of images of the same modality taken at different times is essential for the follow up of the evolution of lesions and changes in the vascular system. Such techniques have been proposed by, e.g., Zana and Klein [58], and by Matsopoulos et al. [59]. Since the pattern of the vascular system is unique for each individual, fundus images provide a solid basis for biometric identification and authentication

applications. Accordingly, the literature on the subject is fairly excessive. Some of the available techniques are the ones proposed by Mariño et al. [60], Köse et al. [61], or Lajevardi et al. [62].

Vessel segmentation is a complex problem even for healthy images, and it gets more complicated as the images start to show pathological signs. One such interfering factor is the presence of closely located patches of bright lesions. The otherwise normal elongated background region between these lesions can locally be very similar to – or even indistinguishable from – vessel segments. On the other hand, it is frequent that bright lesions are actually surrounding vessels, which precludes the usage of an approach which automatically excludes darker regions enclosed between bright patches. It is also important to mention the region of the optic disc, where vessels are also located in a similar bright region.

Existing methods in the literature have been categorized according to several aspects, such as region-based, edge-based, tracing/tracking-based, morphological, matched filter based, multiscale, supervised, unsupervised, or model-based ones [4], [63]–[67]. However, it might not be the most practical to describe a method based solely on a single property of its operation, since most of them combine several techniques. For example, a supervised learning based method may apply multiple lower level pixel- or region-wise descriptors, while these features can be used in a tracking or region growing scheme as well.

Vessels in retinal photographs can be described as Gaussian-like structures perpendicular to their local orientation in the intensity plane. The usage of matched filters and morphological operators in a rotational/directional manner for their segmentation are some of the very fundamental techniques in the literature [23], [68], [69]. Methods that apply this approach, at some point of their operation usually proceed by rotating a filter or structuring element around its center with a specific angle to cover all orientations. Then, they match every pixel of the input within its ROI with all masks, considering the maximal response as the vessel strength at the given position. In the case of matched filters, the filters can be one or two dimensional, and the matching is usually performed by convolution. Several types of filters exist, such as zero mean Gaussians [68]–[71], Gaussian mask with one side of the filter being negative

and the other one positive [72], Gabor filter [63], simple Gaussian [73], first-order derivative of Gaussian [74]–[76], and filters obtained from perpendicular profiles of sample vessels [77]. In the case of morphological approaches, sum of top-hats of rotated linear structuring elements is one of the most fundamental techniques [23]. There are similar directional methods, such as the tramline filter proposed by Lowell et al. [78] and Al Diri et al. [79], the approach of Ricci and Perfetti [80], where the average intensity along rotated linear segments are considered as line strength measures, the method of You et al. [81], which employs rotated radial projections similar to Radon transform, or the line integral based vessel measure by Yuan Yuan et al. [82]. The method proposed by Nguyen et al. [83] is also based on the line measure in [80] with an additional normalization step and the usage of the raw green channel intensity information as a feature. In [84], Wang et al. employed convolution with a multiwavelet kernel filter for all possible directions at each pixel and considered the maximal responses. Similarly, Qian et al. [85] used the maximal response of rotated Gabor wavelet transforms. Not all methods in the literature are fully automatic, e.g, the tracking based techniques proposed by Yin et al. [86], [87] require the manual selection of two initial opposite diametric vessel edge points to segment the corresponding segment.

A possible way of handling the varying width of vessels is the multiscale analysis. In some matched filter methods, it is accomplished by considering different scale parameters for the filter [63], [73], [75]. The method proposed by Odstrcilik et al. [88] employs a matched filtering approach with predefined filters for the different vessel widths. Lupascu et al. [66] and Fraz et al. [63] also consider the maximal value of directional Gabor filters for multiple scales over all possible directions as a feature for every pixel. The methods of Martinez-Perez et al. [89] and Palomera-Perez et al. [90] apply smoothing with Gaussians of different scales and extract the gradient magnitude and principal curvature of the Hessian tensor. A diameter-dependent equalization factor is introduced to normalize both features along the scales, and local maxima are kept as final features in the classification process. The usage of Hessian eigenvalue analysis is a popular approach in the field. Anzalone et al. in [91] applied a similar technique with keeping the maximal absolute eigenvalue as

the final response. The method of Annunziata et al. [92] also utilizes a multiscale Hessian approach for vessel enhancement with also proposing a novel exudate inpainting technique to improve the detection performance of pathological images. The methods of Yin et al. [93] and Yu et al. [94] are also examples for multiscale Hessian analysis for vessel curvature estimation. The ridge measure proposed by Staal et al. [95] is based on the sign of the largest absolute eigenvalue of the Hessian, and in [66], Lupascu et al. considered the same approach using multiple scales with considering the frequency of the negatives as a local descriptor. The filter construction from manually selected blood vessel samples as proposed by Jan et al. [77] handles the different vessel widths by constructing multiple filters, each for a different vessel width. The method proposed by Vlachos and Dermatas [96] applies a line-tracking method based on calculating a cross-sectional profile parameter for the candidate pixels from the intensity values of two opposite pixels with a given distance from the candidate and the intensity of the candidate pixel itself. The multiscale nature of the method comes from considering multiple distance values, i.e., multiple widths for the cross-sectional profile parameter. The combination of different scales is calculated as the weighted average of the cross-sectional profile parameters at different scales by assigning higher weight to larger width arguments. Miri and Mahloojifar [97] employed discrete curvelet transform as part of the image enhancement, followed by a morphological segmentation step. This transform makes it possible to obtain multiscale and directional representation of the underlying structures, while differing from other directional wavelet transforms in that the directional resolution is scale dependent.

The most challenging issues concerning retinal vessel segmentation are the presence of pathologies in the image, such as haemorrhages and bright lesions. Moreover, nonvascular structures in healthy images, such as the boundary of the optic disc, cause strong responses in many existing methods. Those approaches that address these issues may consider additional steps to exclude false detections. For example, in [77], an external optic disc detector is used to erase structures in this region, while in [98], Lam and Hong Yan considered the application of a pruning operator based on centerline extraction. Classification

as a post-segmentation step is also considered in many of the previously described methods. However, classification used in a pixel-wise manner to construct vessel probability or likelihood maps for segmentation can only be successful in distinguishing false positives if the problem itself is considered in the design of low level processing. For example, in [80], the authors claim that the gray level intensities in combination with a modification of the line strength measure can eliminate the effects of the unmodified line strength measure at the edge of the optic disc. Lam et al. [67] proposed the “Smooth Imaging” and “Structurally Differentiable” planes to deal with the so called “ringing effect” [67], [76] caused by bright lesions. To achieve a similar effect, zero-mean Gaussian matched filter and its first order derivative are used by Zhang et al. [74]. Lei Zhang et al. [73] considered a double sided thresholding on the Gaussian matched filter response to eliminate such non-vessel edges.

Methods based on various wavelet transforms for vessel segmentation have been proposed as well. In [99], Fathi and Naghsh-Nilchi claimed that by considering the magnitude of the imaginary part of the complex Gabor transform wavelet coefficients it was possible to separate vessel structures and non-vessel step edges. The same approach is used by Usman Akram et al. in [100], except that the authors did not consider the imaginary coefficients separately. The segmentation method of [100] is a recursive thresholding based one, while the subsequent classification step to identify vascular segments showing signs of neovascularization is close to the technique proposed by the same authors for MA detection in [46]. The method proposed by Bankhead et al. in [101] is based on Isotropic Undecimated Wavelet Transform [102], which is implemented by calculating scaling coefficients through lowpass filtering and wavelet coefficients by subtraction at each iteration. Segmentation is performed by summing wavelet coefficients corresponding to the iteration exhibiting the best contrast and a subsequent thresholding based on the percentage of the smallest valued coefficients. Subsequent centerline extraction and refinements are applied and the intensity profiles perpendicular to the vessels are used to identify exact vessel widths. The method proposed by Soares et al. [103] considers continuous wavelet transform with Gabor wavelet for analysis, which is actually a complex modulated Gaussian. For each pixel and scale, the wavelet

response with the maximal modulus over all possible directions is considered. The segmentation is a pixel-wise classification using the wavelet coefficients and the green channel intensities together as the feature vector for each pixel. Note that such application of wavelet transformation is highly similar to the previously discussed rotational multiscale matched-filtering techniques.

2.3 Performance evaluation methodologies

The basis of the performance evaluation of both MA detectors and vessel segmentation methods is the comparison of their outcome to the manual expert annotations of the same images. These expert annotations are usually referred to as ground truth data, and are usually released with the publicly available image sets. In the case of MAs, the ground truth mostly consists of the coordinates of the MA centroids in the given images, while the manual vessel segmentations are provided in terms of binary masks.

The evaluation of a vessel segmentation result is performed pixel by pixel, thus, it is very straightforward. Those pixels that have been correctly identified as vessels are called true positive (*TP*) detections. Similarly, those that are correctly marked as background are labeled as true negative (*TN*) ones. Two other categories are the false positive (*FP*) and false negatives (*FN*) detections, describing that either the given point is incorrectly marked as a vessel, or incorrectly marked as a background one, respectively.

In the case of MA detectors, the procedure is slightly more complicated. In this case, pixel by pixel comparison cannot be applied. The reason of this fact is that an MA can always be represented as a single pixel by its centroid. A detection is usually considered to be a *TP* if it is significantly close to a ground truth MA point, otherwise it is labeled as an *FP*. It is important that a single ground truth MA point can only be matched to at most one detected lesion. Evidently, always the closest match should be considered. Those points of the ground truth data that have not been matched to any detected MA are considered to be false negatives (*FN*).

The ratio of all true positive detections and all positives in the ground truth data is called sensitivity or true positive rate (*TPR*). That is,

$$TPR = \frac{\#TP}{\#TP + \#FN}, \tag{2.1}$$

where "#" denotes the total number of the respective detections in an image or over several images. Sensitivity expresses how effective the method was in identifying MAs or vessel points. However, it does not give any information about the relationship of correctly identified negatives and false positives. For the evaluation of vessel segmentations, the specificity or true negative rate (*TNR*) can be used for this purpose. Specificity is calculated as the ratio of true negatives and all negatives, i.e,

$$TNR = \frac{\#TN}{\#FP + \#TN}. \tag{2.2}$$

False positive rate (*FPR*) is often used analogously with specificity, since the relation between the two can be formulated as

$$FPR = 1 - TNR = \frac{\#FP}{\#FP + \#TN}. \tag{2.3}$$

An ideal system would have 100% sensitivity and 100% specificity (or 0% *FPR*).

The accuracy (*ACC*) of the system is also a widely used performance measure and is calculated as the ratio of all positive detections and the number of all detections, i.e.,

$$ACC = \frac{\#TP + \#TN}{\#TP + \#FN + \#FP + \#TN}. \tag{2.4}$$

While sensitivity, specificity and accuracy together describe well the performance of a method at a given discriminative threshold, it can also be very informative to visualize and measure the performance of the system at several threshold levels. For this aim, the receiver operating characteristic (*ROC*) analysis technique is primarily considered in the field. Originally, it was proposed for performance comparison in the case of binary classifiers, though later it has been adapted for image processing tasks as well. *ROC* analysis is especially a popular choice for the evaluation of various binary segmentation results.

An *ROC* curve plots *TPR* against *FPR* as the discrimination threshold of the

system varies. To compare the *ROC* curves of different systems, the calculation of the area under the curve (*AUC*) by numerical integration is the de facto standard technique. Since both *TPR* and *FPR* range from 0.0 to 1.0, the maximal value of *AUC* is also 1.0. Thus, the system whose *AUC* is closer to 1.0 may be considered to perform better. The *AUC* figure can be used to describe the performance of the system at all *FPRs*, however, it may also yield misleading results when dealing with medical images. In such applications, usually only lower *FPRs* have diagnostic significance. The problem stems from that methods whose sensitivity is low at high specificity can outperform others whose sensitivity is higher at low *FPRs* in terms of *AUC*. Fortunately, many publicly available retinal image sets provide two manual annotations of the vessels for each image by different ophthalmologists. This way, the second segmentation can be compared with the first one and this result can be considered as a benchmark for the performance evaluation by providing the *FPR* and *TPR* of another independent human observer.

In the case of MA detectors, every pixel except those that are actually MA centroids in the ground truth data should be considered as a true negative. However, this would yield a very misleading sensitivity / specificity based accuracy measurement. Even in the case of MA regions, it is not clear how points that belong to the MA should be treated. This yields that even at a very high false positive per image rate, specificity would be always very high due to the largely different number of MA and non-MA points of the image. Thus, the *AUC* values of such *ROC* curves are always close to 1.0 making it impossible to objectively compare the detectors. Though in some of the early papers authors have reported the results of their experiments in terms of *ROC* analysis in this subject, nowadays this performance evaluation methodology has become obsolete. Instead, the most widespread technique in the literature for the evaluation of abnormality detection methods for medical images is the usage of free-response receiver operating characteristic (*FROC*) [104] curves. A *FROC* curve plots true positive rate against the average number of false positives per image as the discrimination threshold of the system varies.

The usage of *FROC* curves is popular among researchers due to the fact that it is suitable to compare the performance of detection methods that provide an

unknown number of candidates, presumably corresponding to abnormalities on an image. However, since the average number of false positives per image is not bounded, i.e., there can be basically as many as the number of all image pixels, no widely accepted index number similar to the *AUC* that describes an entire *FROC* curve exists.

The Retinopathy Online Challenge [105] provides a platform for the objective evaluation of retinal microaneurysm detectors. Their evaluation protocol for measuring MA detection accuracy is based on summarizing the *FROC* curve figures into a single number, which is calculated as the average sensitivity at seven predefined average false positive per image rates (0.125, 0.25, 0.5, 1, 2, 4, 8).

3 NOVEL METHODS FOR THE DETECTION OF RETINAL MICROANEURYSMS

As it has been discussed in section 2.1, directional pixel-wise techniques are among the most popular ones in the field of automated retinal image analysis. Apart from the specific techniques, the main steps of operation of these methods are very similar. Though both the requirements and difficulties are different for MA detection and vessel segmentation, the solutions proposed here for the two tasks share several common points. One of them is that the directional responses of a pixel are utilized more extensively, and not just by considering a dedicated value which is usually the maximum or sum in most state-of-the-art methods.

In this section, two novel retinal MA detection methods are presented. The method described first is based on the directional grayscale morphological operation discussed in section 2.1. However, the proposed application of the directional top-hat values is novel and makes it possible to extract MAs without the need for any additional classification. The only parameter of the method is the MA diameter, which can be calculated from the ROI diameter. This approach proved to be competitive with the state-of-the-art techniques both individually and also as a candidate extractor member of an ensemble-based system. The secondly described method follows an approach of first extracting candidate points as local minima of the intensity image, and then analyzing their directional cross-section profiles to exclude non-MA candidates. This technique produced outstanding results and proved that directional cross-section profile analysis is a suitable approach to describe the surroundings of image structures. The technique is also unique in the sense that it simplifies the candidate extraction phase of MA detection to the extraction of image minimum regions. Though this step is part of many other image processing techniques applied in available literature methods, yet, such direct application has not been proposed before.

The input of the proposed MA detection methods, and also the vessel segmentation method described later in section 4.1, is a fundus image preferably along with its binary region of interest (ROI) mask. Since several

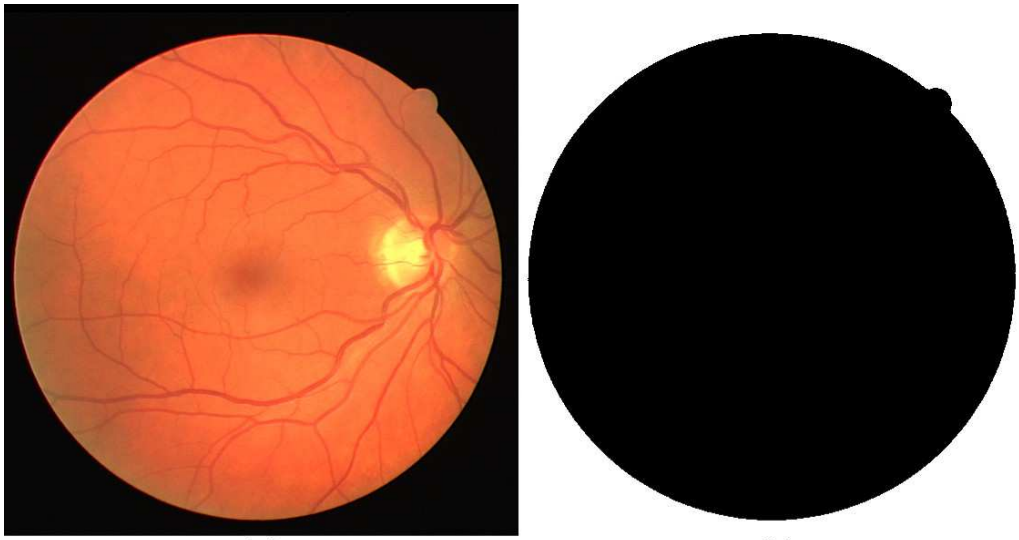

Figure 6. A fundus image (a) and its binary ROI mask (b).

methods exist for ROI detection, e.g., the one proposed by Gagnon et al. [106], this subject is not investigated in more details here. An example for the ROI mask of a fundus image is given in Fig 6. Though mostly color fundus images are used in the clinical practice, it is well established and also the general procedure to use the green channel of retinal images due to the fact that the contrast is the highest in this plane. Thus, the first step of all methods proposed in this work is to extract the green channel. We also require the input images to have such a spatial resolution that the diameter of the ROI is equal to 540 pixels, since this was the smallest ROI diameter in the publicly available fundus image sets. Naturally, it is possible to apply the presented methods to images of different sizes, though in this case other parameters have to be altered accordingly and the more image data will result in longer execution times.

Though the proposed methods do not require a specific kind of preprocessing, it was experimentally found that it is beneficial to consider a certain amount of image smoothing before the actual steps of detection. This is partially due to the fact that many fundus images are available in a lossy compressed format, which results in the distortion of small structures such as MAs. Since the proposed method particularly relies on the local intensity distribution of MAs, it is important to reduce the effect of noise. In the

implementation, convolution with a Gaussian mask with a variance of 1.0 was applied. The experiments showed that this level of smoothing suppressed noise sufficiently, while preserving true MAs. Other image enhancement techniques could also be considered. It is possible that images from other sources than those discussed here may require different kinds of preprocessing steps.

3.1 Directional cross-section profiles

Both the MA detectors and the vessel segmentation method proposed in this dissertation rely heavily on the concept of cross-section profiles. The cross-section of an image point is defined as the intensity values along a discrete line segment that is centered at the given point. Let P denote such a profile and $P[i]$ the intensity value at its i^{th} pixel, where the range of i is $[-r, r]$ with some $r \in \mathbb{N}$. Thus, the central value, i.e., the intensity of the pixel whose surroundings are being examined is $P[0]$. Hence, the length of the profile, i.e., the number of its pixels is $2r+1$. For every pixel, a set of such cross-sections are considered with equal rotational angle difference among the consequent cross-section lines. It can be easily seen that the number of cross-sections covering the surroundings of the pixel can be calculated as $180° / \Delta\varphi$, where $\Delta\varphi$ denotes the scan step. Also, let Φ denote a vector consisting of these cross-section orientations. The authors in [80] mention a 15° angular resolution for

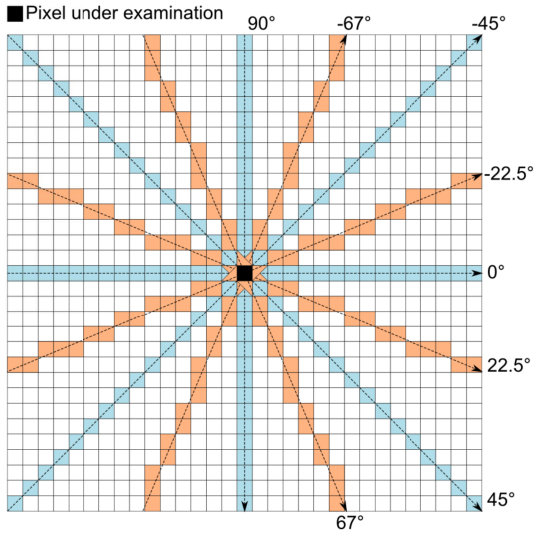

Figure 7. Model of the cross-section lines of a pixel.

the rotation of the line segments. A 6° difference between the consecutive cross-section lines was experimentally found to be sufficient. That is, 30 cross-sections for each pixel are considered in our approach. Fig. 7 shows the graphical representation of the cross-section lines for 8 orientations.

In order to visualize how these image cross-sections can provide valuable information about the underlying structures, Fig. 8 shows sample cross-sections of an MA, a vessel crossing, and an elongated non-MA structure. The orientations of the sample cross-sections were chosen so that the differences between the objects are clearly observable. It can be seen that an MA shows a

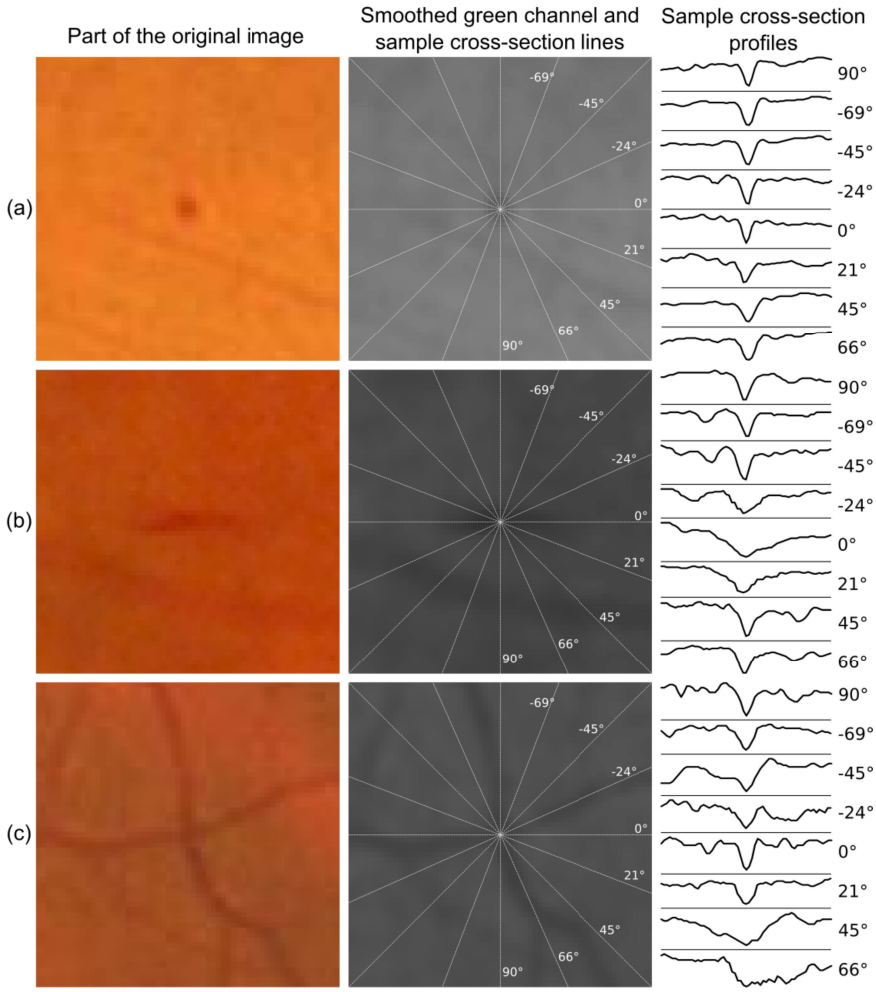

Figure 8. Sample cross-section profiles of an MA (a), an elongated non-MA object (b) and a vessel crossing (c), respectively.

definite inverted Gaussian like peak for all directions, contrary to the other non-circular structures.

3.2 An unsupervised MA detection method based on directional grayscale morphology and diameter opening

It has been discussed both in sections 2.1 and 2.2 that morphological opening with rotated flat structuring elements is one of the most fundamental techniques used for MA detection and vessel segmentation. All these methods follow the principle of using structuring elements that have just larger size than the maximal diameter of the MAs in the image. This step highlights only those structures, where the structuring element could entirely fit in. Considering the maximum of the opened values over the directions results in an image from which MAs are missing. The subtraction of this image from the original one gives a top-hat transformed version that contains the possible MA candidates. However, the drawback of this procedure is that longer structuring elements cannot fit into tighter vessel curvings. This yields that residues of the vessel network will be present in the top-hat image. In order to overcome this problem, most literature methods apply additional region growing, matched filtering, and/or classification steps to exclude false candidates [24], [29], [30].

The first MA detection approach MADET1 presented in this dissertation considers another complementary morphological technique, namely diameter opening [32], [107]. This technique has been used before for MA candidate extraction by Walter et al. [31] in a way of applying it directly on the preprocessed grayscale fundus image. However, in the application proposed here it is applied to data derived from the directional bottom-hat responses instead. This approach makes it possible to segment MAs without considering any subsequent classification or additional parameters. These properties become very useful when utilizing the method in an ensemble-based system, thus, it can be applied on images obtained by different preprocessing methods without any modification or fine tuning. A schematic workflow diagram of the operation of MADET1 is show in Fig. 9.

Next, the concepts of directional response vectors and the determination of the bottom-hat response are explained, after which the steps of the proposed

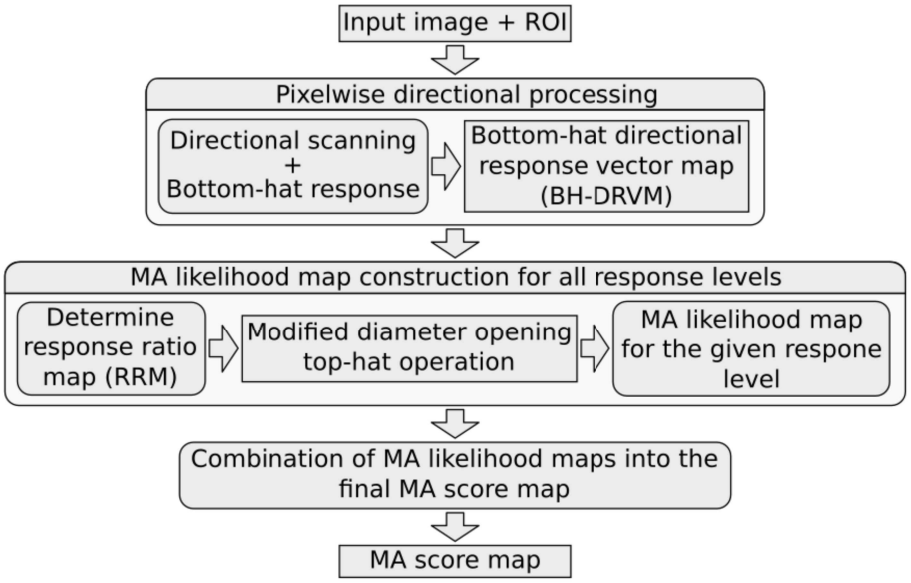

Figure 9. The workflow of the MA detection method MADET1.

unsupervised MA detection method are given.

3.2.1 Determination of the bottom-hat directional response

In order to numerically express the difference between the cross-sections of MAs and other structures, we define the concepts of directional responses and directional response vectors (*DRV*s). The response of a cross-section profile is a single real value. The *DRV* of a pixel is the set of its directional responses over a predefined number of orientations. The directional response vector map (*DRVM*) may be considered as a function that assigns a *DRV* to a pixel within the ROI. These notions will also be extensively used in section 4 during the presentation of a novel vessel segmentation method.

The grayscale erosion and dilation operations considered here can be defined as the selection of the minimal and maximal values in a cross-section profile, respectively. To obtain an opened image for a given orientation, the entire image needs to be eroded, then dilated. The closing operation is defined in the opposite way, i.e, dilation followed by erosion. To simplify the description of the method, here we define these operations on the same profile. Due to the constant structuring function in this case, the grayscale dilation and erosion operations may be simplified to the selection of maximum and minimum profile

values in a sliding window. The length of the profile has to be at least twice the length of the window to make sure that the result at the central element is valid.

Formally, for a profile *P*, using the previous index ranges and notations, dilation and erosion are defined as

$$\delta_\omega(P)[x] = max_{max(-r,\,x-\omega)\leqslant y\leqslant min(r,\,x+\omega)} P[y]\text{, and} \tag{3.1}$$

$$\epsilon_\omega(P)[x] = min_{max(-r,\,x-\omega)\leqslant y\leqslant min(r,\,x+\omega)} P[y]\text{, respectively.} \tag{3.2}$$

Here, ω is the integer half of the length of the sliding window, which in this case corresponds to the half of the maximal MA diameter. Since MAs are darker than the background on color images, we consider the bottom-hat (black top-hat) operation, which is defined as the difference of the closed and original data, formally

$$BH_\omega(P) = \epsilon_\omega(\delta_\omega(P)) - P\,. \tag{3.3}$$

Fig. 10 gives a graphical interpretation of the closed and the bottom-hat profiles of a sample cross-section profile. We note that the top-hat and bottom-hat operations can be freely exchanged based on whether the source image is inverted or not. For a given point and orientation only the result at the central point is relevant, which in this thesis is referred to as the bottom-hat response of the profile:

$$BHR_\omega(P) = BH_\omega(P)[0]\,. \tag{3.4}$$

Thus, the bottom-hat response vector of point (*x*,*y*) is defined as

$$BH\text{-}DRV_{x,y}[i] = BHR_{MA\_diam/2}\left(P_{x,y,\Phi[i]}\right). \tag{3.5}$$

where $P_{x,y,\alpha}$ denotes the cross-section profile with direction α centered at the

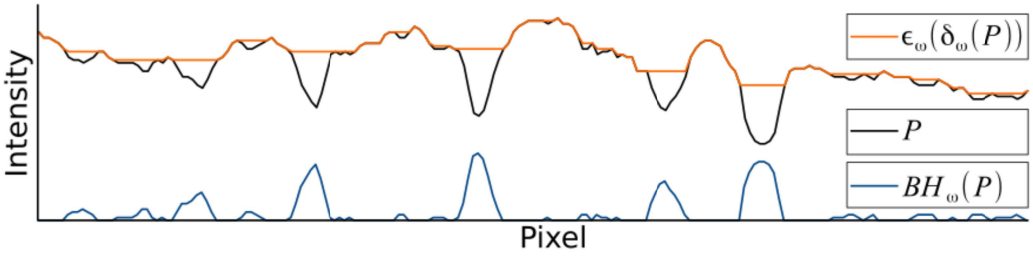

Figure 10. The result of the bottom-hat operation on a sample cross-section profile.

point (x,y), Φ is the vector of the cross-section orientations as defined earlier, and *MA_diam* is the maximal MA diameter parameter.

3.2.2 Construction of the microaneurysm score map

The common approach in the literature is to consider either the maximal top-hat or minimal bottom-hat response over the directions for coarse MA segmentation. The reason of this approach is that since MAs are circular structures, theoretically, they should have high similar responses at all levels. This can be observed in Fig. 11, which shows six MAs and their *BH-DRV*s. However, contrary to the literature approaches, here we determine the ratio of directions where the response levels of the corresponding cross-section profiles were at least $h \in \{1 \dots 255\}$ (assuming an 8 bit intensity image). For this purpose, we define the response ratio maps (*RRM*) as

$$RRM_h(x,y) = \frac{\sum_{i=1}^{|\Phi|} \begin{cases} 1, & \text{if } BH\text{-}DRV_{x,y}[i] \geq h, \\ 0, & \text{otherwise}. \end{cases}}{|\Phi|} \tag{3.6}$$

The likelihood of whether a point corresponds to an MA at a given response level h is derived from the corresponding *RRM* using another grayscale

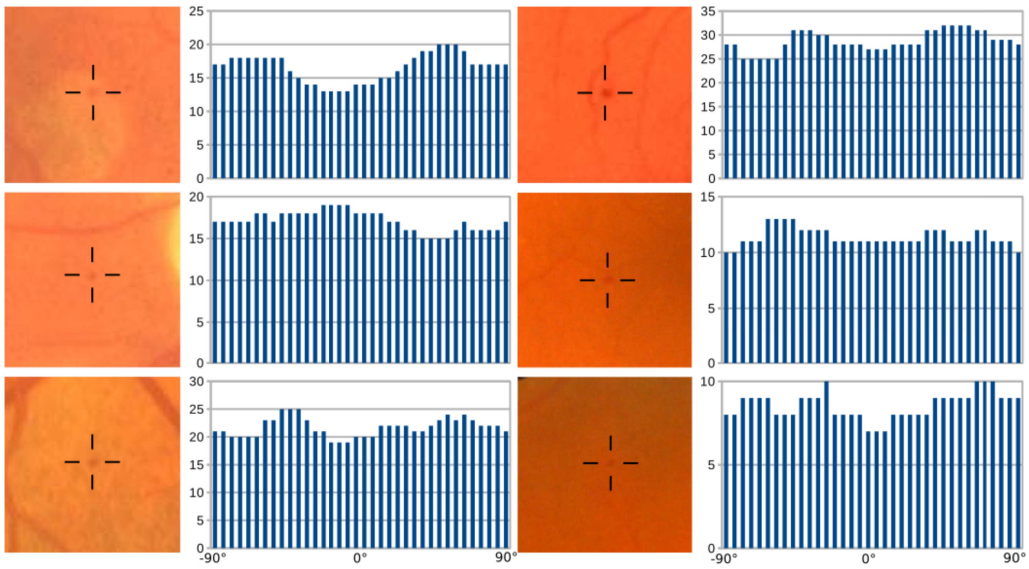

Figure 11. Bottom-hat directional response vectors of six microaneurysm centroids.

morphology operator, the diameter opening [32][107]. This operation removes those structures from an image whose diameter is larger than a given threshold. The subtraction of the diameter opened image from the original one gives its top-hat transform. One of the possible implementations is based on the successive lowering of the threshold around the local maxima, with testing the diameter of the region at each level. The procedure stops when the region exceeds the given size. This technique, which sometimes is referred to as flooding simulation, may also be interpreted as a kind of region growing. The difference is that the stopping criterion is not based on the local intensity difference, but on the diameter of the region. When applying this diameter opening top-hat operation on the response ratio maps, it can be seen that only those local maxima can correspond to MAs, whose value is close to 1.0. That is, the procedure can be significantly accelerated by considering only those points, whose response ratio is at least, for example, 0.9. Additionally, values of the non-zero connected components of the resulting top-hat are multiplied with the largest value within their region. This step further ensures that MA regions would achieve higher scores. Let LM_h denote the MA likelihood map obtained by applying the described modified diameter opening top-hat operation on RRM_h.

The final MA score map is constructed using a weighted pixel-wise maximum selection of the MA likelihood maps corresponding to different height levels. Formally,

$$score_{MA}(x,y) = LM_{h_{max}(x,y)}(x,y) \cdot h_{max}(x,y) \text{ , where} \tag{3.7}$$

$$h_{max}(x,y) = argmax_j LM_j(x,y) . \tag{3.8}$$

That is, the final MA score map is constructed by considering all possible height levels. Based on experimental observations, it was found to be sufficient to consider only the first 30 response levels ($l = 1,\ldots,30$).

The final MAs may be extracted by thresholding the score map, or by considering all its local maxima with the corresponding values in case if the expectation is to produce a set of coordinates with probability values. The experimental results of this MA detector together with the other one presented

in section 3.3 are discussed together in section 3.4.

3.3 MA detection through the direct analysis of rotating cross-section profiles

A brief summary of the second proposed solution for MA detection MADET2 is as follows. The core of the operation is to examine the local surroundings of the regional minimums of the green intensity plane through a direct analysis of their directional cross-section profiles. Since every MA has to have at least one pixel within its area that is a local minimum in the intensity domain, the candidate extraction simplifies to the extraction of the minimum regions of the image. This task can be accomplished very efficiently using available literature methods. Peak detection is applied on the individual cross-section profiles, and subsequently, a set of attributes regarding the size, height, and shape of the peak are calculated. The statistical measures of these attributes as the orientation of the cross-section changes constitute the feature set that is used to classify the candidates. A formula for the final score of the remaining candidates is given, which can be thresholded further to obtain a binary output.

In following sections, the detailed description of each step of the method is given. Also, a schematic diagram of the workflow is shown in Fig. 12.

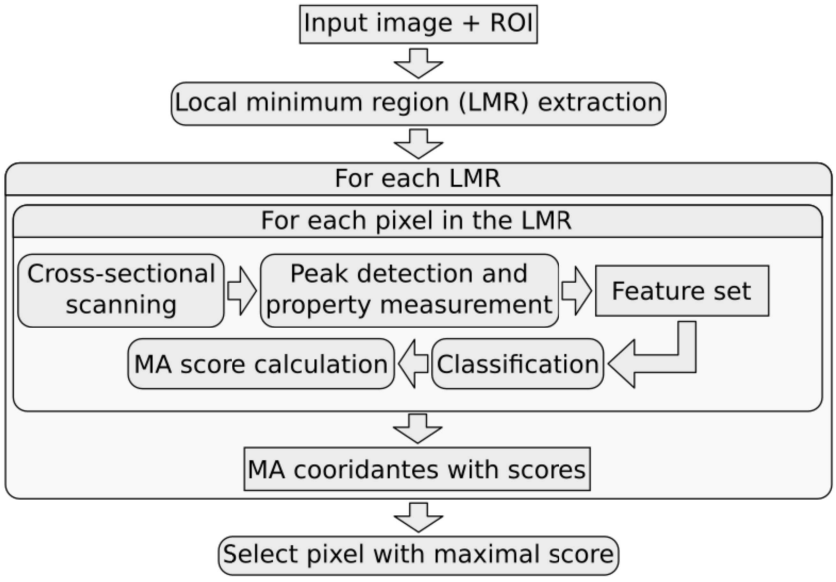

Figure 12. The workflow of MA detector MADET2.

3.3.1 Local minimum region extraction

MAs are local intensity minimum structures on the green channel retinal image, usually with a Gaussian-like intensity distribution. This means that every MA region contains at least one regional minimum as well. A local minimum region (*LMR*) of a grayscale (intensity) image is a connected component of pixels with a constant intensity value, such that every neighboring pixel of the region has a strictly higher intensity [108]. Consequently, it is sufficient to consider only the *LMR*s of the preprocessed image as possible MA candidate regions. While this approach may seem to be straightforward, it has not been used directly for MA candidate extraction before. However, the operation of the diameter closing method used by Walter et al. [31] did influence the proposed approach. As it has been discussed in section 3.1, the most practical implementation of this operation is based on the recursive extension of image minimum regions, known as the flooding simulation.

In order to extract *LMR*s, a simple breadth-first search algorithm was used. Its operation is similar to the one described in [108] for the calculation of grayscale morphological reconstruction. The procedure may be described briefly as follows. Pixels of the image are processed sequentially, and compared to their 8-neighbors. If all neighbors have higher intensities, then the pixel itself is an *LMR*. If there is a neighboring pixel with lower intensity, then the current pixel may not be a minimum. A pixel is considered to be a possible minimum if all neighboring pixels have higher or the same intensity, in which case pixels with the same intensity are stored in a queue and tested in the same way. If the queue becomes empty, so that all the pixels it contained proved to be possible minima, then the corresponding connected component is an *LMR*. The pseudo-code of the procedure is given in Algorithm 1. The variable *processed* refers to a flag map with the same size as the input image and is initially filled with zeros.

Pixels of an *LMR* are considered individually as possible MA candidates and the pixel with the maximal final score will represent its region. This procedure is referred to as non-maximum suppression and it will be discussed in more details later on. Image smoothing as discussed in section 3.1 gains importance

Algorithm 1. Extracting the local minimum regions of an image.

Input:

- *I*: a grayscale intensity image.

Output:

- *res:* the set of local minimum regions.

```
for p in points of I do
   if processed[p] = 1 then continue
   queue.add(neighbors of p)
   is_minimum ← 1
   region.clear
   region.add(p)
   while |queue| > 0 do
      cp ← queue.pop
      if I[cp] < I[p] then
         is_minimum ← 0
         break
      endif
      if I[cp] > I[p] then processed[cp] ← 1
      if I[cp] = I[p] then
         if processed[cp] = 1 then
            is_minimum ← 0
            break
         endif
         region.add(cp)
         processed[cp] ← 1
         for np in neighbors of cp
            if (not region.contains(np)) and (not queue.contains(np)) then
               queue.add(np)
            endif
         endfor
      endif
   endwhile
   if is_minimum = 1 then result.add(region)
endfor
```

at this point of the procedure, since the local intensity variations may be high in a raw retinal image, causing many local minima and longer execution times.

3.3.2 Cross-sectional scanning

In order to examine the surroundings of a single minimum pixel in an MA candidate region, the cross-sectional approach defined in section 3.1.1 is considered again. In [80], Ricci and Perfetti has described a similar procedure as a basic line detector. The authors there reported that they achieved the best

performance with lines of length 15 pixels with also referring to the method proposed in [23], where line operators of the same length are used as structuring elements for vessel segmentation. While in that approach the average intensity along the lines are considered, here we use the resulting intensity profiles to detect and measure the properties of a peak at its center. An additional advantage of this procedure is that it is not that critical to find an optimal length for the cross-section lines, though it has to be sufficiently large to enable the distinction of MAs from haemorrhages and parts of the vasculature.

3.3.3 Peak detection and property measurement on the cross-section profiles

A unique peak detection step is performed on the extracted cross-section profiles. The aim is to decide whether a peak is present at the center of the profile for a specific direction. Several properties of the peak are calculated and the final feature set consists of a set of statistical measures that show how these values vary as the orientation of the cross-section is changing. This way, the variation of important characteristics such as symmetry and shape of the structure, and also its difference from the background may be numerically expressed.

The detection of peaks in one dimensional discrete data is a common task in many fields of science. Such examples are the automatic evaluation of spectrometric [109], [110], chromatographic [111], [112], and cardiographic data. It also has a wide range of applications in signal processing. Localizing peaks in image histograms is used in many cases, e.g. for image segmentation or quantization. The applied methods are of many kinds and usually the most suitable for a specific problem, though the expectations towards a method also vary among the applications. The available methods in the literature include e.g., template matching, wavelet transformation, statistical approaches, baseline corrections, and thresholding.

The basis of the peak detection procedure proposed in this work is to locate strictly monotonic segments (ramps) of the profile. A ramp here is defined as a segment $(P[m],\ldots,P[n])$, with $-r \leqslant m < n \leqslant r$ of the profile *P*, such that,

$$sign(P[i]-P[i-1])\cdot sign(P[i+1]-P[i])=1 \tag{3.9}$$

for every $m<i<n$, where the sign function is defined as

$$sign(x)=\begin{cases}-1, & if\ x<0,\\ 0, & if\ x=0,\\ 1, & if\ x>0.\end{cases} \tag{3.10}$$

In other words, a ramp should be monotone increasing or decreasing. Moreover, the absolute difference between consecutive ramp values should not be less than *min_diff*, and the height of the ramp, i.e., the absolute difference between the first and last value should not be less than *min_height*, either. That is,

$$|P[i+1]-P[i]|\geq min\_diff \tag{3.11}$$

for every $m\leqslant i<n$, and

$$|P[m]-P[n]|\geq min\_height\ . \tag{3.12}$$

The value of *min_diff* acts as a lower threshold for the slope of the ramps, and it controls how sharp the recognized intensity transition should be. The purpose of the parameter *min_height* is to give a lower noise threshold. After examining the cross-section profiles of several retinal MAs, it was found that by setting *min_diff* to 2, and the *min_height* to 3, small monotonic segments that are clearly noise artifacts can be eliminated. The pseudocode for the ramp localization procedure is given in Algorithm 2. The method also uses a *state* variable, which gets its value from the function *sign*, denoting that whether the current ramp is increasing or decreasing, respectively. The localized ramps are stored in a queue in the form of (*start index*, *end index*, *ramp type*), where *ramp type* also gets its value from the variable *state*.

For the sake of better understanding, let us consider the inverted cross-section profiles as the basis of the ramp and the consecutive peak detection. This way, peaks corresponding to MAs become positive. Once the ramps are located, it is tested, whether a definite peak can be located at the center of the profile. The peak is considered to be present, if the rightmost ramp on the left of the central pixel is increasing, and similarly, the leftmost ramp on its right is decreasing. Since only minimum regions are considered as candidates, it is not possible that the central index (0) of the profile is inside a ramp, though, it may be the end or the start of one. Furthermore, increasing ramps to the left and

Algorithm 2. Ramp detection procedure on a profile.

Input:

- *P*: an intensity profile, the indexes of first and last value are *-r* and *r*, respectively.
- *min_diff*, *min_height*: method parameters.

Output:

- *ramps:* the result queue, whose elements are in the form of (*start index*, *end index*, *ramp type*).

```
state ← 0
for i in {-r, …, r – 1} do
   diff ← P[i + 1] - P[i]
   if state = 0 then
      if abs(diff) >= min_diff then
         height ← abs(diff)
         start ← i
         state ← abs(diff)
      endif
   else
      if state = sign(diff) then
         if abs(diff) >= min_diff then
            height ← height + abs(diff)
            if i = n – 2 and height >= min_height then
               push (start, i + 1, state) to ramps
            endif
         else
            if height > min_height then
               push (start, i + 1, state) to ramps
            endif
            state ← 0
         endif
      else
         if height >= min_height then
            push (start, i + 1, state) to ramps
         endif
         if abs(diff) >= min_diff then
            height ← abs(diff)
            start ← i
            state ← sign(diff)
         else
            state ← 0
         endif
      endif
   endif
endfor
```

decreasing ramps to the right of the detected peak are successively attached as long as the gap between two consecutive ramps is not greater than a fixed value *max_gap*. This way, a more noise and local intensity variation tolerant peak detection can be achieved. In the implementation, the parameter *max_gap* was

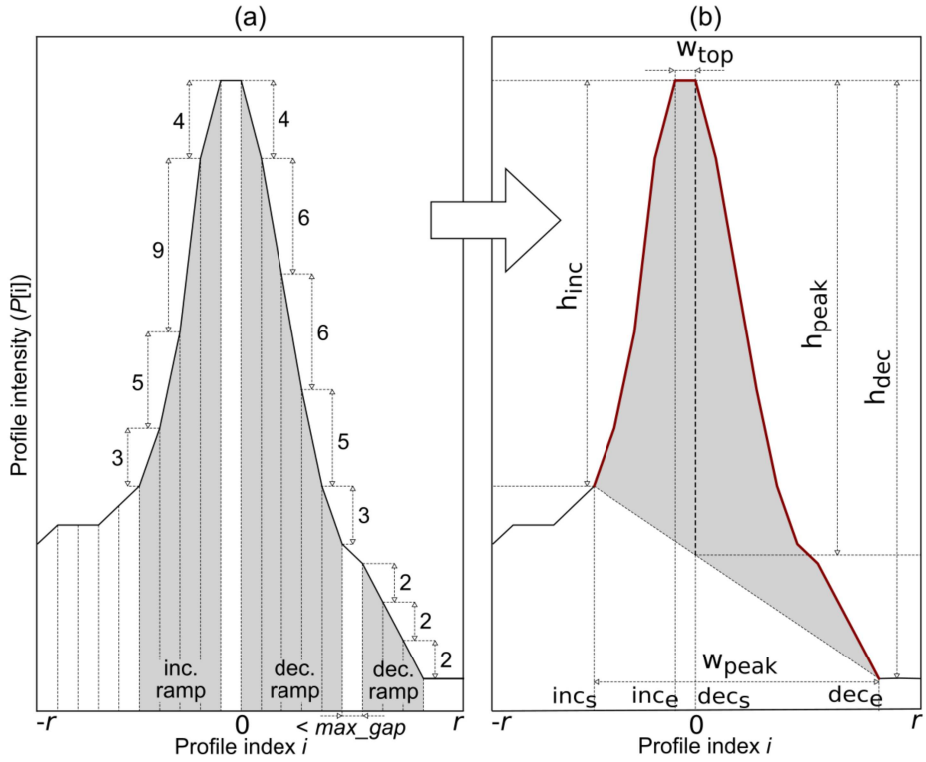

Figure 13. Increasing and decreasing ramps on a sample profile (a), and the result of the peak detection and the calculated peak measures (b).

set to 3, which was also determined based on experimental observations, in the same way as in the case of the parameters *min_diff* and *min_height*. The final peak is represented by four descriptive values: inc_s, inc_e, dec_s, and dec_e. The values of inc_s and inc_e correspond to the start and end indices of the increasing ramp, while dec_s, and dec_e correspond to the boundaries of the decreasing ramp, respectively. Fig. 13 shows a graphical interpretation of the ramps on an inverted sample cross-section profile (Fig. 13 (a)), and how the full peak is formed (Fig. 13 (b)).

Once a peak is detected at the center of a profile *P*, the following features are calculated:

1. The *peak width* is the difference between the start and end indices of the peak:

$$w_{peak} = dec_e - inc_s ; \tag{3.13}$$

2. The *top width* is the size of the gap between the increasing and decreasing ramp:

$$w_{top} = dec_s - inc_e \, ; \tag{3.14}$$

3. The *increasing ramp height*:

$$h_{inc} = P[inc_e] - P[inc_s] \, ; \tag{3.15}$$

4. The *decreasing ramp height*:

$$h_{dec} = P[dec_s] - P[dec_e] \, ; \tag{3.16}$$

5. The *increasing ramp slope*:

$$s_{inc} = h_{inc} / (inc_e - inc_s) \, ; \tag{3.17}$$

6. The *decreasing ramp slope*:

$$s_{dec} = h_{dec} / (dec_e - dec_s) \, ; \tag{3.18}$$

7. The *peak height* is calculated as the difference between the intensity of the central pixel and a baseline that connects the start and end of the profile:

$$h_{peak} = P[0] + \frac{P[dec_e] - P[inc_s]}{w_{peak}} \cdot inc_s + P[inc_s] \, . \tag{3.19}$$

The value of *peak width* corresponds to the extension of the structure in the given direction. The *top width* measures how large the maximum area in the structure is. The *heights* and *slopes* of the increasing and decreasing ramps provide information about the distinction from the surroundings, and the sharpness of the intensity transition, respectively. We note that the slope is considered to be positive for decreasing ramps, too. The value *peak height* combines the heights of the increasing and decreasing ramps by fitting a baseline to the peak and calculating the difference of the profile's central value from it. The calculated peak measures – except the slopes – on the previous sample cross-section profile are shown in Fig. 13 (b).

3.3.4 Feature set and classification

After the cross-sectional scanning and peak detection steps are performed for every scan direction on a given candidate point, several statistical measures of the resulting directional peak properties are calculated. For this purpose, the following five sets that consist of the values of the corresponding peak features are defined. The increasing and decreasing ramp height values are stored jointly in the set *RHEIGHTS* set, likewise, the ramp slope values are stored in *RSLOPES*. The sets *TWIDTHS*, *PWIDTHS*, and *PHEIGHTS* contain the values *top width*, *peak width*, and *peak height*, respectively.

Let μ_T, σ_T, and cv_T denote the respective mean, standard deviation and coefficient of variation of the values in a set *T*. The the coefficient of variation *cv* is the normalized measure of dispersion, and is defined as the ratio of the standard deviation and the mean, i.e.,

$$cv_T = \frac{\sigma_T}{\mu_T} \tag{3.20}$$

The following feature set containing seven elements constitutes the basis of candidate classification:

$$F = \{\mu_{PWIDTHS}, \sigma_{PWIDHTS}, \mu_{TWIDTHS}, \sigma_{TWIDTHS}, \sigma_{RSLOPES}, cv_{RHEIGHTS}, cv_{PHEIGHTS}\}. \tag{3.21}$$

The value of $\mu_{PWIDTHS}$ gives a good measure of the extension of the candidate object, and $\sigma_{PWIDTHS}$ shows how symmetric it is. $\mu_{TWIDTHS}$ and $\sigma_{TWIDTHS}$ serve similar purposes by describing the inner region of the candidate. $\sigma_{RSLOPES}$ has a higher value for vessel crossings. The $cv_{RHEIGHTS}$ and $cv_{PHEIGHTS}$ values provide normalized measures of the variations in the sharpness of the contour. This feature set made it possible to distinguish MAs from the most common interfering objects, such as small disconnected vessel fragments, vessel crossings and bifurcations, retinal haemorrhages that are only slightly larger than MAs, or local darkenings on the vessels.

For classification, a naive Bayes (NB) classifier has been used. This is a simple, yet robust probabilistic algorithm that assumes the individual features to be independent. The training set consists of both positive and negative MA

examples. Usually, it is rather straightforward to obtain the feature vectors of positive instances of the training set, since in most public datasets the coordinates of MAs on the images are given. The non-MA set was assembled manually and consists of the previously described most common false positives from the training images of the publicly available Retinopathy Online Challenge dataset [105]. The used image sets are discussed in details in the experimental results section 3.3.

The training of a NB classifier is based on the estimation of the class priors and feature probability distributions. Following the common practice in the literature when dealing with continuous data, we assume that the feature values in each class are of Gaussian distribution. This yields that the parameters of the distribution can be estimated using the sample means and variances of the training data for the given feature. That is, for each class $c \in \{MA, non\text{-}MA\}$ we determine $\{\mu_{F_i,c}, \sigma^2_{F_i,c}\}$, where F_i denotes the set of the values of the i^{th} feature in *F*. Class priors in this case are considered to be equal, i.e., we assume that both MA and non-MA cases occur with the same frequency. Thus, this term may be ignored in the final decision, which further simplifies the procedure.

The NB classification of a new candidate represented by the feature vector $(f_1, \ldots, f_7)$ is described using the formula

$$classify(f_1, \ldots, f_7) = \underset{c}{argmax} \prod_{i=1}^{7} p(f_i|c), \tag{3.22}$$

which is known as the maximum *a posteriori* decision rule. According to the assumption of normal distribution in the individual features, the probability of f_i over c is expressed as

$$p(f_i|c) = \frac{1}{\sqrt{2\pi\sigma^2_{F_i,c}}} e^{-\frac{(f_i - \mu_{F_{i,c}})^2}{2\sigma^2_{F_{i,c}}}}. \tag{3.23}$$

Other classification methods, such as k-nearest neighbor (kNN) and support vector machines (SVMs) with different kernel functions have been checked as well. Experiments showed that there was only a minimal difference in the final

performance, though the usage of NB gave a slightly better result. Besides, its low computational time and robustness are also advantageous properties. However, the intention of these experiments was not to find the most suitable classification method, but much rather to show the capability of the proposed feature set in terms of expressing the important characteristics of MAs.

The training set, the different classifier results, and the performance evaluation methodology will be discussed in details in the experimental results section 3.4.

3.3.5 MA score calculation and non-maximum suppression

In order to meet the requirements of a real-life DR screening system, scores are assigned to the MA candidates that were classified as true MAs. This score considers the shape, symmetry, sharpness, and contrast of the candidate. It is constructed in such a way that stronger and more visible MAs achieve higher scores than faint ones. It has been experimentally found that the product of the minimal value of *PHEIGHTS*, denoted as $min_{PHEIGHTS}$, and μ_{SLOPES} reflects well the strength of the appearance of the candidate. Note that the usage of the minimum of the directional peak heights is analogous to the minimum of rotated morphological bottom-hats discused earlier in the overview of the literature methods. The final MA score is calculated using the formula:

$$score_{MADET\,2} = \frac{min_{PHEIGHTS} \cdot \mu_{RSLOPES}}{1 + \sigma_{PWIDTHS} + \sigma_{TWIDTHS} + \sigma_{RSLOPES} + \sigma_{RHEIGHTS} + \sigma_{PHEIGHTS}} . \quad (3.24)$$

The score calculated in this way will be maximal when the variables in the denominator are equal to zero. It will assign higher scores to locally more distinctive candidates with sharper edges, and it takes into consideration that variation in the important features should be as low as possible as well. Notice that opposed to the feature set used for classification, in (3.21) the standard deviations of *RHEIGHTS* and *PHEIGHTS* are considered instead of their coefficients of variation. Since these values express the contrast of the candidate, for the classification step it is more suitable to consider their normalized variants. In the case of classification, the aim is to decide whether the candidate is a valid MA and not to express how prominent it is, for which

purpose the normalized dispersion measure is more suitable. The variables in the denominator of (3.24) are of different ranges, thus, one might consider some sort of normalization in order to bring the values, e.g., into the range of [0,1]. The necessary min/max values of the corresponding terms can be derived from the training data. However, for the experiments reported here, no normalizations were used.

The final step of the proposed method is referred to as the non-maximum suppression of the scores. It has been described earlier that in the case of a regional minimum, all of its points are considered individually as candidate points. Non-maximum suppression thus means the operation of selecting the point with the highest score from every minimum region that will represent the corresponding candidate. Therefore, points with non-maximal score in a candidate region are neglected, and the output of the proposed MA detection method is a set of coordinates along with the corresponding score values. In most of the cases the point with the highest score is also the centroid of the MA. It is rather rare that instead of a single minimum point a larger region would be present in the case of MAs.

In order to achieve a binary output for the MA candidates, simple thresholding of the score values may be performed. This score threshold may also be interpreted as the discriminative threshold of the entire system, which gives the opportunity to FROC analysis. Optionally, it may be useful to apply statistical normalization on the score maps, and thus a global threshold can be defined for the system.

3.4 Experimental evaluation of the MA detection methods

The presented detection methods MADET1 and MADET2 have been tested on two independent image sets: in an open online competition and on a private image set that was provided by the Moorfields Eye Hospital, London, UK. No additional vessel or optic disc detections were applied for these tests.

3.4.1 Materials and classifier configuration

The presented methods were optimized primarily for the Retinopathy Online Challenge (ROC) [105], which is an international online competition dedicated to objectively compare the accuracy of retinal microaneurysm detectors under the same conditions. The publicly available image set of the ROC challenge consists of 50 training and 50 test images, both are of three different spatial resolutions: 768×576, 1058×1061, 1389×1383 pixels. The field of view (FOV) of the images is 45°, and all images are compressed with JPEG. The coordinates of the MAs are available only for the training set, which can be used as a ground truth. This setup gives each participating team the opportunity to train their methods on the training set, and then submit their results obtained on the test set. The output of the methods should be in the form of pairs of candidate coordinates and confidence values. The performance of a method is calculated as the average sensitivity at seven predefined false positive per image rates (1/8, 1/4, 1/2, 1, 2, 4, and 8) by the ROC providers.

The method MADET2 presented in section 3.2 applies a two-class classification; therefore, it requires two sets of training examples. Assembling the positive set (*MA*) is straightforward. However, compilation of the negative set (*non-MA*) is more complicated, since its elements have to be selected manually. To construct the training feature set for the classifier of the proposed method, the official annotations of the MAs on the training set were taken as a basis, and the ambiguous ones were sorted out manually. The set *non-MA* was assembled manually and consisted mostly of vessel crossings and bifurcations, elongated disconnected vessel fragments, and haemorrhages. Table 1 shows the means and standard deviations of the feature values for the two classes in the training data. Since a naive Bayes classifier with the assumption of normal

Table 1. Means and standard deviations of the training feature vectors for the MADET2 method.

Feature	***MA***	***non-MA***
$\sigma_{RSLOPES}$	0.7623 ± 0.1280	1.2522 ± 0.6934
$cv_{PHEIGHTS}$	0.1989 ± 0.2407	0.3329 ± 0.0476
$cv_{RHEIGHTS}$	0.2594 ± 0.0375	0.4389 ± 0.0369
$\mu_{TWIDTHS}$	1.2095 ± 7.3803	1.7283 ± 3.3291
$\sigma_{TWIDTHS}$	0.7459 ± 1.3820	1.6078 ± 2.4946
$\mu_{PWIDTHS}$	8.5987 ± 7.0796	11.7989 ± 7.5289
$\sigma_{PWIDTHS}$	1.8159 ± 1.1965	3.7547 ± 2.7767

distribution of the individual features were used, these mean and standard deviation values constitute the configuration of the classifier as well.

During development, other classifiers have also been checked. This was done by evaluating on the ROC training set, since the MA annotations are not available for the images in the test set. Using the aforementioned NB classifier, an average sensitivity of 0.1509 was achieved, while in the cases of a k-nearest neighbor (k=15, statistically normalized feature vectors) and an SVM classifier with radial basis kernel function (libSVM [113] default settings) these figures were 0.1500 and 0.1490, respectively. It can be seen that the difference between the considered classifiers was minimal. Speed and robustness were also in favor of choosing NB eventually.

Besides the competition ROC, both methods have been tested on a set of images provided by the Moorfields Eye Hospital, London, UK. This image set consists of 60 retinal images and the coordinates of the MA centroids are also available for all the images. The FOV of the images is 45°, and the diameter of their ROI is approximately 2200 pixels on average. In order to evaluate the presented supervised method on this dataset, the same classifier setup was used as for the ROC. Hence, it was possible to test on all the 60 images without splitting them into a training and test set. In the case of the ROC, certain lesions are considered as “irrelevant” by the organizers, and thus, their detections are not counted as false positives. However, in the case of the annotation of the

Moorfields images, no such category was considered.

3.4.2 Results

In the challenge ROC, the unsupervised method MADET1 presented in section 3.1 [8] achieved an average sensitivity 0.355, while the method MADET2 presented in section 3.2 [9] achieved 0.423, both evaluated by the organizers. Table 2 summarizes the performance of the methods that have been submitted to the competition so far. The first placed method DRSCREEN [48] is an ensemble-based technique, which combines several individual algorithms, including the unsupervised MADET1, as well. While the average sensitivity of the ensemble-based method is slightly higher, it is important to mention that the presented supervised method achieved higher sensitivity at the diagnostically most important low average false positive per image rates, i.e., at 1/8 and 1/4 *FP*s/image. Table 3 shows the sensitivities of the two MA detection methods in this dissertation and the first placed ensemble-based one at the seven average false positive per image rates.

The evaluation protocol of the Moorfields images is that no false detections are considered as “irrelevant”. This resulted in a lower sensitivity at the same average false positive per image levels, compared to the ROC. The average

Table 2. List of methods that have been submitted to the Retionapthy Online Challenge along with their average sensitivity at the predefined false positive per image rates.

	Method	**Average sensitivity**
1.	Antal and Hajdu (DRSCREEN) [48]	0.434
2.	**MADET2** [9]	0.423
3.	Niemeijer et al.[30]	0.395
4.	Quellec et al. [38]	0.381
5.	Giancardo et al. [41]	0.375
6.	Zhang et al. [35]	0.357
7.	**MADET1 [8]**	0.355
8.	Sánchez et al. [39]	0.322
9.	Mizutani et al. [37]	0.310
10.	IRIA-Group [33]	0.264

Table 3. Sensitivities at the predefined average false positive per image rates for the proposed method and the first placed ensemble-based one in the ROC challenge.

	1/8	1/4	1/2	1	2	4	8
MADET2 [9]	**0.251**	**0.312**	0.350	0.417	0.472	0.542	0.615
MADET1 [8]	0.169	0.248	0.274	0.367	0.385	0.499	0.542
Antal and Hajdu [48]	0.173	0.275	**0.380**	**0.444**	**0.526**	**0.599**	**0.643**

sensitivity of the method MADET1 was 0.117, while the technique MADET2 achieved 0.233 on this image set.

The *FROC* curves of the proposed methods based on the results obtained from the ROC organizers, and based on own experiments on the Moorfields images are shown in Fig. 14. and Fig. 15, respectively. Since the Moorfields images are not publicly available, we present an image from the image set that shows several pathologies in Fig. 16, with the true positive, false positive, and false negative detections highlighted, and the four false positives are also zoomed. The score threshold was chosen so that the number of average false positives per image was 2 in this experiment.

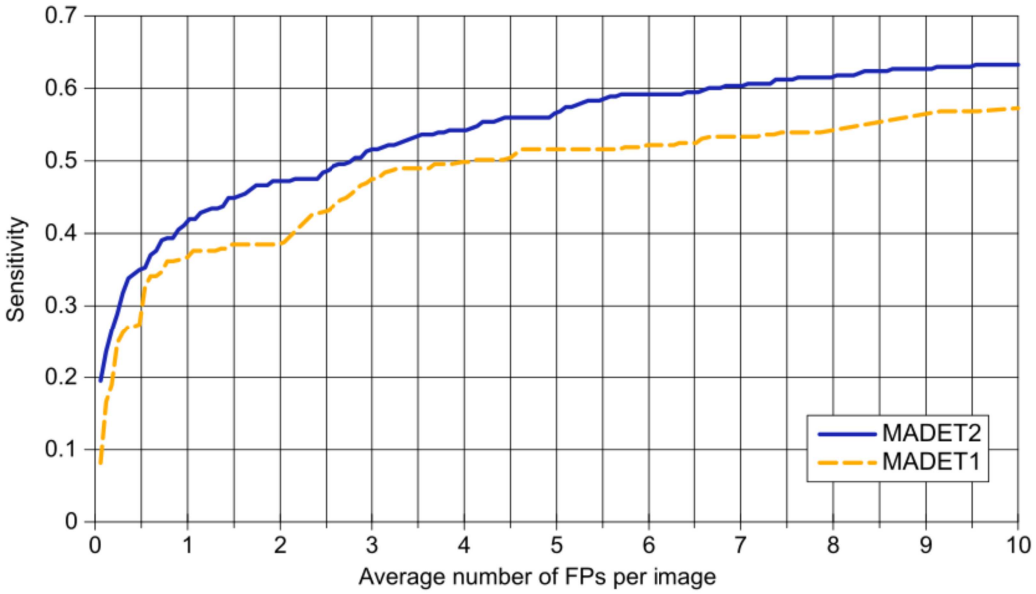

Figure 14. FROC curves of the proposed methods based on their results in the Retinopathy Online Challenge.

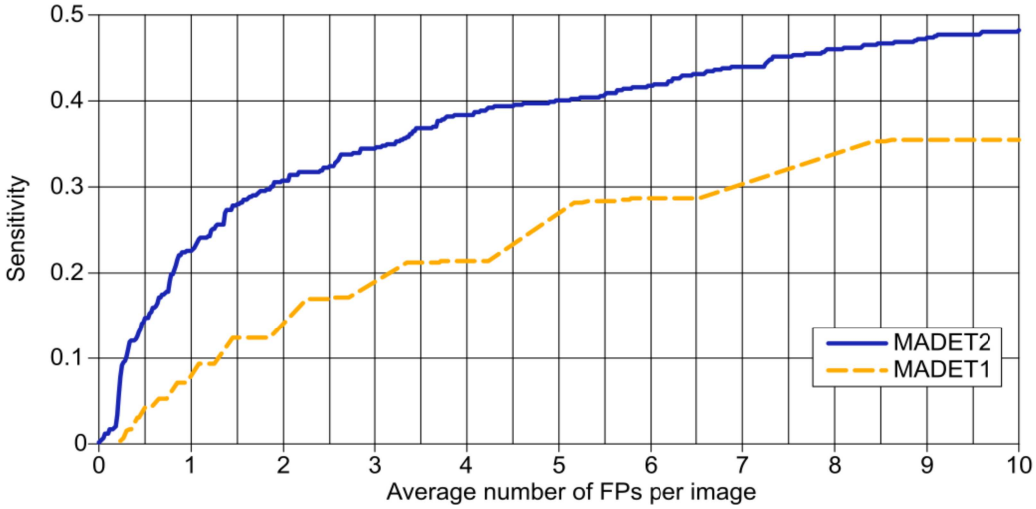

Figure 15. FROC curves of the proposed methods based on their results on the Moorfields images.

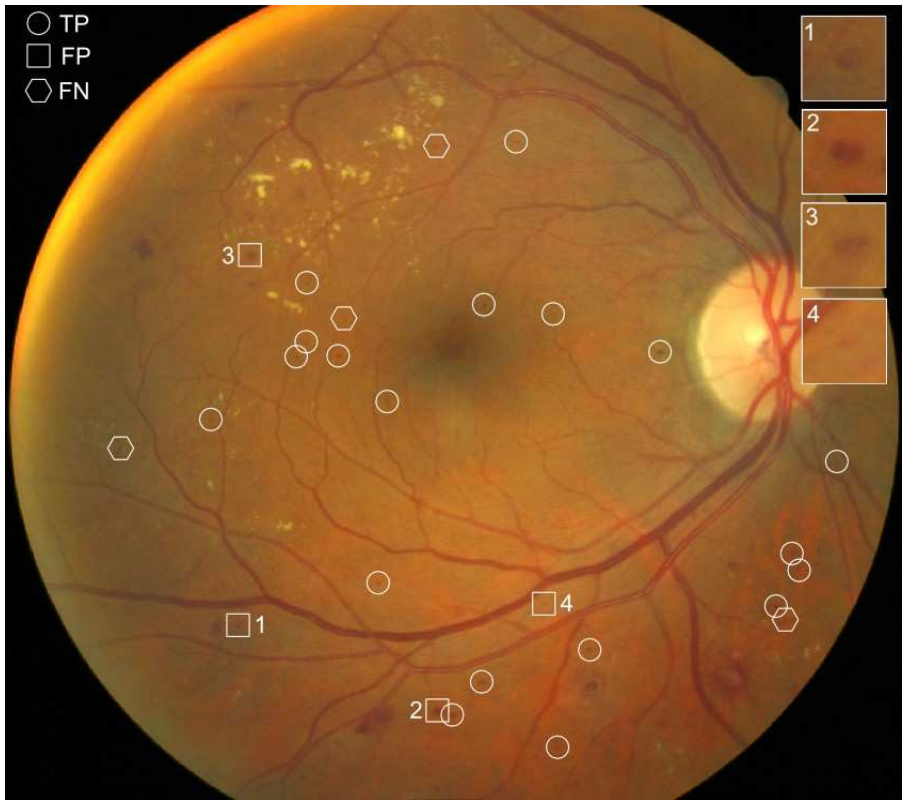

Figure 16. An image showing the result of the detection in the Moorfields Eye Hospital dataset. Four false positive detections are marked and zoomed.

The proposed method was implemented in Java SE 1.6. The average computational time was approximately 2 seconds per image without parallelization, using a desktop computer with an Intel® Core™2 Quad Q8200 Processor and 2 GB RAM. Since MA candidate regions may be processed independently, there are many points, where the method could be parallelized, such as the cross-sectional scanning step.

3.5 Summary of new scientific results in the field of retinal microaneurysm detection

1. An unsupervised MA detector based on the most fundamental directional morphology technique of the current literature has been developed. It makes it possible to segment MAs without any additional classification step using grayscale diameter opening on the data derived from the directional morphology responses. The algorithm takes only the maximal MA diameter as a parameter, which can be calculated based on the ROI diameter. Related publication: [8].
2. It has been shown that the candidate extraction phase of MA detection can be carried out by the extraction of the regional minima of the image intensities. Related publication: [9].
3. A novel MA detection technique has been proposed, which is based on the analysis of the directional cross-section profiles centered at the minima points of the image. A peak detection technique and several peak properties have been introduced. A feature set based on certain statistical measures of the peaks of cross-sections has been proposed and used for candidate classification. A formula for the final candidate score has been given that takes the symmetry, sharpness, and contrast of the candidate into consideration. Related publications: [9]–[12].

4 A NOVEL RETINAL VESSEL SEGMENTATION METHOD

This section presents a novel technique for retinal vessel segmentation. The proposed method is a directional multiscale approach, in some aspects similar to the literature techniques discussed in section 2.2 and the MA detection methods described in section 3. The main difference and novelty lie in the manner how the directional responses are utilized. While almost all available similar methods in the current literature consider only the maximal or summed directional responses at each pixel, the method presented here considers the directional responses of a pixel as a vector. The obtained information is utilized in several ways. A response vector correlation based similarity measure and its usage in a nearest neighbor classifier setup for filtering segmentation seed points are proposed. The segmentation procedure itself is a region growing technique which employs a directional response vector similarity constraint on adjacent pixels within the region. A vessel score measure is introduced which is more adequate for elongated structure recognition than simple maximum

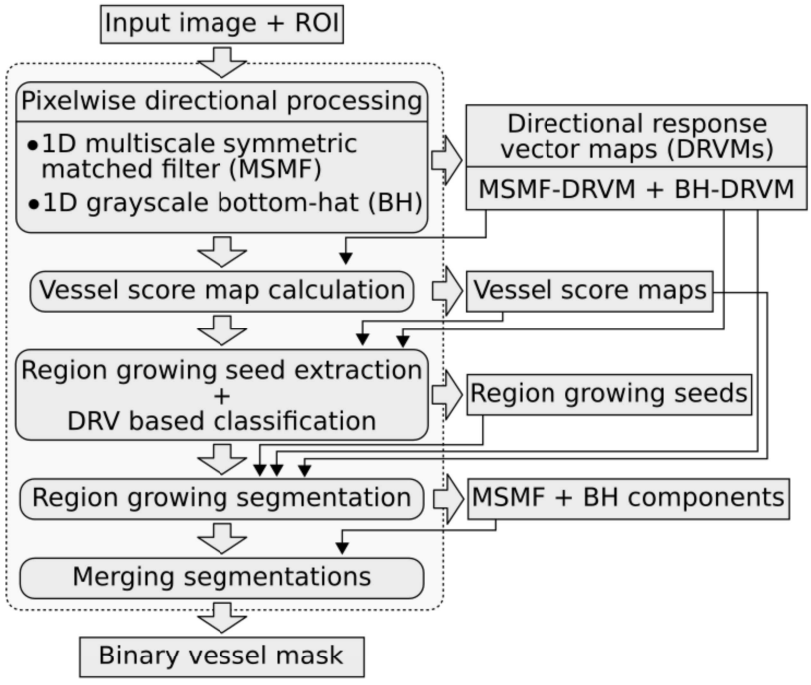

Figure 17. Workflow of the proposed retinal vessel segmentation method.

selection. Additionally, a symmetry constrained matched filtering approach is proposed as well, which overcomes the issue of false high responses to the steep intensity transitions at the border of the optic disc and bright lesions.

Next, in section 4.1, the detailed description of the proposed retinal vessel segmentation technique is given. A schematic workflow diagram of the main steps of the operation is shown in Fig. 17. Experimental results are presented in section 4.2. Finally, section 4.3 demonstrates how some components of the proposed vessel segmentation can be used in another field of medical image processing, namely the automatic segmentation of pigment networks in dermatoscopic images.

4.1 Segmentation based on directional response vector similarity and region growing

4.1.1 Inputs and preprocessing

The input of the vessel segmentation algorithm is the green channel of a color retinal image, preferably along with its binary ROI mask. While the ROI is not necessary, it can be used to exclude some spurious candidates at boundaries and to significantly lower the computational time by eliminating a large number of insignificant pixels. There are some spatial parameters of the method, which correspond to a certain ROI diameter, which is discussed in more details in section 4.2.1. These parameters either need to be adjusted if images of different ROI diameter are processed, or the images need to be rescaled accordingly. Similarly to the proposed MA detection approaches, this method does not require a specific preprocessing step either. Simple Gaussian smoothing with a standard deviation of 1.0 on the extracted green channel was applied in the implementation, though one might consider other image enhancement techniques depending on the quality of the input images.

4.1.2 Pixel-wise determination of the directional response vectors

In the first phase of its operation, the proposed method applies the same procedure to obtain cross-section profiles for each pixel which was described in section 3.1. There are two operations applied on all cross-sections of a pixel, both resulting in two directional response vectors for each profile. The

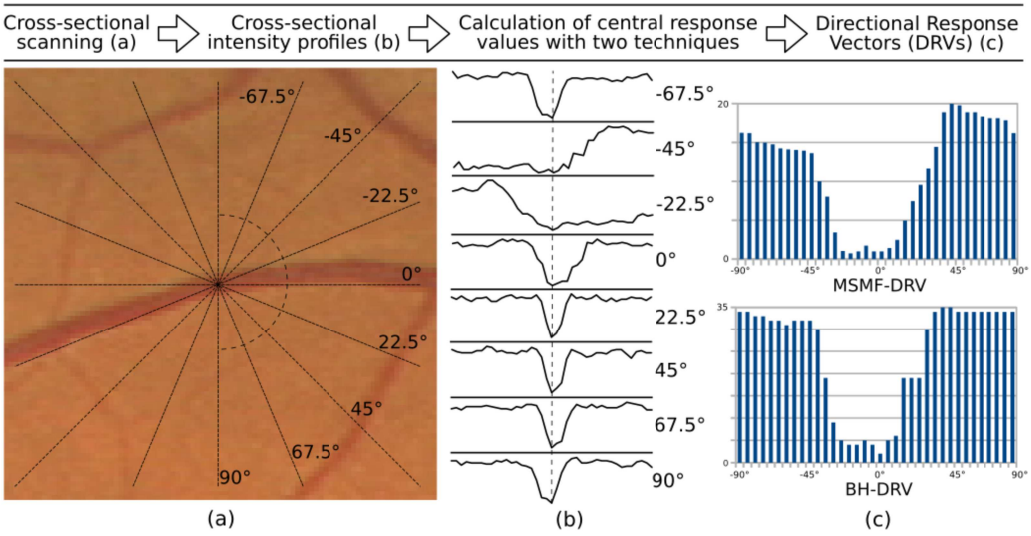

Figure 18. The workflow of the directional processing procedure with the schematic representation of some cross-section lines (a), the corresponding cross-section profiles (b), and the directional response vectors of the pixel under examination (c).

difference between this approach and the existing ones lies in the way how these directional responses are utilized. Namely, here the entire response vectors are used, instead of considering only the maximal or summed responses over the directions. Fig. 18 gives a depiction of the workflow of the directional processing.

The first operation to obtain directional responses is the same morphological bottom-hat operation that was described in section 3.2.1. The only difference is that the parameter in this case is the maximal vessel width and not the maximal MA diameter. The advantage of this simple morphological operation in the case of vessel extraction is that it gives almost no response for bright lesion edges and the optic disc boundary. Unfortunately, it does give high response to more irregular cross-sections, such as those of haemorrhages, and it is less susceptible for thin vessels.

The second technique used to obtain responses is a special matched filtering approach which is also a contribution of this dissertation and is described in the next section.

4.1.2.1 1D multiscale symmetric matched filter response

The second order derivative of the Gaussian (SDG) filter is widely used in signal and image processing tasks. Its negative normalized variant is often referred to as the *Mexican-hat* due to its shape. The two dimensional counterpart is known as the Laplacian of Gaussian (LoG) filter and is a fundamental tool in corner, blob and edge detection tasks. The one-dimensional filter function of the SDG with scale parameter σ can be given as

$$G''_{\sigma}(x)=\frac{\left(x^2-\sigma^2\right)}{\sigma^4}\cdot e^{\frac{-x^2}{2\sigma^2}} \tag{4.1}$$

Two favorable properties of the SDG filter are that it is zero-mean and the filter flattens out to zero. Hence, the response is less dependent on the size of the cross-section than it would be in the case of e.g. zero-mean Gaussian masks [68], [69]. The only constraint is that this size should be sufficiently large to allow the SDG filter with the largest scale to flatten out. This property can be observed in Fig. 19, which shows the plots of five SDG filters that correspond to different scale parameters.

In our presentation, we will use the same notations as described in section

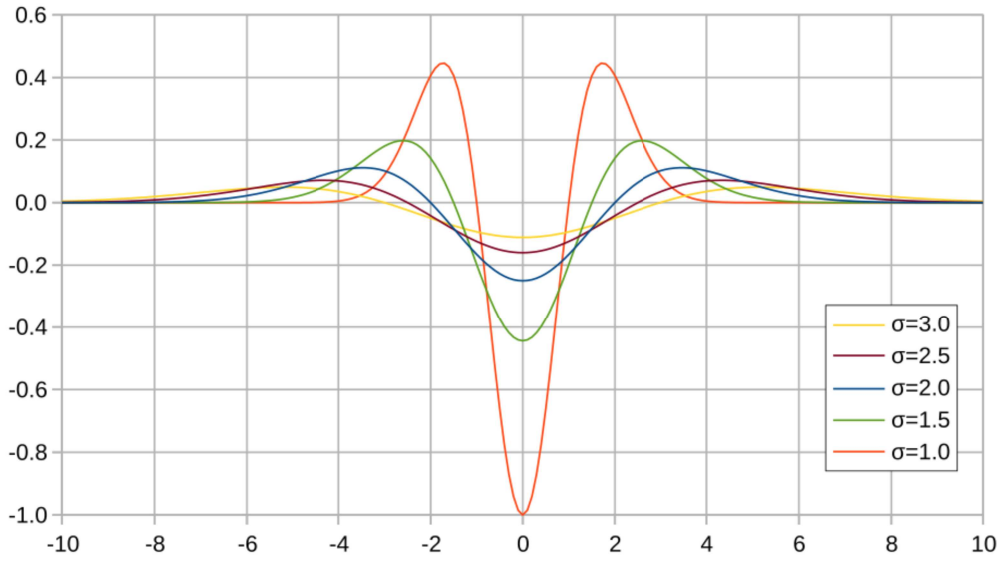

Figure 19. Second order derivative of the Gaussian (SDG) filters corresponding to different scale parameters.

3.1, i.e., P denotes a cross-section profile, $P[i]$ its i^{th} value, and $i \in \{-r, \ldots, r\}$, where r is considered to be the radius of the cross-section. The general way to calculate the matched filter response is the discrete cross-correlation of the signal and the mask. If both of them are real and the mask is central symmetric, this is the same as the discrete convolution, thus, both expressions occur in the literature. In this case, the size of the cross-section profile and the mask are equal, and since only the response at the central index is relevant, the operation simplifies to the sum-product of the two vectors. That is, the matched filter response for profile P with an SDG having parameter σ is

$$MFR_{\sigma}(P) = \sum_{i=-r}^{r} P[i] \cdot G''_{\sigma}(i) \,. \tag{4.2}$$

The most important drawback of this correlation based matching of directional SDG filters in the case of retinal images is the high response for asymmetric bright intensity transitions, such as those occurring at the boundary of the optic disc and bright lesions. This effect is sometimes referred to as the "ringing effect" in the corresponding literature [67], [76], [102]. The solution proposed here to overcome this issue is to split the sum-product to a left and right part, excluding the central element, and subtracting the absolute difference of these two from the entire response. Thus, a symmetry constraint is incorporated. In the case of an SDG filter, the sum-products may be negative, which would yield erroneous effects in later steps. Thus, in such case the response is considered to be zero. The formal description can be given as

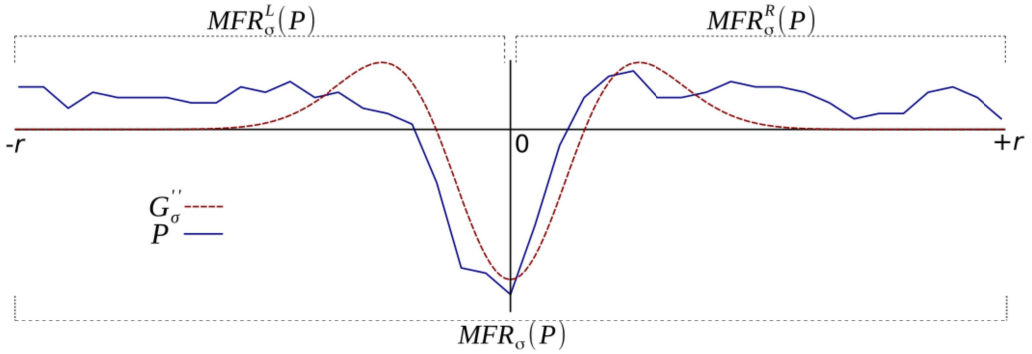

Figure 20. A vessel cross-section profile and an SDG filter along with the intervals for the calculation of the matched filtered response.

$$MFR_\sigma(P) = MFR_\sigma^L(P) + P[0]\cdot G_\sigma''(0) + MFR_\sigma^R(P)\text{, where} \tag{4.3}$$

$$MFR_\sigma^L(P) = \sum_{i=-r}^{-1} P[i]\cdot G_\sigma''(i)\text{, and} \tag{4.4}$$

$$MFR_\sigma^R(P) = \sum_{i=1}^{r} P[i]\cdot G_\sigma''(i)\,. \tag{4.5}$$

In order to help the better understanding of (4.3), (4.4)., and (4.5), Fig. 20 shows a vessel cross-section profile along with an SDG filter. The intervals for the determination of the left, right, and total sum-products are also indicated. This way, the symmetric matched filter response is expressed as:

$$SMFR_\sigma(P) = max(MFR_\sigma(P) - |MFR_\sigma^R(P) - MFR_\sigma^L(P)|, 0)\,. \tag{4.6}$$

To handle the varying width of vessels, SDG masks corresponding to different scale parameters are matched against the profile, and the maximal

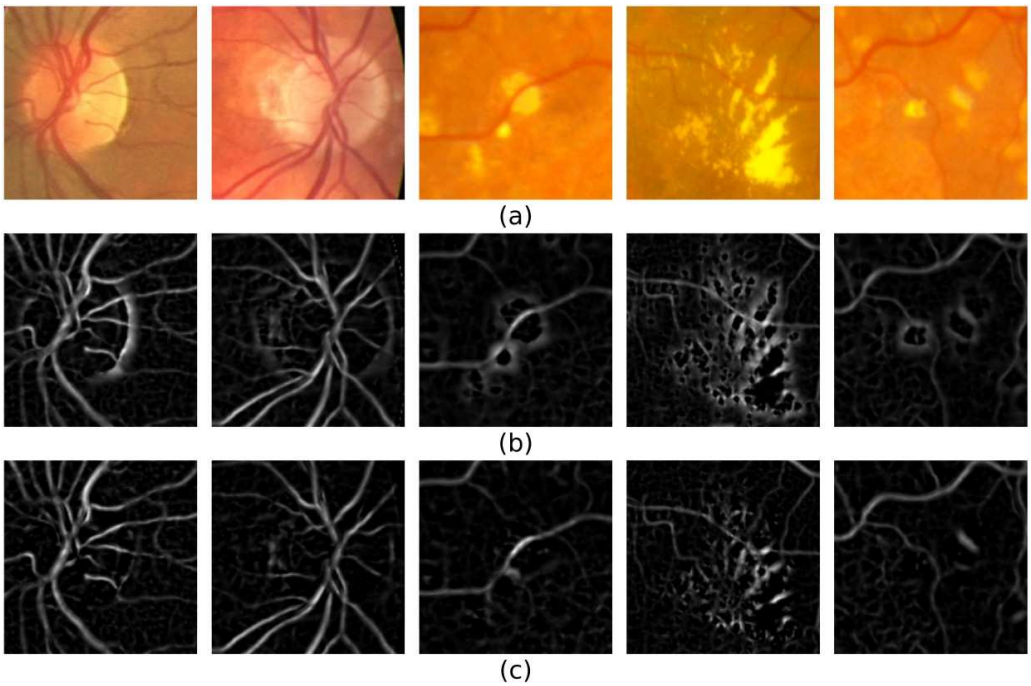

Figure 21. Parts of retinal images (a), the result of applying simple SDG filter (b), and the result of the proposed symmetric matched filter response calculation (c).

response is selected. Formally, the final multiscale modified matched filter (*MSMF*) response to *P* is given as

$$MSMFR(P) = max_{\sigma} SMFR_{\sigma}(P) . \tag{4.7}$$

In the test implementation, σ has been selected from the range $[1.0, 3.0]$ with a step 0.1. To demonstrate the effect of simple directional SDG filters and the proposed symmetry constrained technique, parts of retinal images containing optic discs and bright lesions are shown in Fig. 21, along with the results of the directional SDG and the proposed filtering technique. For this experiment, the maximal directional responses were selected at each point. In section 4.1.3.1, a more suitable formula is given, however, the superiority of the proposed *MSMF* for vessel enhancement is clearly visible even in this way.

4.1.3 Segmentation on the response vector maps

Resulting from the previous step, two directional response vector maps (*DRVM*s), the multiscale symmetric matched filter (*MSMF-DRVM*) and the bottom-hat (*BH-DRVM*) maps are obtained. The segmentation procedure described in this section is considered on both vector maps separately, and the resulting two primary vessel masks will be combined to form the final

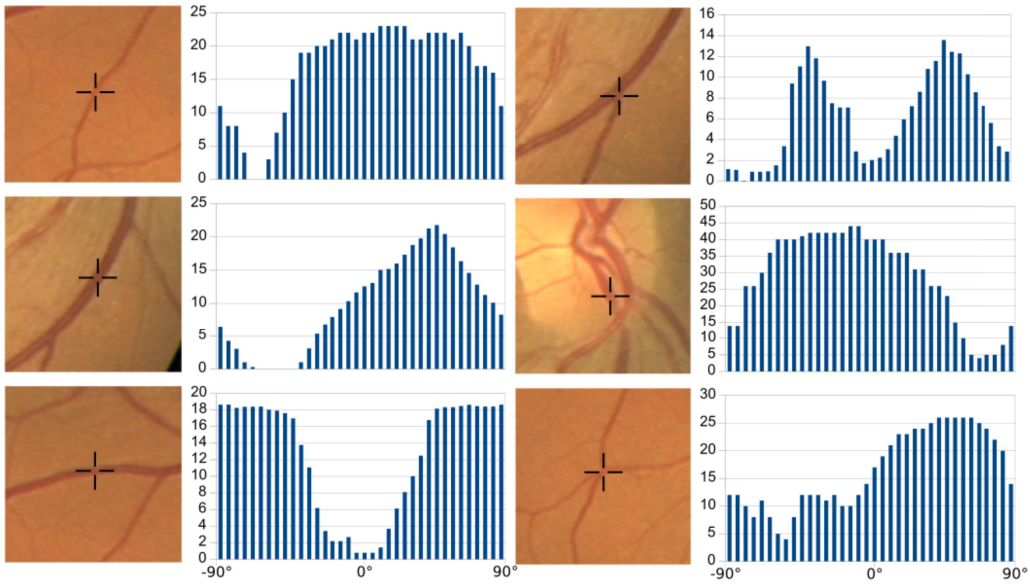

Figure 22. Six different Examples for the *DRV*s of different vessel structures.

segmentation, which is described in details later on.

In Fig. 22, six examples of *DRV*s of vessel segments and vessel crossings are shown. The horizontal and vertical axes of the diagrams indicate the orientation and the response value, respectively. It can be seen how the drops in the response values correspond to the orientation of the underlying structure, and that thicker vessels cause larger valleys in the *DRV*s.

4.1.3.1 Vessel score maps and extraction of seeds for region growing

In order to obtain a single value that describes the likelihood of a pixel belonging to a vessel, a score based on the statistical measures of its response vector is calculated. While most of the previously discussed similar directional methods only consider the maximal or summed response over the directions, here a more descriptive formula considering the mean, standard deviation and maximal value of the response vector is given [13]. The underlying idea of this approach is that vessel points have low or even zero response at directions matching the orientation of the corresponding vessel, thus, the variation of responses over the directions is higher. Therefore, we calculate the vessel score of a pixel by multiplying its response vector mean with the standard deviation and then divide the product with the maximal response value to achieve a certain level of normalization. That is, the vessel score is calculated as

$$score_{vessel}(DRV) = \mu_{DRV} \cdot \sigma_{DRV} / max_{DRV}\,, \tag{4.8}$$

where μ_{DRV}, σ_{DRV}, and max_{DRV} denote the mean, standard deviation, and maximum of a *DRV*, respectively. In Fig. 23 and 24, the maximum, mean, standard deviation and vessel score maps of the *BH*- and *MSMF-DRV*s of the retinal image from the image set DRIVE shown in Fig. 6 is given.

In order to correct the different ranges of the resulting score maps, statistical normalization is applied. That is, each score value *sc* is replaced with $(sc - \mu_{score})/\sigma_{score}$, where μ_{score} and σ_{score}, are the mean and standard deviations of the original score map. This normalization makes it possible to use the same score threshold th_{score} in the segmentation of the *MSMF* and *BH* maps.

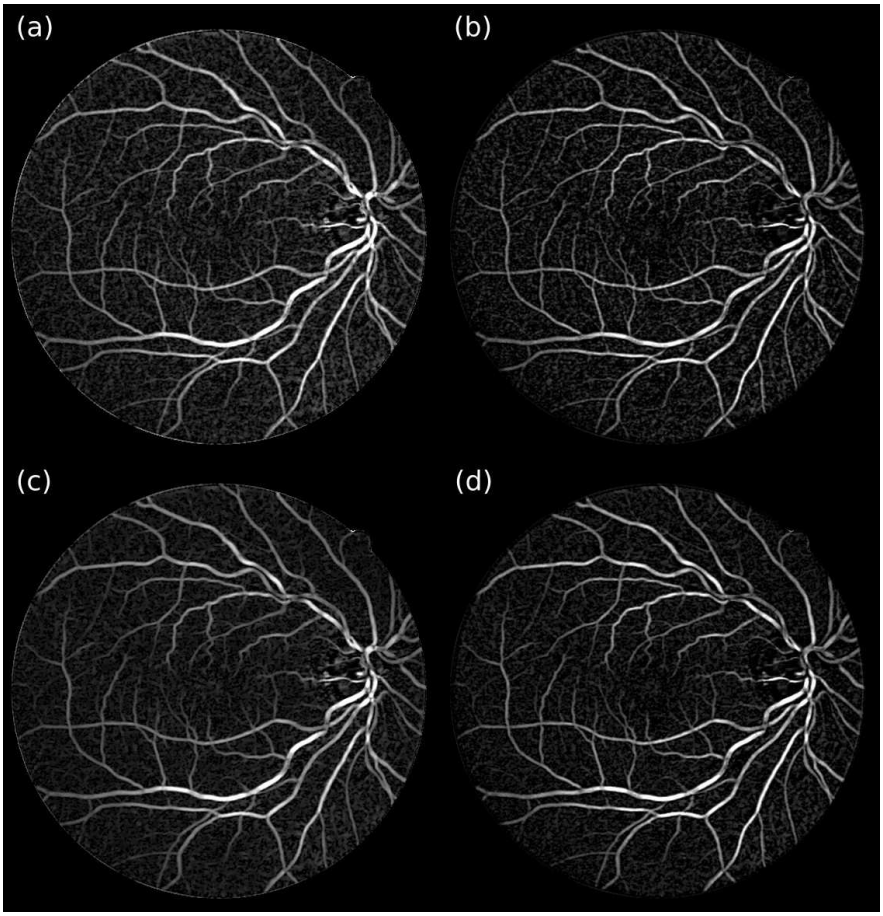

Figure 23. The *BH-DRV* maximum (a), mean (b), standard deviation (c), and final vessel score maps (d) of the retinal image shown in Fig. 6.

The segmentation procedure described in section 4.1.3.3 is a special region growing approach that uses both the response vector map and the corresponding vessel score map. The seed points of the procedure are those local maxima of the score map, whose values are greater than th_{score}. One advantage of this approach over, e.g, the simple thresholding of the score map to extract seed regions, is that this way the vessel seeds are located at the center of the vessels. This property gains importance, when seed points are classified based on their *DRV*s as described in the next section.

In order to extract the local maxima regions of the score map, the procedure described in Algorithm 1 was considered here as well. The only difference is that the score map first needs to be inverted so that maximal regions become

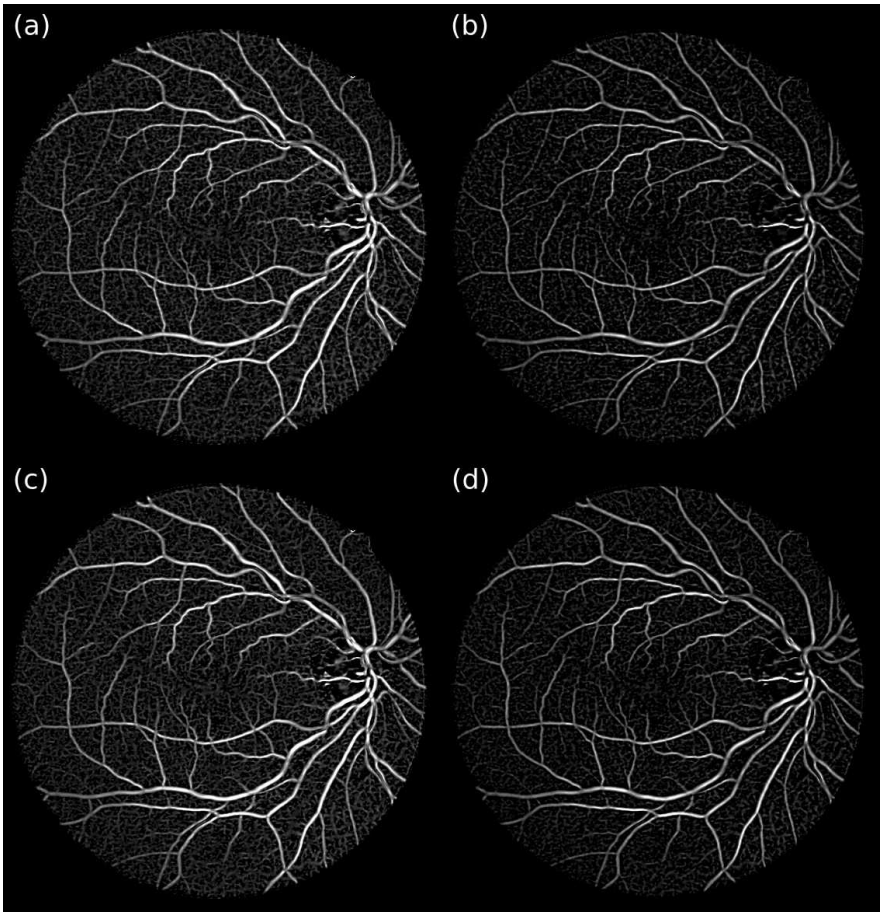

Figure 24. The *MSMF-DRV* maximum (a), mean (b), standard deviation (c), and final vessel score maps (d) of the retinal image shown in Fig. 6.

minimal ones.

4.1.3.2 Classification of the region growing seeds

The purpose of the classification step is to exclude seed points that clearly belong to lesions, such as MAs or haemorrhages. While it is less difficult to distinguish MAs, images with a high number of bright lesions close to each other are more challenging to deal with. For example, the background regions between certain bright lesions may be locally indistinguishable from vessels.

The *DRV* of a pixel provides information about its surroundings in the form of a fixed number of response values. This information is utilized in such a way that the seed points are filtered based on whether their *DRV*s are sufficiently

similar to that of a set of manually selected training points. The used technique is a nearest neighbor search, basically a one class kNN classification. However, instead of a Euclidean distance metric, a modified cross-correlation based measure is considered.

Each element of a *DRV* corresponds to a given direction, thus points of two identical structures that differ only in their orientation, e.g. two vessel segments of the same width, have different *DRV*s. To overcome this difficulty, a similarity measure of the *DRV*s that is invariant to the orientation of the underlying structure is proposed. This is accomplished by successively rotating (circularly shifting) either *DRV*, at each step calculating the normalized cross-correlation of the rotated *DRV* and the other one. The rotation is performed as many times as the length of the *DRV*. That is, finally all possible orientations are checked and the maximal correlation will give the similarity measure of the two vectors. Whether the rotation is to the left or the right is irrelevant, here the latter is considered, i.e., the rotation of a vector is performed by replacing each element of it with the one to the left, while the value shifted out at the last index is brought in at the first index.

To formulate this procedure, let X and Y denote two *DRV*s, and let l_A denote the length of *DRV A*. The maximal rotated cross-correlation (*MRCC*) is then calculated as

$$MRCC(X,Y) = max_{k=1,\ldots,l_X} \rho(R(X,k),Y), \tag{4.9}$$

where ρ denotes the Pearson correlation coefficient between the two *DRV*s, i.e.,

$$\rho(X,Y) = \sum_{i=1}^{l_A} \frac{(X[i]-\mu_X)\cdot(Y[i]-\mu_Y)}{\sigma_X \cdot \sigma_Y}, \tag{4.10}$$

and R denotes the rotation operation defined as

$$R(X,k)[i] = \begin{cases} R(X,k-1)[i-1], \text{if } i>0 \\ R(X,k-1)[l_X-1], \text{if } i=0 \end{cases}, \tag{4.11}$$

where $R(X,0) = R(X,l_X) = X$.

The classification of a *DRV* is done by comparing it to a given set of sample vessel point *DRV*s and recording the k highest *MRCC* whose mean value will

provide the confidence measure of the seed point. If this confidence is less than a predefined minimal value, then the corresponding seed point is omitted from the following region growing segmentation step. In the implementation, the minimal confidence was set to 0.95 and the value of *k* to 21.

The reason for considering a one class classification is that this way assembling the sample vectors is more straightforward, either by marking vessel points manually, or using the given binary masks of some publicly available image set. The only important requirement is that the marked points should be as close to the center of the vessel as possible, since the *DRV*s of vessel points are changing as getting closer to the edges. This can be easily accomplished by skeletonizing the binary vessel maps in available image sets. This is also the reason why the seeds were extracted in the way as described in the section 4.1.3.1, i.e, by considering the maxima of the corresponding vessel score map.

4.1.3.3 Region growing based segmentation using a directional response vector similarity constraint

The proposed region growing based segmentation operates by iteratively expanding a seed region through processing its contour points in a sequential manner, considering their non-region 8-neighbors as possible candidates. Such a candidate point is added to the region, if the product of its score divided by th_{score}, and the correlation coefficient between its *DRV* and that of the current contour point is higher than a predefined parameter *rg_coeff*. That is, a neighboring point *np* of a contour point *cp* is added to the region if

$$\rho\left(DRV_{cp}, DRV_{np}\right) \cdot \frac{score_{vessel}\left(DRV_{np}\right)}{th_{score}} \geq rg\_coeff \ . \tag{4.12}$$

The growing is continued until there are no more valid candidates to add. It is possible that a seed pixel is grown into another region, in which case it will not be processed individually, since the result would be the same. The pseudocode of the procedure is given in Algorithm 3.

Region growing criterion (4.12) expresses local similarity as the correlation of the *DRV*s of adjacent pixels, and allows certain level of deviation in vessel

Algorithm 3. The procedure of the region growing method used for segmentation.

Input:
- drvm: Directional response vector map.
- score_map: vessel score map.
- seeds: list of region growing seed points (maxima of the score map)
- score_th, rg_coeff: method parameters.

Output:
- label_map: result of the segmentation.

Auxiliary:
- point_queue: stores points for processing.

```
Fill label_map with 0.
label ← 0
for s in seeds do
   if score_map[s] >= th_score and label_map[s] = 0 then
      label ← label + 1
      push s to point_queue
      label_map[s] = label
      while |point_queue| > 0 do
         cp ← remove first item from point_queue
         for np in neighbors of cp do
            if label_map[np] = 0 then
               if corrCoeff(drvm[cp], drvm[np]) * score_map[np] / th_score >=
               rg_coeff then
                  label_map[np] ← seed_id
                  push np to point_queue
               endif
            endif
         endfor
      endwhile
   endif
endfor
```

score from th_{score} depending on the parameter *rg_coeff*. By letting the vessel score to be lower than th_{score}, technically, a double thresholding (hystersis thresholding) scenario is achieved. The only difference is that instead of using a secondary lower threshold expressed in the ratio of th_{score}, the degree of how much deviation is allowed depends on the similarity of the corresponding *DRV*s. That is, in case of adjacent pixels that show high correlation in their *DRV*s, a larger drop in vessel score is allowed. The aim of this approach is to prevent small non-vessel structures from being connected to the peripheries of vessels, which occasionally happens when using thresholding based solely on the vessel score. In order to demonstrate this effect, Fig. 25 shows portions of

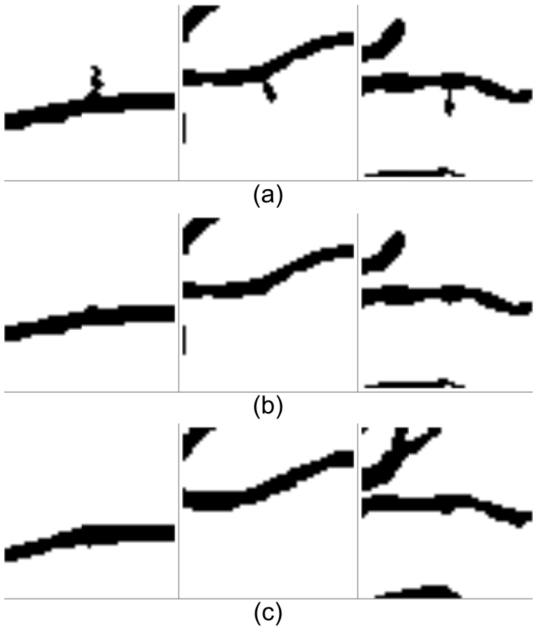

Figure 25. Examples showing the difference between simple double thresholding of the vessel score (a) and the proposed *DRV* correlation based region growing segmentation (b). The manual ground truth segmentations are also shown (c).

three example segmentations obtained by the proposed region growing method and the hysteresis thresholding of the respective vessel score maps, respectively. For the latter case, the high threshold was set to th_{score} and the low threshold to $rg\_coeff \cdot th_{score}$. This way, the two techniques can be compared. It can be seen that by using the proposed vector correlation based region growing method, artifacts that would be present otherwise are removed. While it is true that such cases are rather rare in an image, it is important to mention that such deformations would affect the results of other methods in a negative way. We can mention, e.g., skeletonization, as a common procedure to extract vessel network keypoints, such as branching points.

Another possible approach would be to compare the candidate pixels to the seed pixel using the *MRCC* of the *DRV*s as described in section 4.1.3.2. However, in practice, this approach leads to several problems and also deteriorates the performance. First, the *MRCC* has higher computational cost and this way all seed points have to be processed. This is because we cannot guarantee that even if a seed has been grown into the region of another seed

point, the result of growing from the first one would be the same. Hence, the processing time is largely increased. Moreover, as the region is getting larger, it is more probable that the structure of the vessel is getting more different, e.g., the width of the vessel is changing. An even more difficult problem is that when the growing reaches a point, where the vessel structure is substantially different, e.g., a vessel crossing or bifurcation, the growing would stop due to the entirely different *DRV*s.

4.1.4 Merging response vector map segmentations

As described in the beginning of section 4.1.3, the proposed segmentation is applied to both the *MSMF*- and *BH-DRVM*s resulting in two primary vessel segmentations, basically two sets of connected components obtained by region growing. In this final step, these two segmentations are merged to construct the final binary vessel mask.

The motivation of the merging step is that our experiments showed that large vessels are thinner on the *MSMF* segmentations than on the manually annotated ground truth images, while on the *BH* segmentation the width of these vessels are more appropriate. However, the *MSMF* is more sensitive to thin vessels, though it produces quite a lot of artifacts, too. The *BH* masks on the other hand are less susceptible for thin vessels, though usually some parts of them are present, even if the structure is not connected. Fortunately, *BH* masks are less sensitive to noise, thus, there are less artifacts on these segmentations.

First, we define the length of a binary connected component as the number of its non-intersecting skeleton points, i.e., those that have at most two 8-connected neighbors. In order to obtain the skeleton of a component, the corresponding method from the image processing library ImageJ [114] has been utilized. The method used to combine the two segmentations is the following.

Components on either segmentation whose length is higher than *high_length* are copied to the final vessel mask image. Considering the remaining components, those will belong to the final mask, whose intersection with at least one component from the other segmentation is not empty, and the length of the component chain is at least *low_length*. For this calculation, a temporary label map *T* is maintained, which is initially filled with zeroes. Whenever a

Algorithm 4. Procedure for merging the components of the *MSMF* and *BH* segmentations.

Input:

- *COMPS:* components of the two segmentations to be combined, denoted as *COMPS*[0] and *COMPS*[1].
- *low_length*, *high_length*: low and high length thresholds.

Output:

- *vessel_map:* binary result of the combination.

Auxiliary:

- *T:* temporary label map.

```
Fill T and vessel_map with 0.
temp_label ← 0
for k in {0,1} do
   for c in COMPS[k] do
      if length of c >= high_length then
         Copy c to vessel_map with value 1.
      else
         L ← set of non zero labels in T under c
         if |L| > 0 then
            Copy c to T with first label from L.
            if |L| > 1 then Record label equivalences.
         else
            C2 ← components in COMPS[1 – k] overlapping with c
            if |C2| > 0 then
               temp_label ← temp_label + 1
               Copy c and C2 to T with temp_label.
            endif
         endif
      endif
   endfor
endfor
Resolve label equivalences in T.
for c in components of T do
   if length of c >= low_length then Copy c to vessel_map with value 1.
endfor
```

component from either segmentation is processed, first it is checked whether it overlaps with a non-zero label from *T*. If so, the points of the processed component are set to this value on *T*, i.e., the union of the two sets is constructed. If there were multiple non-zero labels, then the label equivalences are stored using a convenient data structure and the component is copied to *T* with one of the labels. Otherwise, if all values were zero, then it is checked whether there are overlapping components from the other segmentation, and if so, their union with a new label is copied to *T*. Finally, when components of both segmentations are processed, the components of *T* are tested for their

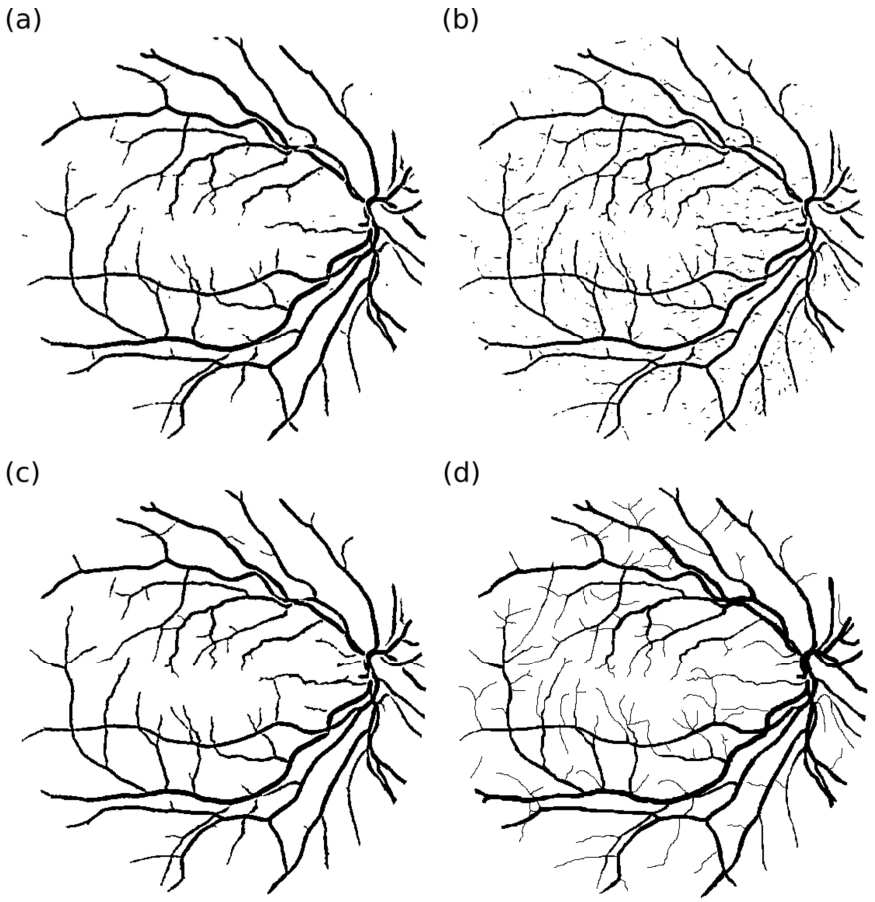

Figure 26. Binary results of the region growing on the *MSMF* (a) and *BH* (b) *DRVM*s, the result of their merging (c), and the manual ground truth vessel segmentation of the same retinal image (d).

length, with also taking the label equivalences into consideration. Those components that pass are copied to the final vessel map in a binary form. The pseudocode of the merging procedure is enclosed in Algorithm 4.

Resulting from the presented merging of the *MSMF* and *BH* components, those small components that are only present on either segmentation are removed. This becomes useful in the case of the *MSMF* segmentation as discussed before. *MSMF* is more sensitive for thin vessels, yet some fragments are usually present on the *BH* too. Thus, the combination of the two makes a fair compromise. Also, the width of large vessels is mostly corrected in this way, simply because the *BH* is the more prominent in such case. In Fig. 26,

binary examples of the *MSMF* and the *BH* segmentations of the retinal image in Fig. 6, along with the result of their merging and the ground truth manual vessel segmentation are shown. The vessel score threshold was 0.5 in this case, and the *rg_coeff* parameter was set to 0.6.

4.2 Experimental evaluation of the proposed retinal vessel segmentation method

4.2.1 Materials and parameters

The performance of the proposed vessel segmentation method has been tested on two publicly available image sets. The image set DRIVE [95] consists of 40 color retinal images with an FOV of 45°. The spatial resolution of the images is 565×584 pixels, and the diameter of the ROI is approximately 540 pixels on each image. The image set is equally divided into a training and a test set. The binary ROI masks are also given for every image. The manual segmentations of the vascular system are given for both the training and test images, and secondary manual segmentations by a different observer are given for the test images as well.

The STARE database [69] consists of 20 color retinal images with a spatial resolution of 700×605 pixels, and an FOV of 35°. Two manual vessel segmentations are available for each image, and the binary ROI masks are also given. The ROI diameter of these images is approximately 650 pixels on average.

The High-Resolution Fundus (HRF) Image Database [88] consists of 15 healthy images, 15 ones with diabetic retinopathy, and 15 more with glaucoma. The spatial resolution of the images is 3504×2336 pixels. One manual vessel segmentation is available for each image and the ROI masks are also provided. The diameter of the ROI of the images is approximately 1015 pixels.

The parameter values of the proposed method given so far correspond to the ROI diameter of the DRIVE images. Images of different spatial resolution should be either rescaled or the parameter values should be altered accordingly. The parameters that are resolution sensitive are the maximal vessel width as used in the bottom-hat response calculation, which was set to 9 for the DRIVE images, and the values of the parameters *low_length* and *high_length* were set to 15 and 25, respectively. The value of *rg_coeff* was experimentally set to 0.6. The sample *DRV*s for the classification step were obtained by manually marking 218 vessel points on two of the DRIVE training images. The minimal

confidence and the parameter k for the seed point classification described in section 4.1.3.2 were set to 0.95 and 21, respectively. These values were also established by manual experimentation. Probably more optimal parameter configuration could be found by exhaustive testing, however, in this work the aim was to focus on the algorithm itself rather than its optimization.

4.2.2 Results

The result of the proposed method on the DRIVE test images is shown in Table 4, along with the results of several state-of-the-art methods, all discussed earlier in section 2.2. The score threshold th_{score} was experimentally set to the level, where the *FPR* figure was the closest to the second manual segmentation. Moreover, the *FPR* of most other methods also come from this range. It can be observed that the difference in *TPR* between the proposed method and the second manual segmentation is only 0.0117 at the same *FPR*. Similarly, the results on the STARE images are shown in Table 5. The score threshold th_{score} here was set to the level, where the *FPR* is the closest to that of the other

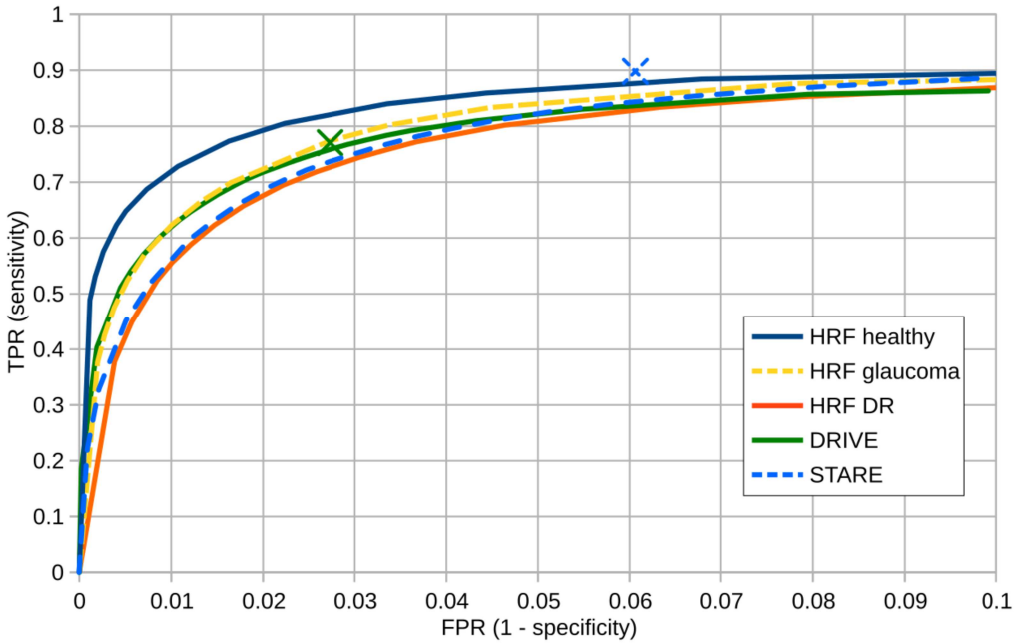

Figure 27. ROC curves of the proposed method obtained on the test images of the DRIVE, and STARE datasets, respectively. Crosses mark the accuracy of the second manual segmentations on the respective datasets.

Table 4. Performance of the proposed method on the test images of the dataset DRIVE compared with the state-of-the-art.

Method	***FPR***	***TPR***	***ACC***	***AUC***
2nd human observer	0.0277	0.7763	0.9470	-
Proposed method	0.0277	0.7646	0.9458	0.9351
Martinez-Perez et al. [89]	0.0345	0.7246	0.9344	-
Staal et al. [95]	0.017	0.6780	0.9441	0.9520
Marín et al. [65]	0.0199	0.7067	0.9452	0.9588
You et al. [81]	0.0249	0.7410	0.9434	-
Zhang et al. [74]	0.0276	0.7120	0.9382	-
Mendonca and Campilho [72]	0.0236	0.7344	0.9452	-
Fraz et al. [76]	0.0231	0.7152	0.9430	-
Fraz et al. [63]	0.0193	0.7406	0.9480	0.9747
Miri and Mahloojifar [97]	0.0205	0.7352	0.9458	-
Vlachos and Dermatas [96]	0.045	0.747	0.929	-
Bankhead et al. [101]	0.0283	0.7027	0.9371	-
Qian etl al.[85]	0.0211	0.7187	0.9509	-
Yu et al. [94]	0.0255	0.7233	0.9426	-
Al-Diri et al. [79]	0.0449	0.7282	-	-
Nguyen et al. [83]	-	-	0.9407	-
Ricci and Perfetti [80]	-	-	0.9595	0.9633
Soares et al. [103]	-	-	0.9466	0.9614
Lupascu et al. [66]	-	-	0.9597	0.9561
Lam et al. [67]	-	-	0.9472	0.9614
Wang et al. [84]	-	-	0.9461	-

methods, the *TPR* of the proposed method at the *FPR* of the second manual segmentation on these images is approximately 0.85. There are no secondary manual segmentations for the HRF database. The respective *ROC* curves of the proposed method are shown in Fig. 27. Table 6 shows the *TPR* and *FPR* results at the highest accuracies of the proposed method in comparison with other state-of-the-art ones on the HRF images.

The focus during development was on the performance at low *FPR*s.

Table 5. Performance of the proposed method on the dataset STARE compared with the state-of-the-art.

Method	***FPR***	***TPR***	***ACC***	***AUC***
2nd human observer	0.061	0.9017	0.9351	-
Proposed method	0.0249	0.7248	0.9492	0.9360
Martinez-Perez et al. [89]	0.0431	0.7506	0.9410	-
Staal et al. [95]	0.019	0.6970	0.9541	0.9614
Marín et al. [65]	0.018	0.6944	0.9526	0.9769
You et al. [81]	0.0244	0.7260	0.9497	-
Zhang et al. [74]	0.0247	0.7177	0.9484	-
Mendonca and Campilho [72]	0.027	0.6996	0.9440	-
Qian et al. [85]	0.0233	0.7187	0.9509	-
Yu et al. [94]	0.0291	0.7112	0.9463	-
Odstrcilik et al. [88]	0.0488	0.7847	0.9341	-
Annunziata et al. [92]	0.0164	0.7128	0.9562	-
Fraz et al. [76]	0.0319	0.7311	0.9442	-
Fraz et al. [63]	0.0237	0.7548	0.9534	0.9768
Al-Diri et al. [79]	0.0319	0.07521	-	-
Nguyen et al. [83]	-	-	0.9324	
Ricci and Perfetti [80]	-	-	0.9680	0.9646
Soares et al. [103]	-	-	0.9671	0.9480
Lam et al. [67]	-	-	0.9567	0.9739
Wang et al. [84]	-	-	0.9521	-

However, since some literature methods only discuss the performance in terms of *AUC*, the *AUC* values of the proposed method were also calculated, and are enclosed in Tables 4 and 5. The results of the literature methods are borrowed from the cited papers, the algorithms were not reimplemented. The performance of the proposed method is slightly weaker on the STARE images, compared to the accuracy of the second manual segmentation. This is mostly because there are more pathological images in this set, and some are of significantly worse quality than the DRIVE images. It is also important to mention that the same training *DRV*s are used in the classification that were obtained on the training

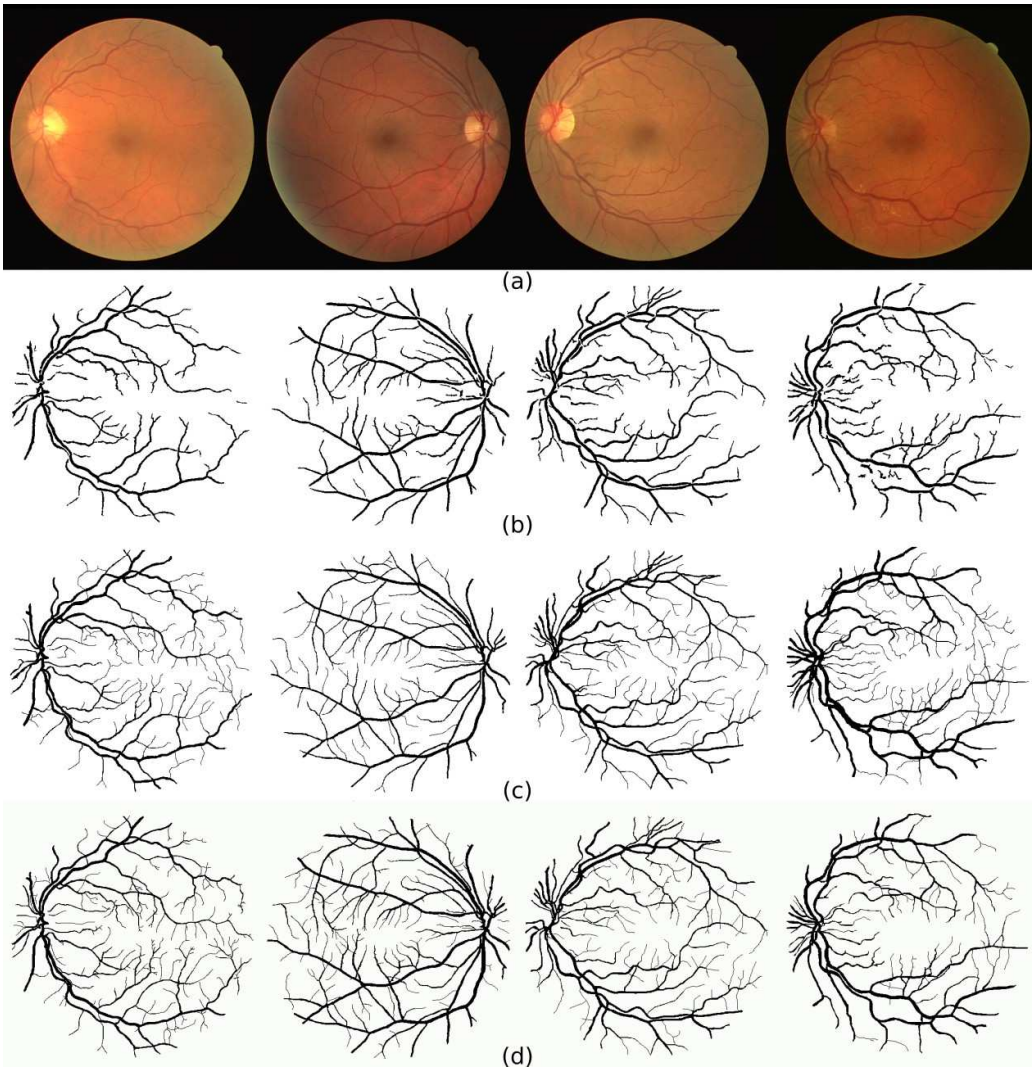

Figure 28. Images from the image set DRIVE (a). The results of the proposed method at threshold 0.6 (b), the ground truth segmentations (c), and the second manual segmentations (d).

images of the dataset DRIVE.

Fig. 28 and 29 show four images from the image set DRIVE and four from the image set STARE, respectively, along with the results of the proposed vessel segmentation method and the two manual segmentations. The score threshold of the proposed method was set to 0.6 in both cases. Similarly, Fig. 30 shows three images from the database HRF. It is important to point out the lack of falsely detected optic disc boundaries, due to the previously discussed *MSMF* and *BH*

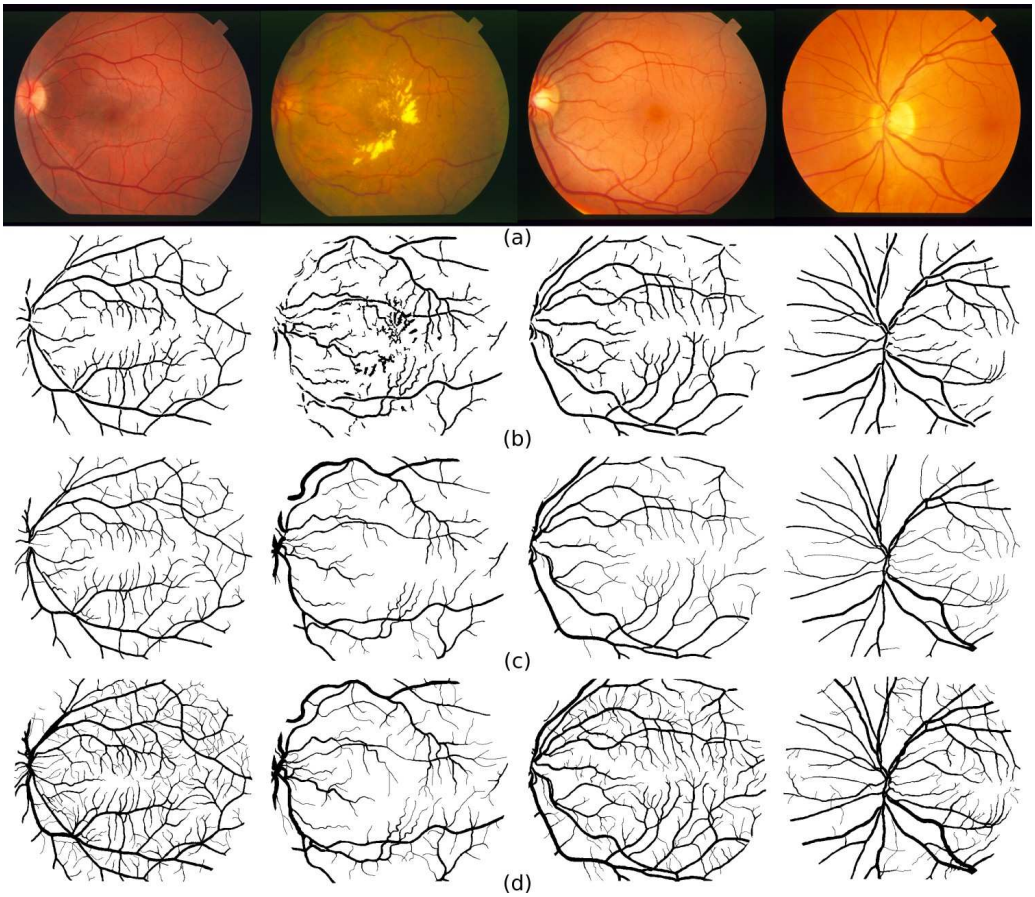

Figure 29. Images from the image set STARE (a). The results of the proposed method at threshold 0.6 (b), the ground truth segmentations (c), and the second manual segmentations (d).

filters. It can be seen that the proposed method performs well on most images, even if the contrast is low. However, the presence of bright lesions does cause some misclassification. While the border of bright lesions do not yield the ringing effect for the same reason as in the case of the optic disc boundary, the regions between closely located exudates unfortunately give some false positives.

Overall, it can be stated that the experiments proved that the proposed method is comparable in accuracy with the state-of-the-art, and in many cases it performs even better than literature methods. Since the components of the proposed vessel segmentation method are novel in the field of retinal image processing, it is a rational assumption that the segmentation results should also

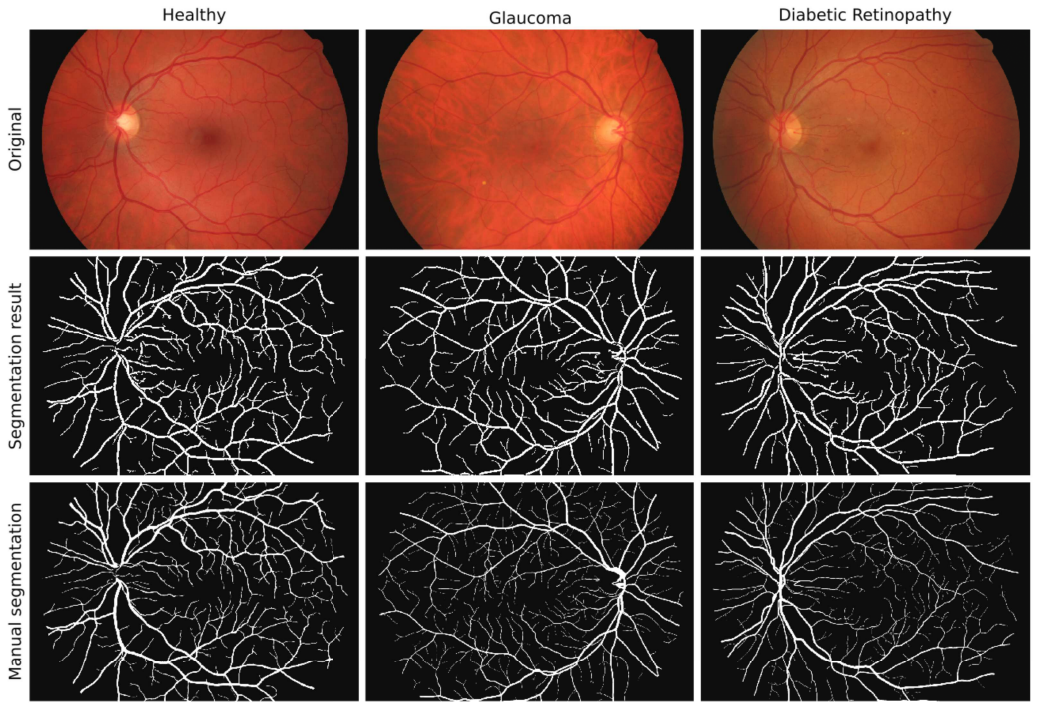

Figure 30. Three images from the database HRF with the segmentation result of the proposed method and the ground truth manual segmentations.

differ from that of other methods in certain cases. Any CAD system has to consider as much methods as possible in order to improve the final outcome, and heterogeneity among the basic principles of the components of such ensemble system is a favorable property.

The execution time in the case of the DRIVE images was around 30 seconds

Table 6. Performance of the proposed method on the dataset HRF compared with the state-of-the-art.

	Healthy			**Glaucoma**			**Diabetic Retinopathy**		
Method	*FPR*	*TPR*	*ACC*	*FPR*	*TPR*	*ACC*	*FPR*	*TPR*	*ACC*
Proposed method	0.0163	0.7736	0.9572	0.0165	0.6993	0.9539	0.0178	0.6577	0.9488
Yu et al. [94]	0.0233	0.7938	0.9566	0.0338	0.789	0.9518	0.0375	0.7604	0.946
Odstrcilik et al. [88]	0.025	0.7861	0.9539	0.0362	0.79	0.9497	0.0381	0.7463	0.9445
Annunziata et al. [92]	0.0065	0.6820	0.9587	0.0215	0.7566	0.9603	0.0213	0.6997	0.9554

Table 7. Average execution times of the proposed and literature vessel segmentation methods in the case of the DRIVE images.

Method	Year	Execution time
Proposed method	2015	30 sec
Martinez-Perez et al. [89]	2007	NA
Staal et al. [95]	2004	15 min
Marín et al. [65]	2011	1.5 min
You et al. [81]	2011	NA
Zhang et al. [74]	2010	10 sec
Mendonca and Campilho [72]	2006	2.5 min
Miri and Mahloojifar [97]	2011	50 sec
Vlachos and Dermatas [96]	2010	NA
Qian etl al. [85]	2014	2 min
Al-Diri et al. [79]	2009	11 min
Nguyen et al. [83]	2013	2.5 sec
Ricci and Perfetti [80]	2007	NA
Soares et al. [103]	2006	3 min
Lupascu et al. [66]	2010	2 min
Lam et al. [67]	2010	13 min
Wang et al. [84]	2013	3.5 min

on average, and 40 seconds in the case of the STARE images. The proposed method was implemented in JAVA SE 1.6, and tested on a laptop equipped with Intel(R) Core(TM) i3 M350 CPU and 3 GBs of RAM. The calculations of the *DRVM*s and the seed point classification have been parallelized, since these are the most time consuming parts. The *DRV* calculation of the individual pixels can be done independently from each other. Similarly, the region growing seeds can be classified independently. The time demand of the proposed classification step depends on the number of the used training *DRV*s, i.e., the number of sample vectors. There is no explicit training of the classifier, the setup only involves the loading of the sample vessel *DRV*s. The region growing segmentation by itself took around 2 seconds in the case of the DRIVE images. Table 7 lists the average execution times of the discussed state-of-the-art vessel

segmentation methods on the DRIVE images. The reported times do not include the occasional classifier training times. The data have been borrowed from the cited papers, and many of them could now be considered outdated. Probably all the listed methods could be implemented more efficiently, and ran on faster or more appropriate hardware. This table only aims to give a rough representation of the computational time demands of the different approaches.

4.3 Applications in digital dermatoscopic image analysis

Certain components of the presented vessel segmentation technique has been also applied successfully in another field of medical image processing, namely, the automatic analysis of digital dermatoscopic (epiluminescence microscopy, ELM) images. Next, a brief insight into the background of dermatoscopy and its importance in the diagnosis of melanoma is given.

4.3.1 Dermatoscopy and the role of pigment networks in melanoma diagnosis

Dermatoscopy is the primary diagnostic technique for examining skin lesions, and thus distinguishing benign cases from cancerous ones. There are many variants of dermatoscopes. Traditional ones consist of a magnifier, a non-polarized light source, and a transparent contact plate. These models require the usage of immersion liquid before directly placing the tool on the skin, thus flattening its surface. A serious disadvantage of this technique is the presence of air bubbles stuck in the immersion liquid, appearing with very bright edges due to the strong lighting. Another widespread line of dermatoscopes are those that use polarized light source, this way canceling skin reflections. These models do not require the usage of immersion liquid, and by controlling the degree of polarization, both surface and subsurface (dermatoscopic) inspections are attainable. If the dermatoscope is attached to a digital camera, either through an adapter or directly, it is referred to as a digital or video dermatoscope.

Among the many features of a skin lesion that a dermatologist must consider, the type of the pigment network, if present, is of prominent importance. The pigment network is a grid-like network consisting of pigmented lines and hypopigmented holes [115]. The assessment of pigment network alterations is helpful for differentiating between benign and malignant melanocytic proliferations, especially when they are confined to the epidermis and superficial dermis [116]. Typical (regular) pigment networks are relatively uniform, regularly meshed, homogenous in color and usually thinning out at the peripheries. An atypical (irregular) pigment network is of darker color, its lines often thickened, the mesh irregular with holes that are heterogeneous in

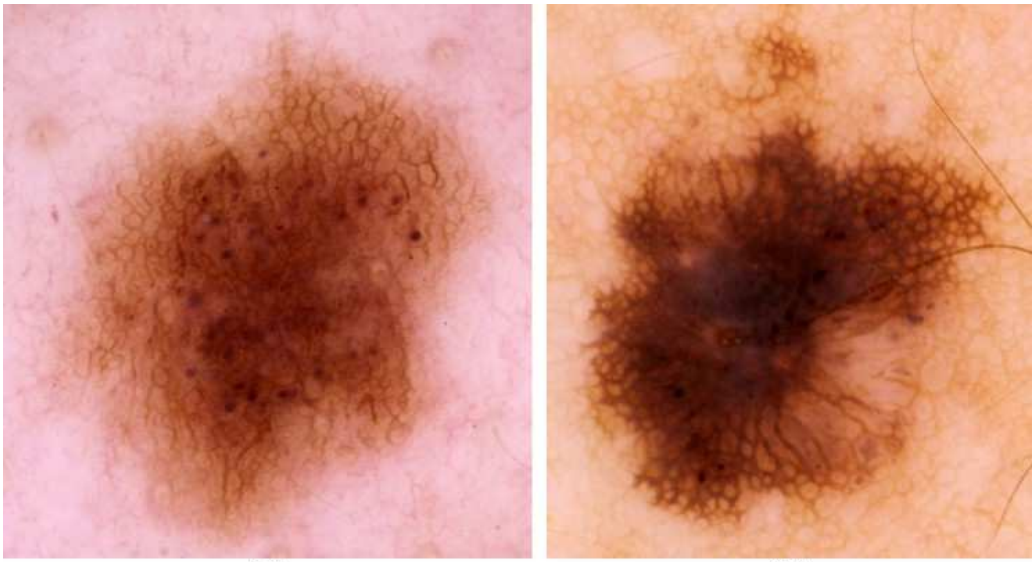

Figure 31. Examples for regular (a) and irregular (b) pigment networks in dermatoscopic images of melanocytic skin lesions.

area and shape, and it usually ends abruptly at the peripheries. Most importantly, an atypical pigment network is a dermoscopic criterion with high specificity for the diagnosis of melanoma [115], [116]. In Fig. 31, two example images are shown both for typical and atypical pigment networks in dermatoscopic images.

There are several similarities between retinal vessel and dermatoscopic pigment network segmentation regarding the approaches considered in the literature. Some of the latest methods include those by Sadeghi et al. [117], Barata et al. [118], and Arroyo et al. [119]. While naturally the literature on automatic pigment network detection is more extensive than what is discussed in this dissertation, the operation of these recent methods give a good insight into the field. In [117], LoG filtering is applied to capture all intensity transitions, and subsequently, the closed contours of the zero crossings are considered in order to extract holes of the network. The holes are then transformed to a graph using a maximal distance threshold. The LoG filtering results in the detection of both bright and dark transitions, and contour cycles that correspond to dots, globules (another form or pigmentation), or bubbles are removed using previously learned parameters. The method proposed in [118]

considers a directional approach using rotated difference of Gaussian (DoG) filters, and taking the maximal response over the directions, similarly to the vessel segmentation methods discussed earlier in section 2.2. Following the steps of reflection and hair removal, which is also based on the directional DoG filtering, the network is extracted by thresholding the filtered image. The classification of the lesion is then performed by determining several topology related features based on the relations of the network and its holes. The approach in [119] considers many pixel level features, such as Gaussian filter responses of different scales, Hessian features, DoG filters, and statistical texture features, in this case the variance and entropy of gray level co-occurance matrices. The segmentation is carried out by pixel level classification and the decision on the presence of the network is again mostly based on analyzing the network holes.

From this overview, it can be seen that the techniques used for the tasks of retinal vessel segmentation and dermatoscopic pigment network detection are indeed very similar. Consequently, it seems reasonable to assume that some parts of the vessel segmentation method proposed earlier may be successfully applied to this task as well.

4.3.2 A novel pigment network detection technique

Since there is no such maximal thickness criteria for pigment networks as for retinal vessels, and the scale of magnification is not constant among images, the grayscale morphology based directional response calculation (section 3.2.1) is not a valid approach here. However, due to its advantageous properties, the multiscale symmetric matched filtering (*MSMF*) approach (section 4.1.2.1) can be also utilized to extract the lines of the network. Its multiscale nature can handle lines of varying thickness, and the symmetry constraint ensures that the edges of bright structures and light reflections will not be falsely detected.

The procedure is the same as described in secion 4.1.2.1 with the exception that it is applied on an intensity image calculated from the red, green, and blue channels, instead of considering only the green channel as in the case of retinal images. The grayscale intensity is determined by:

$$I_{GS} = 0.299 \cdot I_R + 0.587 \cdot I_G + 0.114 \cdot I_B \tag{4.13}$$

where I_R, I_G, and I_B are the red, green, and blue intensity channels, respectively. The network score of each pixel, is calculated using the vessel score formula described in equation (4.8).

To obtain a binary network mask, a hysteresis thresholding technique is applied to the score map. This means that two threshold values are considered, a high (th_{high}) and a low (th_{low}) one, and those pixels are marked as foreground ones, whose score is greater than th_{low} , and are connected to at least one point with a score greater than th_{high} through an 8-connected path of points with scores greater than th_{low} . The high threshold was set as the mean score, and $th_{low} = 0.5 \cdot th_{high}$. The response vector similarity based region growing segmentation (section 4.1.3.3) has been also tested, and though it was able to eliminate some deformations, there was no significant difference regarding the final decision on the presence of the pigment network.

The recognition of the pigment network is based on analyzing the holes of the binary network mask, i.e., those 4-connected components of background pixels that do not touch the image borders. Since the network segmentation is not perfect, several such holes will be detected even in images that do not contain pigment network. Consequently, the holes need to be filtered. First, holes consisting of less than 5 or more than 400 pixels are automatically rejected. For the remaining holes, a simple convexity measure, the ratio of the area of the hole, and the area of its convex hull is calculated. This measure is known as the solidity, and those hole components are kept, whose solidity is at least 0.8.

The remaining holes are decomposed into disjoint groups, based on proximity analysis using a simple maximal distance clustering. In each such group, every hole must be within this maximal distance to at least another hole component. The group is considered to correspond to a pigment network if it is composed of at least four hole components. The number of holes in groups that fulfilled this criteria are summed up, and if this number exceeds a certain threshold, then the lesion is considered to contain a pigment network. This threshold was set to 50 in our test implementation. Fig. 32 shows a skin lesion with typical pigment network, the generated pigment network score map, the prefiltered holes in the segmented pigment network, and the groups resulting

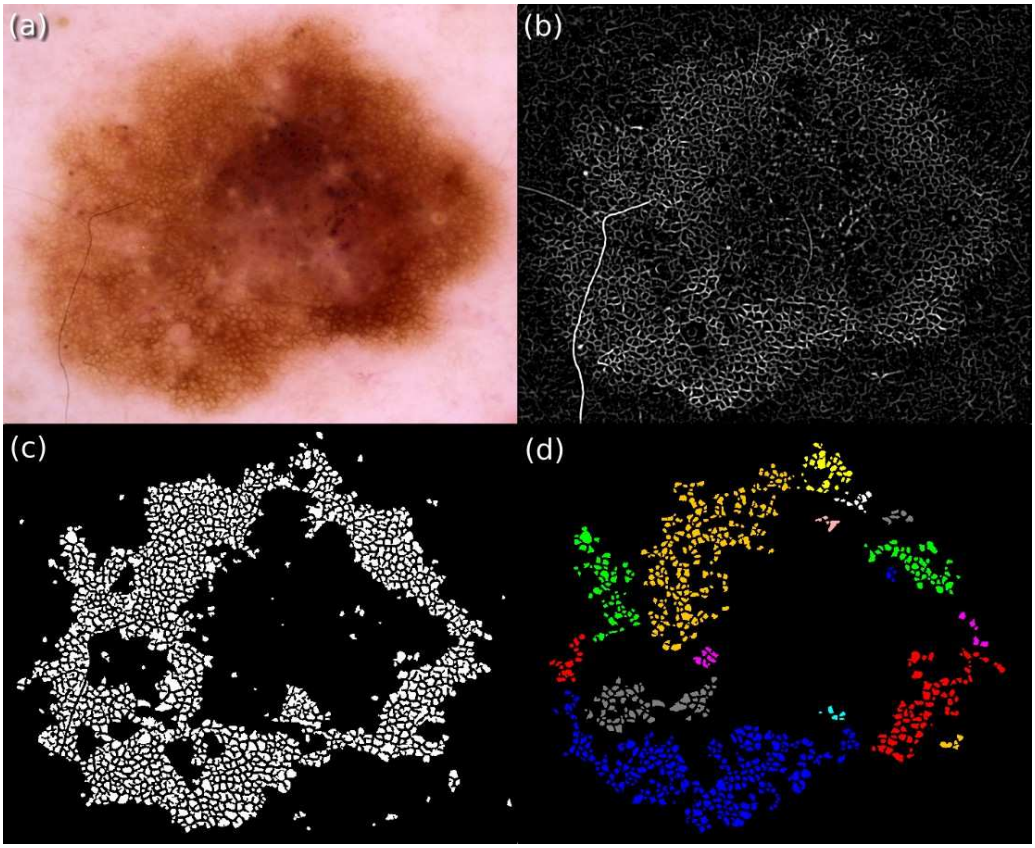

Figure 32. A sample dermatoscopic image (a), the calculated network score map (contrast enhanced for better visualization) (b), the holes of the segmented network (c), and the result of the maximal distance clustering of the filtered hole components (d).

after the maximal distance clustering of the holes that passed the solidity test.

Though the proposed procedure is fairly simple compared with other state-of-the-art methods, it is not in the scope of this work to give a thorough and well-optimized method for dermatoscopic pigment network detection, rather to show that the proposed matched filtering and score calculation can also be used for this task, and hopefully in the future it may be a key component in a more elaborate system.

4.3.3 Preliminary results on the recognition of the presence of pigment network

Unfortunately, there are no publicly available annotated dermatosopic image sets dedicated to automatic pigment network recognition and typicality

measurement testing. One way is to manually collect images from a dermatoscopy atlas, such as [116]. However these images are usually of poor spatial resolution and often corrupted by the presence of air bubbles, light reflections, and hair. Available literature methods are mostly tested on private image sets.

Resulting from our collaboration with the Department of Dermatology of the University of Debrecen, a set of high-resolution dermatoscopic images have been collected [120]. For this experiment 21 images have been selected, of which there are 8 images with no pigment network, 6 with typical pigment network, and 7 with atypical pigment network. The original resolution of the images vary between 15 and 18 megapixels. All images were rescaled to a width and height that is 20% of the original, and the lesion regions have been manually cropped before the steps of the segmentation.

Among the 8 negative images, 7 were correctly identified, and 1 was falsely marked as containing pigment network. Similarly, among the 13 positive images, 12 were correctly identified, and 1 was missed. That is, in this experiment, sensitivity and specificity were 92.3% and 87.5%, respectively. Though this experiment was conducted on a small dataset, these results prove that the technique proposed for retinal vessel segmentation can be also successfully applied to segment the pigment network in dermatoscopic images.

4.4 New scientific results in the field of retinal vessel segmentation

1. A multiscale matched filtering procedure based on the second derivative of the Gaussian filter has been proposed. The novelty of this technique is that it does not give false high responses at the boundary of the optic disc and bright lesions, which is a common drawback in many matched filtering or other line strength measure based vessel segmentation methods. The solution proposed here overcomes this issue by implementing a symmetry constraint in the response calculation. This technique allows high response only for those cross-sections, where the difference in the degree of the intensity transition of the two sides is minimal. Related publication: [14].
2. A novel vessel segmentation technique has been proposed, whose most important property is that it utilizes all directional responses of a pixel, and not just a dedicated value such as the maximum or sum as in most similar literature techniques. A similarity measure based on the correlation of directional response vectors has been given, which is invariant to the orientation of the structures to which the respective pixels belong. It has been shown how this measure can be applied in the nearest neighbor classification of region growing seed points. The specialty of the proposed region growing segmentation procedure is that it considers both the vessel score difference and the directional response vector similarity of adjacent pixels. The construction of the vessel score of a pixel is also a contribution of this dissertation, and it assigns higher value to elongated structures than small circular ones by utilizing that the variation in the directional responses of such points is higher. Related publications: [13], [14].

5 SUMMARY

This dissertation presents novel image processing techniques for the automatic analysis of fundus images. Two automatic methods for microaneurysm detection, and an automatic vessel segmentation method have been proposed. It has also been demonstrated how the proposed vessel segmentation technique may be used to extract the pigment network in dermatoscopic images.

Microaneurysms (MAs) are the first signs of diabetic retinopathy. Thus, their recognition is a primary task in any automated screening system that aims to assist the diagnosis of this disease. The first contribution of this work is that it is shown how a well-known directional morphology technique can be used to construct an unsupervised MA detection method. This procedure is nearly parameter-free, except for the maximal MA diameter, and it gives a novel approach to the utilization of directional responses. The second proposed MA detection method applies a similar directional approach as existing MA detectors in the literature. However, such direct analysis of image minima cross-section profiles has not been discussed before. The described peak detection technique, the proposed peak descriptors, the feature set, and the formula to calculate the final score are all novel contributions of this dissertation to the field of computer assisted retinal image analysis. The performance of the proposed MA detection methods has been evaluated both in an online competition and on an independent image set provided by an eye clinic, where grading of retinal images is done on a daily routine. The proposed cross-section profile analysis based detector proved to be the best non-ensemble method in the competition and achieved the highest sensitivity at low false positive rates among all participants. The only method that has achieved higher average sensitivity was an ensembe-based detector, which combines several individual algorithms, including the unsupervised morphological method presented in this work.

Vessel segmentation may have many roles in automatic retinal image processing, such as an aid to lesion detectors, anatomical parts localization, as the basis of image registration, or even for authorization purposes. While it does

not form the first line of diagnosing diabetic retinopathy, in later stages it may be useful to recognize vessel deformations or the symptoms of hypertension. The vessel segmentation method presented in this dissertation also follows a pixel-wise directional approach. However, due to different expectations towards vessel segmentation, it considers an entirely different workflow as that of the proposed MA detection method. The proposed multiscale matched filtering technique overcomes the problem of steep intensity transitions that occur at the boundary of the optic disc and bright lesions. Unlike most similar directional methods in the literature, which only consider the maximal response over the directions, the vessel score formula presented here is less sensitive to noise and results in higher score for elongated structures than for circular ones like microaneurysms. The proposed utilization of directional responses is what distinguishes the most the proposed method from the state-of-the-art. The proposed correlation based similarity measure for directional response vectors and classifier setup have not been applied in the field of retinal image analysis before, and presumably along with the presented region growing scheme could be used in other fields of digital image processing as well.

It has also been demonstrated that certain components of the proposed vessel segmentation technique, namely the multiscale symmetric matched filtering and the vessel score formula, can be applied for the segmentation of the pigment network in dermatocopic images. Using a simple spatial clustering technique on the obtained network holes it was made possible to estimate whether the lesion contains a pigment network or not.

6 ÖSSZEFOGLALÁS (SUMMARY IN HUNGARIAN)

Ebben az értekezésben szemfenék-képek automatikus elemzéséhez használható új digitális képfeldolgozási módszerek kerültek bemutatásra. A dolgozat első felében két új automatikus mikroaneurizma detektort, a másodikban pedig egy új érhálózat szegmentáló algoritmust adtunk meg. Megmutattuk továbbá, hogy a retina érhálózatát szegmentáló eljárás bizonyos komponensei eredményesen használhatóak dermatoszkópos eljárással bőr léziókról készült felvételeken történő pigment-hálózat szegmentálási feladatokra is.

A mikroaneurizmák megjelenése a szemfenéken a diabéteszes retinopátia legelső látható tünete, így ezek felismerése elsődleges fontosságú bármilyen olyan automatikus döntéstámogató rendszerben, mely ennek a betegségnek a hatékony szűrését hivatott segíteni. Az értekezés első eredménye ezen a téren annak az igazolása, hogy egy, a területen alapvető morfológiai eljárásból kiindulva készíthető egy betanítást nem igénylő, lényegében paraméter nélküli mikroaneurizma detektor. A másodjára bemutatott aneurizma detektorhoz hasonló irány-szerinti eljárásokon alapuló módszerek ugyan léteznek már az irodalomban, azonban a keresztmetszeti intenzitás profiloknak az itt javasolt alkalmazása még nem került máshol tárgyalásra. A leírt csúcsdetektálási módszer, a javasolt csúcsleírók, a jellemző vektorok, illetve a végső pontszámítási formula mind saját fejlesztés eredménye és ezen disszertáció hozzájárulása a számítógéppel támogatott szemfenék-kép kiértékelés területéhez. A bemutatott eljárások teljesítménye egy nyílt nemzetközi versenyben, illetve egy független szemészeti intézménytől származó képi halmazon került kiértékelésre. A dolgozatban bemutatott keresztmetszeti intenzitás profilokon alapuló módszer bizonyult a legjobb egyedi algoritmusnak az említett online versenyben és szolgáltatta az összes résztvevő módszer közül a legmagasabb szenzitivitást alacsony fals pozitív szám mellett. Az egyetlen összesítésben jobb pontosságot nyújtó módszer egy olyan összetett rendszer volt, mely több egyedi algoritmus kimenetét kombinálja, beleértve a dolgozatban elsőként bemutatott osztályozó lépés nélküli detektorét is.

Az érhálózat szegmentálásának több alkalmazása is lehet a retina-képek

automatikus feldolgozása során, ilyenek például az elváltozások detektálásának támogatása, anatómiai részek helyzetének pontosabb meghatározása, különböző modalitású képek regisztrációja, vagy biometrikus azonosítási eljárások megalapozása. Bár nem tartozik a diabéteszes retinopátia diagnózisának első vonalába, az eljárás a betegség későbbi stádiumában felhasználható az érhálózat elváltozásainak felismeréséhez vagy éppen a magas vérnyomás vérerekre gyakorolt hatásának elemzéséhez. Az értekezésben bemutatott érhálózat szegmentáló módszer ugyancsak egy pixelenkénti irányalapú megközelítést alkalmaz, azonban az érhálózat szegmentálásával szemben támasztott követelményeknek megfelelően eltér a bemutatott mikroaneurizma detektoroktól. A módszer részeként javasolt többléptékű mintaillesztési eljárás képes kiküszöbölni a vakfolt és világos léziók körvonalánál jelentkező magas maszk válaszokat, mely a hasonló eljárásoknál igen gyakori. Az irodalomban megtalálható hasonló, irányonkénti eljárásokat használó technikákkal szemben az itt bemutatott módszer nem csak a maximális választ tekinti, hanem egy olyan formulán alapul, mely lényegesen zajtűrőbb és magasabb értéket rendel az olyan elnyúlt struktúrákhoz mint az érhálózat darabjai, miközben a körszerű mikroaneurizmák értékét alacsonyan tartja. Az irány szerinti válaszok alkalmazásának javasolt módja az, ami alapvetően megkülönbözteti a bemutatott módszert az irodalmiaktól. Az irány szerinti válaszvektorokra javasolt korreláció alapú hasonlósági mérték, illetve osztályozó eljárás korábban még nem került alkalmazásra ezen a területen, és az ugyancsak itt bemutatott régiónövelő szegmentálási eljárással együttesen feltehetően más képfeldolgozási feladatokra is alkalmasak lehetnek.

Bemutatásra került továbbá, hogy a javasolt érhálózatot szegmentáló módszer egyes komponensei – konkrétan a mintaillesztési eljárás és érpont erősséget mérő formula – hogyan alkalmazhatóak dermatoszkópos képeken történő pigment-hálózat szegmentálási feladatokra. Itt egy egyszerű térbeli klaszterező eljárással vizsgáltuk a kinyert hálózatban lévő lyukak egymáshoz viszonyított helyzetét és számát, így becsülve a hálózat jelenlétét.

ACKNOWLEDGMENT

Some elements of this thesis were supported by the TECH08-2 project DRSCREEN – Developing a computer based image processing system for diabetic retinopathy screening of the National Office for Research and Technology of Hungary (contract no.: OM-00194/2008, OM-00195/2008, OM-00196/2008). We also acknowledge the Moorfields Eye Hospital, London for their clinical support. This work was supported in part by the TÁMOP-4.2.2.C-11/1/KONV-2012-0001 and the TÁMOP 4.2.2./B-10/1-2010-0024 projects. The work was supported in part by the European Union, co-financed by the European Social Fund. This work was also supported in part by the project OTKA/NK101680—Mathematical modeling of clinical observations for improved melanoma detection, and by the János Bolyai grant of the Hungarian Academy of Sciences.

I am grateful to my thesis advisor András Hajdu for his encouragement and guidance. I am also thankful to the Doctoral School of Informatics of the University of Debrecen for having provided the opportunity to conduct the research.

I am honoured to have worked with the members of the DRSCREEN project, especially the co-authors of my papers.

I am the most grateful to my family for supporting me throughout these years.

REFERENCES

[1] D. S. Fong, L. P. Aiello, F. L. Ferris, and R. Klein, “Diabetic Retinopathy,” *Diabetes Care*, vol. 27, no. 10, pp. 2540–2553, Oct. 2004.

[2] *Evidence-based eye care*. Philadelphia, PA: Lippincott Williams & Wilkins, 2007.

[3] B. Li and H. K. Li, “Automated Analysis of Diabetic Retinopathy Images: Principles, Recent Developments, and Emerging Trends,” *Curr. Diab. Rep.*, May 2013.

[4] M. M. Fraz, P. Remagnino, A. Hoppe, B. Uyyanonvara, A. R. Rudnicka, C. G. Owen, and S. A. Barman, “Blood vessel segmentation methodologies in retinal images – A survey,” *Comput. Methods Programs Biomed.*, vol. 108, no. 1, pp. 407–433, Oct. 2012.

[5] E. T. D. R. S. R. Group and others, “Early photocoagulation for diabetic retinopathy: ETDRS report number 9,” *Ophthalmology*, vol. 98, no. 5, pp. 766–785, 1991.

[6] L. Giancardo, F. Meriaudeau, T. P. Karnowski, Y. Li, S. Garg, K. W. Tobin, and E. Chaum, “Exudate-based diabetic macular edema detection in fundus images using publicly available datasets,” *Med. Image Anal.*, vol. 16, no. 1, pp. 216–226, Jan. 2012.

[7] S. Ali, D. Sidibé, K. M. Adal, L. Giancardo, E. Chaum, T. P. Karnowski, and F. Mériaudeau, “Statistical atlas based exudate segmentation,” *Comput. Med. Imaging Graph.*, Jul. 2013.

[8] I. Lazar and A. Hajdu, “Microaneurysm detection in retinal images using a rotating cross-section based model,” presented at the Biomedical Imaging: From Nano to Macro, 2011 IEEE International Symposium on, 2011, pp. 1405–1409.

[9] I. Lazar and A. Hajdu, “Retinal Microaneurysm Detection Through Local Rotating Cross-Section Profile Analysis,” *IEEE Trans. Med. Imaging*, vol. 32, no. 2, pp. 400–407, Feb. 2013.

[10] I. Lazar, R. J. Qureshi, and A. Hajdu, “A novel approach for the automatic detection of microaneurysms in retinal images,” 2010, pp. 193–197.

[11] I. Lázár and A. Hajdu, “Retinal Microaneurysm Detection Based on Intensity Profile Analysis,” in *Proceedings of the 8th International Conference on Applied Informatics*, Eger, Hungary, 2010, pp. 157–165.

[12] I. Lázár and A. Hajdu, “Keresztmetszeti intenzitás profilokon alapuló mikroaneurizma detektálás és érhálózat szegmentálás retina képeken,” in *Proceedings of a Képfeldolgozók és Alakfelismerők Társaságának 9. országos konferenciája*, 2013, pp. 404–412.

[13] I. Lazar and A. Hajdu, “Segmentation of vessels in retinal images based on directional height statistics,” presented at the Engineering in Medicine and Biology Society (EMBC), 2012 Annual International Conference of the IEEE, 2012, pp. 1458–1461.

[14] I. Lázár and A. Hajdu, “Segmentation of retinal vessels by means of directional response vector similarity and region growing,” *Comput. Biol. Med.*, vol. 66, pp. 209–221, Nov. 2015.

[15] C. Agurto, V. Murray, E. Barriga, S. Murillo, M. Pattichis, H. Davis, S. Russell, M. Abramoff, and P. Soliz, “Multiscale AM-FM Methods for Diabetic Retinopathy Lesion Detection,” *IEEE Trans. Med. Imaging*, vol. 29, no. 2, pp. 502–512, Feb. 2010.

[16] C. Köse, U. Şevik, C. İkibaş, and H. Erdöl, “Simple methods for segmentation and measurement of diabetic retinopathy lesions in retinal fundus images,” *Comput. Methods Programs Biomed.*, vol. 107, no. 2, pp. 274 – 293, 2012.

[17] G. Quellec, M. Lamard, M. D. Abràmoff, E. Decencière, B. Lay, A. Erginay, B.

Cochener, and G. Cazuguel, “A multiple-instance learning framework for diabetic retinopathy screening,” *Med. Image Anal.*, vol. 16, no. 6, pp. 1228–1240, Aug. 2012.

[18] M. R. K. Mookiah, U. R. Acharya, C. K. Chua, C. M. Lim, E. Y. K. Ng, and A. Laude, “Computer-aided diagnosis of diabetic retinopathy: A review,” *Comput. Biol. Med.*, vol. 43, no. 12, pp. 2136 – 2155, 2013.

[19] R. J. Winder, P. J. Morrow, I. N. McRitchie, J. R. Bailie, and P. M. Hart, “Algorithms for digital image processing in diabetic retinopathy,” *Comput. Med. Imaging Graph.*, vol. 33, no. 8, pp. 608–622, Dec. 2009.

[20] N. Patton, T. M. Aslam, T. MacGillivray, I. J. Deary, B. Dhillon, R. H. Eikelboom, K. Yogesan, and I. J. Constable, “Retinal image analysis: Concepts, applications and potential,” *Prog. Retin. Eye Res.*, vol. 25, no. 1, pp. 99–127, Jan. 2006.

[21] B. Laÿ, “Analyse automatique des images angiofluorographiques au cours de la rétinopathie diabétique,” *Ecole Natl. Supér. Mines Paris Cent. Morphol. Mathématique Paris Fr.*, 1983.

[22] C. Baudoin, B. Lay, and J. Klein, “Automatic detection of microaneurysms in diabetic fluorescein angiography.,” *Rev. Dépidémiologie Santé Publique*, vol. 32, no. 3–4, p. 254, 1984.

[23] F. Zana and J.-C. Klein, “Segmentation of vessel-like patterns using mathematical morphology and curvature evaluation,” *IEEE Trans. Image Process.*, vol. 10, no. 7, pp. 1010–1019, Jul. 2001.

[24] T. Spencer, J. A. Olson, K. C. McHardy, P. F. Sharp, and J. V. Forrester, “An Image-Processing Strategy for the Segmentation and Quantification of Microaneurysms in Fluorescein Angiograms of the Ocular Fundus,” *Comput. Biomed. Res.*, vol. 29, no. 4, pp. 284–302, Aug. 1996.

[25] M. J. Cree, J. A. Olson, K. C. McHardy, P. F. Sharp, and J. V. Forrester, “A fully automated comparative microaneurysm digital detection system,” *Eye*, vol. 11, no. 5, pp. 622–628, 1997.

[26] A. J. Frame, P. E. Undrill, M. J. Cree, J. A. Olson, K. C. McHardy, P. F. Sharp, and J. V. Forrester, “A comparison of computer based classification methods applied to the detection of microaneurysms in ophthalmic fluorescein angiograms,” *Comput. Biol. Med.*, vol. 28, no. 3, pp. 225–238, May 1998.

[27] A. M. Mendonca, A. J. Campilho, and J. M. Nunes, “Automatic Segmentation of Microaneurysms in Retinal Angiograms of Diabetic Patients,” *Image Anal. Process. Int. Conf. On*, vol. 0, p. 728, 1999.

[28] J. H. Hipwell, F. Strachan, J. A. Olson, K. C. McHardy, P. F. Sharp, and J. V. Forrester, “Automated detection of microaneurysms in digital red-free photographs: a diabetic retinopathy screening tool,” *Diabet. Med.*, vol. 17, no. 8, pp. 588–594, Aug. 2000.

[29] A. D. Fleming, S. Philip, K. A. Goatman, J. A. Olson, and P. F. Sharp, “Automated microaneurysm detection using local contrast normalization and local vessel detection,” *IEEE Trans. Med. Imaging*, vol. 25, no. 9, pp. 1223–1232, Sep. 2006.

[30] M. Niemeijer, B. van Ginneken, J. Staal, M. S. A. Suttorp-Schulten, and M. D. Abramoff, “Automatic detection of red lesions in digital color fundus photographs,” *IEEE Trans. Med. Imaging*, vol. 24, no. 5, pp. 584–592, May 2005.

[31] T. Walter, P. Massin, A. Erginay, R. Ordonez, C. Jeulin, and J.-C. Klein, “Automatic detection of microaneurysms in color fundus images,” *Med. Image Anal.*, vol. 11, no. 6, pp. 555–566, Dec. 2007.

[32] L. Vincent, “Morphological Area Openings and Closings for Grey-scale Images,” in

Shape in Picture, Y.-L. O, A. Toet, D. Foster, H. J. A. M. Heijmans, and P. Meer, Eds. Berlin, Heidelberg: Springer Berlin Heidelberg, 1994, pp. 197–208.

[33] K. Ram, G. D. Joshi, and J. Sivaswamy, "A Successive Clutter-Rejection-Based Approach for Early Detection of Diabetic Retinopathy," *IEEE Trans. Biomed. Eng.*, vol. 58, no. 3, pp. 664–673, Mar. 2011.

[34] A. Sopharak, B. Uyyanonvara, and S. Barman, "Simple hybrid method for fine microaneurysm detection from non-dilated diabetic retinopathy retinal images," *Comput. Med. Imaging Graph.*, Jun. 2013.

[35] B. Zhang, X. Wu, J. You, Q. Li, and F. Karray, "Detection of microaneurysms using multi-scale correlation coefficients," *Pattern Recognit.*, vol. 43, no. 6, pp. 2237–2248, Jun. 2010.

[36] A. Bhalerao, A. Patanaik, S. Anand, and P. Saravanan, "Robust Detection of Microaneurysms for Sight Threatening Retinopathy Screening," presented at the Computer Vision, Graphics & Image Processing, 2008. ICVGIP '08. Sixth Indian Conference on, 2008, pp. 520–527.

[37] A. Mizutani, C. Muramatsu, Y. Hatanaka, S. Suemori, T. Hara, and H. Fujita, "Automated microaneurysm detection method based on double ring filter in retinal fundus images," in *SPIE Medical Imaging*, 2009, p. 72601N–72601N.

[38] G. Quellec, M. Lamard, P. M. Josselin, G. Cazuguel, B. Cochener, and C. Roux, "Optimal Wavelet Transform for the Detection of Microaneurysms in Retina Photographs," *IEEE Trans. Med. Imaging*, vol. 27, no. 9, pp. 1230–1241, Sep. 2008.

[39] C. I. Sánchez, R. Hornero, A. Mayo, and M. García, "Mixture model-based clustering and logistic regression for automatic detection of microaneurysms in retinal images," 2009, p. 72601M–72601M–8.

[40] L. Giancardo, F. Mériaudeau, T. P. Karnowski, K. W. Tobin, Y. Li, and E. Chaum, "Microaneurysms detection with the radon cliff operator in retinal fundus images," presented at the Proc. SPIE 7623, Medical Imaging 2010: Image Processing, 2010, p. 76230U–76230U–8.

[41] L. Giancardo, F. Meriaudeau, T. P. Karnowski, Y. Li, K. W. Tobin, and E. Chaum, "Microaneurysm detection with radon transform-based classification on retina images," presented at the Engineering in Medicine and Biology Society,EMBC, 2011 Annual International Conference of the IEEE, 2011, pp. 5939–5942.

[42] M. Tavakoli, R. P. Shahri, H. Pourreza, A. Mehdizadeh, T. Banaee, and M. H. Bahreini Toosi, "A complementary method for automated detection of microaneurysms in fluorescein angiography fundus images to assess diabetic retinopathy," *Pattern Recognit.*, vol. 46, no. 10, pp. 2740–2753, Oct. 2013.

[43] J. Oliveira, G. Minas, and C. Silva, "Automatic detection of microaneurysm based on the slant stacking," presented at the Computer-Based Medical Systems (CBMS), 2013 IEEE 26th International Symposium on, 2013, pp. 308–313.

[44] T. Inoue, Y. Hatanaka, S. Okumura, C. Muramatsu, and H. Fujita, "Automated microaneurysm detection method based on eigenvalue analysis using hessian matrix in retinal fundus images," in *Engineering in Medicine and Biology Society (EMBC), 2013 35th Annual International Conference of the IEEE*, 2013, pp. 5873–5876.

[45] K. M. Adal, D. Sidibé, S. Ali, E. Chaum, T. P. Karnowski, and F. Mériaudeau, "Automated detection of microaneurysms using scale-adapted blob analysis and semi-supervised learning," *Comput. Methods Programs Biomed.*, Jan. 2014.

[46] M. U. Akram, S. Khalid, and S. A. Khan, "Identification and classification of

microaneurysms for early detection of diabetic retinopathy," *Pattern Recognit.*, vol. 46, no. 1, pp. 107–116, Jan. 2013.

[47] B. Antal and A. Hajdu, "Improving microaneurysm detection using an optimally selected subset of candidate extractors and preprocessing methods," *Pattern Recognit.*, vol. 45, no. 1, pp. 264–270, Jan. 2012.

[48] B. Antal and A. Hajdu, "An Ensemble-Based System for Microaneurysm Detection and Diabetic Retinopathy Grading," *IEEE Trans. Biomed. Eng.*, vol. 59, no. 6, pp. 1720–1726, Jun. 2012.

[49] C. Heneghan, "Characterization of changes in blood vessel width and tortuosity in retinopathy of prematurity using image analysis," *Med. Image Anal.*, vol. 6, no. 4, pp. 407–429, Dec. 2002.

[50] E. Grisan, M. Foracchia, and A. Ruggeri, "A Novel Method for the Automatic Grading of Retinal Vessel Tortuosity," *IEEE Trans. Med. Imaging*, vol. 27, no. 3, pp. 310–319, Mar. 2008.

[51] M. Foracchia, E. Grisan, and A. Ruggeri, "Detection of Optic Disc in Retinal Images by Means of a Geometrical Model of Vessel Structure," *IEEE Trans. Med. Imaging*, vol. 23, no. 10, pp. 1189–1195, Oct. 2004.

[52] A. A.-H. A.-R. Youssif, A. Z. Ghalwash, and A. A. S. A.-R. Ghoneim, "Optic Disc Detection From Normalized Digital Fundus Images by Means of a Vessels' Direction Matched Filter," *IEEE Trans. Med. Imaging*, vol. 27, no. 1, pp. 11–18, 2008.

[53] M. Niemeijer, M. D. Abràmoff, and B. van Ginneken, "Fast detection of the optic disc and fovea in color fundus photographs," *Med. Image Anal.*, vol. 13, no. 6, pp. 859 – 870, 2009.

[54] A. M. Mendonça, A. Sousa, L. Mendonça, and A. Campilho, "Automatic localization of the optic disc by combining vascular and intensity information," *Comput. Med. Imaging Graph.*, vol. 37, no. 5–6, pp. 409–417, Jul. 2013.

[55] A. Hoover and M. Goldbaum, "Locating the optic nerve in a retinal image using the fuzzy convergence of the blood vessels," *IEEE Trans. Med. Imaging*, vol. 22, no. 8, pp. 951–958, Aug. 2003.

[56] L. Tang, M. Niemeijer, J. M. Reinhardt, M. K. Garvin, and M. D. Abramoff, "Splat Feature Classification With Application to Retinal Hemorrhage Detection in Fundus Images," *IEEE Trans. Med. Imaging*, vol. 32, no. 2, pp. 364–375, Feb. 2013.

[57] D. Youssef and N. H. Solouma, "Accurate detection of blood vessels improves the detection of exudates in color fundus images," *Comput. Methods Programs Biomed.*, vol. 108, no. 3, pp. 1052 – 1061, 2012.

[58] F. Zana and J. C. Klein, "A multimodal registration algorithm of eye fundus images using vessels detection and Hough transform," *IEEE Trans. Med. Imaging*, vol. 18, no. 5, pp. 419–428, May 1999.

[59] G. K. Matsopoulos, P. A. Asvestas, N. A. Mouravliansky, and K. K. Delibasis, "Multimodal Registration of Retinal Images Using Self Organizing Maps," *IEEE Trans. Med. Imaging*, vol. 23, no. 12, pp. 1557–1563, Dec. 2004.

[60] C. Mariño, M. G. Penedo, M. Penas, M. J. Carreira, and F. Gonzalez, "Personal authentication using digital retinal images," *Pattern Anal. Appl.*, vol. 9, no. 1, pp. 21–33, May 2006.

[61] C. Köse and C. İki˙baş, "A personal identification system using retinal vasculature in retinal fundus images," *Expert Syst. Appl.*, May 2011.

[62] S. M. Lajevardi, A. Arakala, S. A. Davis, and K. J. Horadam, "Retina Verification

System Based on Biometric Graph Matching," *IEEE Trans. Image Process.*, vol. 22, no. 9, pp. 3625–3635, Sep. 2013.

[63] M. M. Fraz, P. Remagnino, A. Hoppe, B. Uyyanonvara, A. R. Rudnicka, C. G. Owen, and S. A. Barman, "An Ensemble Classification-Based Approach Applied to Retinal Blood Vessel Segmentation," *IEEE Trans. Biomed. Eng.*, vol. 59, no. 9, pp. 2538–2548, Sep. 2012.

[64] Xiayu Xu, M. Niemeijer, Qi Song, M. Sonka, M. K. Garvin, J. M. Reinhardt, and M. D. Abramoff, "Vessel Boundary Delineation on Fundus Images Using Graph-Based Approach," *IEEE Trans. Med. Imaging*, vol. 30, no. 6, pp. 1184–1191, Jun. 2011.

[65] D. Marín, A. Aquino, M. E. Gegundez-Arias, and J. M. Bravo, "A New Supervised Method for Blood Vessel Segmentation in Retinal Images by Using Gray-Level and Moment Invariants-Based Features," *IEEE Trans. Med. Imaging*, vol. 30, no. 1, pp. 146–158, Jan. 2011.

[66] C. A. Lupascu, D. Tegolo, and E. Trucco, "FABC: Retinal Vessel Segmentation Using AdaBoost," *IEEE Trans. Inf. Technol. Biomed.*, vol. 14, no. 5, pp. 1267–1274, Sep. 2010.

[67] B. S. Y. Lam, Yongsheng Gao, and A. W.-C. Liew, "General Retinal Vessel Segmentation Using Regularization-Based Multiconcavity Modeling," *IEEE Trans. Med. Imaging*, vol. 29, no. 7, pp. 1369–1381, Jul. 2010.

[68] S. Chaudhuri, S. Chatterjee, N. Katz, M. Nelson, and M. Goldbaum, "Detection of blood vessels in retinal images using two-dimensional matched filters," *IEEE Trans. Med. Imaging*, vol. 8, no. 3, pp. 263–269, Sep. 1989.

[69] A. D. Hoover, V. Kouznetsova, and M. Goldbaum, "Locating blood vessels in retinal images by piecewise threshold probing of a matched filter response," *IEEE Trans. Med. Imaging*, vol. 19, no. 3, pp. 203–210, Mar. 2000.

[70] M. Al-Rawi, M. Qutaishat, and M. Arrar, "An improved matched filter for blood vessel detection of digital retinal images," *Comput. Biol. Med.*, vol. 37, no. 2, pp. 262–267, Feb. 2007.

[71] M. Al-Rawi and H. Karajeh, "Genetic algorithm matched filter optimization for automated detection of blood vessels from digital retinal images," *Comput. Methods Programs Biomed.*, vol. 87, no. 3, pp. 248–253, Sep. 2007.

[72] A. M. Mendonca and A. Campilho, "Segmentation of retinal blood vessels by combining the detection of centerlines and morphological reconstruction," *IEEE Trans. Med. Imaging*, vol. 25, no. 9, pp. 1200–1213, Sep. 2006.

[73] Lei Zhang, Qin Li, J. You, and D. Zhang, "A Modified Matched Filter With Double-Sided Thresholding for Screening Proliferative Diabetic Retinopathy," *IEEE Trans. Inf. Technol. Biomed.*, vol. 13, no. 4, pp. 528–534, Jul. 2009.

[74] B. Zhang, L. Zhang, L. Zhang, and F. Karray, "Retinal vessel extraction by matched filter with first-order derivative of Gaussian," *Comput. Biol. Med.*, vol. 40, no. 4, pp. 438–445, Apr. 2010.

[75] M. Sofka and C. V. Stewart, "Retinal Vessel Centerline Extraction Using Multiscale Matched Filters, Confidence and Edge Measures," *IEEE Trans. Med. Imaging*, vol. 25, no. 12, pp. 1531–1546, Dec. 2006.

[76] M. M. Fraz, S. A. Barman, P. Remagnino, A. Hoppe, A. Basit, B. Uyyanonvara, A. R. Rudnicka, and C. G. Owen, "An approach to localize the retinal blood vessels using bit planes and centerline detection," *Comput. Methods Programs Biomed.*, vol. 108, no. 2, pp. 600–616, Nov. 2012.

[77] J. Jan, J. Odstrcilik, J. Gazarek, and R. Kolar, “Retinal image analysis aimed at blood vessel tree segmentation and early detection of neural-layer deterioration,” *Comput. Med. Imaging Graph.*, vol. 36, no. 6, pp. 431–441, Sep. 2012.

[78] J. Lowell, A. Hunter, D. Steel, A. Basu, R. Ryder, and R. L. Kennedy, “Measurement of Retinal Vessel Widths From Fundus Images Based on 2-D Modeling,” *IEEE Trans. Med. Imaging*, vol. 23, no. 10, pp. 1196–1204, Oct. 2004.

[79] B. Al-Diri, A. Hunter, and D. Steel, “An Active Contour Model for Segmenting and Measuring Retinal Vessels,” *IEEE Trans. Med. Imaging*, vol. 28, no. 9, pp. 1488–1497, Sep. 2009.

[80] E. Ricci and R. Perfetti, “Retinal Blood Vessel Segmentation Using Line Operators and Support Vector Classification,” *IEEE Trans. Med. Imaging*, vol. 26, no. 10, pp. 1357–1365, Oct. 2007.

[81] X. You, Q. Peng, Y. Yuan, Y. Cheung, and J. Lei, “Segmentation of retinal blood vessels using the radial projection and semi-supervised approach,” *Pattern Recognit.*, vol. 44, no. 10–11, pp. 2314–2324, Oct. 2011.

[82] Yuan Yuan, Yishan Luo, and A. C. S. Chung, “VE-LLI-VO: Vessel Enhancement Using Local Line Integrals and Variational Optimization,” *IEEE Trans. Image Process.*, vol. 20, no. 7, pp. 1912–1924, Jul. 2011.

[83] U. T. V. Nguyen, A. Bhuiyan, L. A. F. Park, and K. Ramamohanarao, “An effective retinal blood vessel segmentation method using multi-scale line detection,” *Pattern Recognit.*, vol. 46, no. 3, pp. 703–715, Mar. 2013.

[84] Y. Wang, G. Ji, P. Lin, and E. Trucco, “Retinal vessel segmentation using multiwavelet kernels and multiscale hierarchical decomposition,” *Pattern Recognit.*, vol. 46, no. 8, pp. 2117–2133, Aug. 2013.

[85] Y. Qian Zhao, X. Hong Wang, X. Fang Wang, and F. Y. Shih, “Retinal vessels segmentation based on level set and region growing,” *Pattern Recognit.*, vol. 47, no. 7, pp. 2437–2446, Jul. 2014.

[86] Y. Yin, M. Adel, M. Guillaume, S. Bourennane, and others, “Bayesian tracking for blood vessel detection in retinal images,” presented at the 18th European Signal Processing Conference (EUSIPCO-2010), Aalborg, Denmark, 2010, pp. 1009–1013.

[87] Y. Yin, M. Adel, and S. Bourennane, “Retinal vessel segmentation using a probabilistic tracking method,” *Pattern Recognit.*, vol. 45, no. 4, pp. 1235–1244, Apr. 2012.

[88] J. Odstrcilik, R. Kolar, A. Budai, J. Hornegger, J. Jan, J. Gazarek, T. Kubena, P. Cernosek, O. Svoboda, and E. Angelopoulou, “Retinal vessel segmentation by improved matched filtering: evaluation on a new high-resolution fundus image database,” *IET Image Process.*, vol. 7, no. 4, pp. 373–383, Jun. 2013.

[89] M. E. Martinez-Perez, A. D. Hughes, S. A. Thom, A. A. Bharath, and K. H. Parker, “Segmentation of blood vessels from red-free and fluorescein retinal images,” *Med. Image Anal.*, vol. 11, no. 1, pp. 47–61, Feb. 2007.

[90] M. A. Palomera-Perez, M. E. Martinez-Perez, H. Benitez-Perez, and J. L. Ortega-Arjona, “Parallel Multiscale Feature Extraction and Region Growing: Application in Retinal Blood Vessel Detection,” *IEEE Trans. Inf. Technol. Biomed.*, vol. 14, no. 2, pp. 500–506, Mar. 2010.

[91] A. Anzalone, F. Bizzarri, M. Parodi, and M. Storace, “A modular supervised algorithm for vessel segmentation in red-free retinal images,” *Comput. Biol. Med.*, vol. 38, no. 8, pp. 913–922, Aug. 2008.

[92] R. Annunziata, A. Garzelli, L. Ballerini, A. Mecocci, and E. Trucco, “Leveraging

Multiscale Hessian-based Enhancement with a Novel Exudate Inpainting Technique for Retinal Vessel Segmentation," *IEEE J. Biomed. Health Inform.*, pp. 1–1, 2015.

[93] X.-X. Yin, B. W.-H. Ng, J. He, Y. Zhang, and D. Abbott, "Unsupervised Segmentation of Blood Vessels from Colour Retinal Fundus Images," in *Health Information Science*, vol. 8423, Y. Zhang, G. Yao, J. He, L. Wang, N. R. Smalheiser, and X. Yin, Eds. Cham: Springer International Publishing, 2014, pp. 194–203.

[94] H. Yu, S. Barriga, C. Agurto, G. Zamora, W. Bauman, and P. Soliz, "Fast vessel segmentation in retinal images using multiscale enhancement and second-order local entropy," 2012, p. 83151B.

[95] J. Staal, M. D. Abramoff, M. Niemeijer, M. A. Viergever, and B. van Ginneken, "Ridge-Based Vessel Segmentation in Color Images of the Retina," *IEEE Trans. Med. Imaging*, vol. 23, no. 4, pp. 501–509, Apr. 2004.

[96] M. Vlachos and E. Dermatas, "Multi-scale retinal vessel segmentation using line tracking," *Comput. Med. Imaging Graph.*, vol. 34, no. 3, pp. 213–227, Apr. 2010.

[97] M. S. Miri and A. Mahloojifar, "Retinal Image Analysis Using Curvelet Transform and Multistructure Elements Morphology by Reconstruction," *IEEE Trans. Biomed. Eng.*, vol. 58, no. 5, pp. 1183–1192, May 2011.

[98] B. S. Y. Lam and Hong Yan, "A Novel Vessel Segmentation Algorithm for Pathological Retina Images Based on the Divergence of Vector Fields," *IEEE Trans. Med. Imaging*, vol. 27, no. 2, pp. 237–246, Feb. 2008.

[99] A. Fathi and A. R. Naghsh-Nilchi, "Automatic wavelet-based retinal blood vessels segmentation and vessel diameter estimation," *Biomed. Signal Process. Control*, vol. 8, no. 1, pp. 71–80, Jan. 2013.

[100] M. Usman Akram, S. Khalid, A. Tariq, and M. Younus Javed, "Detection of neovascularization in retinal images using multivariate m-Mediods based classifier," *Comput. Med. Imaging Graph.*, vol. 37, no. 5–6, pp. 346–357, Jul. 2013.

[101] P. Bankhead, C. N. Scholfield, J. G. McGeown, and T. M. Curtis, "Fast Retinal Vessel Detection and Measurement Using Wavelets and Edge Location Refinement," *PLoS ONE*, vol. 7, no. 3, p. e32435, 2012.

[102] J.-L. Starck, J. Fadili, and F. Murtagh, "The Undecimated Wavelet Decomposition and its Reconstruction," *IEEE Trans. Image Process.*, vol. 16, no. 2, pp. 297–309, Feb. 2007.

[103] J. V. B. Soares, J. J. G. Leandro, R. M. Cesar, H. F. Jelinek, and M. J. Cree, "Retinal vessel segmentation using the 2-D Gabor wavelet and supervised classification," *IEEE Trans. Med. Imaging*, vol. 25, no. 9, pp. 1214–1222, Sep. 2006.

[104] P. C. Bunch, J. F. Hamilton, G. K. Sanderson, and A. H. Simmons, "A Free Response Approach To The Measurement And Characterization Of Radiographic Observer Performance," in *Proc. SPIE 0127, Application of Optical Instrumentation in Medicine VI*, 1977, pp. 124–135.

[105] M. Niemeijer, B. van Ginneken, M. J. Cree, A. Mizutani, G. Quellec, C. I. Sanchez, B. Zhang, R. Hornero, M. Lamard, C. Muramatsu, X. Wu, G. Cazuguel, J. You, A. Mayo, Qin Li, Y. Hatanaka, B. Cochener, C. Roux, F. Karray, M. Garcia, H. Fujita, and M. D. Abramoff, "Retinopathy Online Challenge: Automatic Detection of Microaneurysms in Digital Color Fundus Photographs," *IEEE Trans. Med. Imaging*, vol. 29, no. 1, pp. 185–195, Jan. 2010.

[106] L. Gagnon, M. Lalonde, M. Beaulieu, and M.-C. Boucher, "Procedure to detect anatomical structures in optical fundus images," presented at the Proc. SPIE 4322,

Medical Imaging 2001: Image Processing, 2001, pp. 1218–1225.
[107] E. J. Breen and R. Jones, “Attribute Openings, Thinnings, and Granulometries,” *Comput. Vis. Image Underst.*, vol. 64, no. 3, pp. 377–389, Nov. 1996.
[108] L. Vincent, “Morphological grayscale reconstruction in image analysis: applications and efficient algorithms,” *IEEE Trans. Image Process.*, vol. 2, no. 2, pp. 176–201, Apr. 1993.
[109] K. H. Jarman, D. S. Daly, K. K. Anderson, and K. L. Wahl, “A new approach to automated peak detection,” *Chemom. Intell. Lab. Syst.*, vol. 69, no. 1–2, pp. 61–76, Nov. 2003.
[110] K. R. Coombes, S. Tsavachidis, J. S. Morris, K. A. Baggerly, M.-C. Hung, and H. M. Kuerer, “Improved peak detection and quantification of mass spectrometry data acquired from surface-enhanced laser desorption and ionization by denoising spectra with the undecimated discrete wavelet transform,” *PROTEOMICS*, vol. 5, no. 16, pp. 4107–4117, Nov. 2005.
[111] G. Vivó-Truyols, J. R. Torres-Lapasió, A. M. van Nederkassel, Y. Vander Heyden, and D. L. Massart, “Automatic program for peak detection and deconvolution of multi-overlapped chromatographic signals,” *J. Chromatogr. A*, vol. 1096, no. 1–2, pp. 146–155, Nov. 2005.
[112] S. Peters, G. Vivó-Truyols, P. J. Marriott, and P. J. Schoenmakers, “Development of an algorithm for peak detection in comprehensive two-dimensional chromatography,” *J. Chromatogr. A*, vol. 1156, no. 1–2, pp. 14–24, Jul. 2007.
[113] C.-C. Chang and C.-J. Lin, “LIBSVM: A library for support vector machines,” *ACM Trans. Intell. Syst. Technol.*, vol. 2, no. 3, pp. 27:1–27:27, 2011.
[114] C. A. Schneider, W. S. Rasband, and K. W. Eliceiri, “NIH Image to ImageJ: 25 years of image analysis,” *Nat. Methods*, vol. 9, no. 7, pp. 671–675, Jun. 2012.
[115] A. A. Marghoob, R. P. Braun, and A. W. Kopf, *Atlas of dermoscopy*. London; New York: Taylor & Francis, 2005.
[116] G. Argenziano, H. P. Soyer, V. D. Giorgi, D. Piccolo, P. Carli, M. Delfino, A. Ferrari, R. Hofmann-Wellenhof, D. Massi, G. Mazzocchetti, M. Scalvenzi, and I. H. Wolf, *Interactive atlas of dermoscopy*. Edra Medical Pub. & New Media, 2000.
[117] M. Sadeghi, M. Razmara, T. K. Lee, and M. S. Atkins, “A novel method for detection of pigment network in dermoscopic images using graphs,” *Comput. Med. Imaging Graph.*, vol. 35, no. 2, pp. 137–143, Mar. 2011.
[118] C. Barata, J. S. Marques, and J. Rozeira, “A System for the Detection of Pigment Network in Dermoscopy Images Using Directional Filters,” *IEEE Trans. Biomed. Eng.*, vol. 59, no. 10, pp. 2744–2754, Oct. 2012.
[119] J. L. García Arroyo and B. García Zapirain, “Detection of pigment network in dermoscopy images using supervised machine learning and structural analysis,” *Comput. Biol. Med.*, Nov. 2013.
[120] J. Toth, L. Bartha, T. Szabo, I. Lazar, B. Harangi, and A. Hajdu, “An online application for storing, analyzing, and sharing dermatological data,” presented at the 6th IEEE International Conference on Cognitive Infocommunications (CogInfoCom 2015), Gyor, Hungary, 2015, pp. 339–342.

LIST OF THE AUTHOR'S PUBLICATIONS

Publications related to the thesis

Journal articles

I. Lázár and A. Hajdu, “Segmentation of retinal vessels by means of directional response vector similarity and region growing,” *Computers in Biology and Medicine*, vol. 66, pp. 209–221, Nov. 2015, DOI: 10.1016/j.compbiomed.2015.09.008.

I. Lázár and A. Hajdu, “Retinal Microaneurysm Detection Through Local Rotating Cross-Section Profile Analysis,” *IEEE Transactions on Medical Imaging*, vol. 32, no. 2, pp. 400–407, Feb. 2013, DOI: 10.1109/TMI.2012.2228665.

Articles in the proceedings of international conferences

I. Lázár and A. Hajdu, “Segmentation of vessels in retinal images based on directional height statistics,” in *Proceedings of the Engineering in Medicine and Biology Society (EMBC), 2012 Annual International Conference of the IEEE*, pp. 1458–1461, 2012, DOI: 10.1109/EMBC.2012.6346215.

I. Lázár and A. Hajdu, “Microaneurysm detection in retinal images using a rotating cross-section based model,” in *Proceedings of the Biomedical Imaging: From Nano to Macro, 2011 IEEE International Symposium on*, pp. 1405–1409, 2011, DOI: 10.1109/ISBI.2011.5872663.

I. Lázár, R. J. Qureshi, and A. Hajdu, “A novel approach for the automatic detection of microaneurysms in retinal images,” in *Proceedings of the Emerging Technologies (ICET), 2010 6th International Conference on*, pp. 193–197, 2010, DOI: 10.1109/ICET.2010.5638490.

I. Lázár and A. Hajdu, “Retinal Microaneurysm Detection Based on Intensity Profile Analysis,” in *Proceedings of the 8th International Conference on Applied Informatics (ICAI 2010)*, pp. 157–165, 2010.

Articles in the proceedings of Hungarian conferences

I. Lázár and A. Hajdu, “Keresztmetszeti intenzitás profilokon alapuló mikroaneurizma detektálás és érhálózat szegmentálás retina képeken,” in *Proceedings of Képfeldolgozók és Alakfelismerők Társaságának 9. országos konferenciája*, pp. 404-412, 2013.

Other publications

Articles in the proceedings of international conferences

J. Toth, L. Bartha, T. Szabo, **I. Lazar**, B. Harangi, A. Hajdu, “An Online Application for Storing, Analyzing, and Sharing Dermatological Data,” *Cognitive Infocommunications (CogInfoCom), 2015 6th IEEE International Conference on*, Gyor. Hungary, pp. 339-342, 2015, DOI: 10.1109/CogInfoCom.2015.7390615.

B. Antal, **I. Lázár**, and A. Hajdu, “An adaptive weighting approach for ensemble-based detection of microaneurysms in color fundus images,” in *Proceedings of the Engineering in*

Medicine and Biology Society (EMBC), 2012 Annual International Conference of the IEEE, pp. 5955–5958, 2012, DOI: 10.1109/EMBC.2012.6347350.

B. Antal, **I. Lázár**, and A. Hajdu "An Ensemble Approach to Improve Microaneurysm Candidate Extraction," in *Communications in Computer and Information Science - 7th International Joint Conference, ICETE 2010, Revised Selected Papers*, pp. 378-391, 2012. DOI: 10.1007/978-3-642-25206-8_25.

B. Antal, **I. Lázár**, A. Hajdu, Zs. Török, A. Csutak, and T. Pető, "Evaluation of the grading performance of an ensemble-based microaneurysm detector," in *Proceedings of the Engineering in Medicine and Biology Society (EMBC), 2011 Annual International Conference of the IEEE*, pp. 5943–5946, 2011, DOI: 10.1109/IEMBS.2011.6091469.

B. Antal, **I. Lázár**, A. Hajdu, Zs. Török, A. Csutak, and T. Pető, "A multi-level ensemble-based system for detecting microaneurysms in fundus images," in *Proceedings of the 4th IEEE International Workshop on Soft Computing Applications*, pp. 137-142, 2010, DOI: 10.1109/SOFA.2010.5565609.

B. Antal, **I. Lázár**, and A. Hajdu, "An optimal voting scheme for microaneurysm candidate extractors using simulated annealing," in *Proceedings of the 5th International Conference on Signal Processing and Multimedia Applications (SIGMAP 2010)*, pp. 80-87, 2010.

B. Antal, **I. Lázár**, and A. Hajdu, "Novel approaches to improve microaneurysm detection in retinal images" in *Proceedings of the 8th International Conference on Applied Informatics (ICAI 2010)*, pp. 149-156, 2010.

Articles in the proceedings of Hungarian conferences

B. Antal, **I. Lázár**, and A. Hajdu, "Mikroaneurizma detektálás összetett rendszerrel," in *Proceedings of Képfeldolgozók és Alakfelismerők Társaságának 8. országos konferenciája*, pp 155-162, 2011.

Conference abstracts

A. Csutak, B. Antal, I. **Lázár,** T. Pető, Z. Török, A. Biró, A. Hajdu, "Diabetic retinopathy screening with computational support" in *Acta Ophthalmol.* 89, p. 357, 2011, DOI: 10.1111/j.1755-3768.2011.357.x

Technical reports

I. Lázár, B. Antal, and A. Hajdu, "Microaneurysm detection in digital fundus images," Tech. Rep. 2010/14(387), University of Debrecen, Hungary.